# ABSTRACT

**MOSES, SELINA. Characterization and functionalization of substrates and nanoparticles for detection of surface binding events of biomolecules. (Under the direction of Stefan Franzen.)**

This dissertation mainly focuses on detection of biomolecules on metal and metal-oxide surfaces by photoelectrochemistry. Characterization of DNA monolayers on the surface of gold was studied in detail by X-ray photoelectron spectroscopy (XPS), Polarization Modulated Infrared reflectance absorbance Spectroscopy (PMIRRAS) and FTIR. An electrochemical technique Chronocoulometry (CC) quantified the surface coverage of ssDNA on gold to be ~ $10^{12}$ molecules/cm$^2$. The issues that affected the hybridization efficiency of DNA on the gold surface were analyzed and parameters for optimum hybridization were established by the same techniques used to detect ssDNA on the surface. Though gold is a well-known surface, the thiol chemistry, which is the basis of attaching DNA on the surface, is not robust and reproducible due to the desorption of probes from the surface during hybridization, which involves elevating the temperature. Hybridization yield on gold surfaces could not be determined accurately as the desorption of probe from the surface was a competing phenomenon during hybridization event. As a result, new substrates were analyzed and indium-doped tin oxide (ITO) was found to be a very useful substrate because of the ease with which it can be modified with COOH, Phosphates, Phosphonates and silanes. In addition, the physical properties of ITO make it an attractive candidate to use in creating bioarrays. It is highly conductive and tansparent in the visible region and reflective in the IR. Compared to the thiol chemistry on gold the phosphates are much stronger and resistant to elevated temperatures used for hybridization. ITO electrodes can sustain relatively high potentials required to oxidize

gold nanoparticles used as labels to detect hybridization. All these properties can be utilized to characterize ssDNA modified ITO surfaces and surface DNA hybridization either by optical or electrical methods. 12-Phosphonododecanoic acid (12-PDA) formed a well-ordered monolayer on the ITO surface. By activating the COOH group by 1-ethyl-3-(3-dimethylaminopropyl)carbodiimide hydrochloride (EDC), an amine terminated DNA probe can be attached to the surface with 12-PDA as the linker. Studies on monolayer of DNA on ITO by XPS, IR show presence of DNA on the ITO surface and CC reveals a surface coverage of ~ $10^{13}$ molecules/$cm^2$. The detection strategies employed in this study to detect hybridization of DNA was by probing the gold nanoparticle labeled target DNA by XPS, AFM, electrochemical stripping and thermography. To further improve the design, $TiO_2$ nanoparticles sensitized with a Ruthenium polypyridyl complex was used as a label to detect DNA hybridization photoelectrochemically. This idea was generalized further to detect viruses - Red Clover Necrotic Mosaic Virus (RCNMV) and HIV from Gag protein immobilized on the ITO surface.

# CHARACTERIZATION AND FUNCTIONALIZATION OF SUBSTRATES AND NANOPARTICLES FOR DETECTION OF SURFACE BINDING EVENTS OF BIOMOLECULES

by

SELINA MOSES

A dissertation submitted to the Graduate Faculty of
North Carolina State University
in partial fulfillment of the requirements
for the Degree of
Doctor of Philosophy

**CHEMISTRY**

Raleigh, North Carolina

2005

**APPROVED BY:**

Dr. Stefan Franzen, Chair of Advisory Committee

Dr. Daniel Feldheim

Dr. Paul Maggard

Dr. Jan Genzer

## DEDICATION

To my wonderful parents

who taught me to dream big in life and

supported me with their

thoughtful prayers

To my dear sister and her family

for their encouragement

and love

To my loving husband

for constantly inspiring me

and for believing in me

## BIOGRAPHY

Selina Moses was born on October 12, 1976 in Tirunelveli, a city in the most southern part of India. As her father was serving in the “Indian Air Force” she was raised in various parts of India and attended elementary school affiliated to the “Central Board of Secondary Education” in various states of India. She has won prestigious awards for Drawing and has represented her school in many activities. She passed her “Higher Secondary School” with distinction and joined “Nowrosjee Wadia College” in Pune, Maharashtra to get her Batchelors Degree in Chemistry. She was accepted by “University of Pune”, affiliated with the “National Chemical Laboratory” – one of the best schools for Physical Chemistry, to pursue her graduate studies in Physical Chemistry. Selina graduated with a Masters Degree in Physical Chemistry in 1999 as one of the top rank holders in the University. She joined the “Department of Chemistry” at “University of Illinois at Chicago” for Graduate Program in 2000. She was engaged to Jabastine in 2001 and planned to transfer to a good school in NC to be with her fiance. Around that time, Dr. Stefan Franzen was invited for a seminar to UIC and excited with his research interests, she transferred to North Carolina State University to complete her Graduate Studies under the guidance of Dr. Stefan Franzen. She worked on many different projects and got various opportunities to present her research in National Meetings.also received the “Outstanding Researcher Award” for 2002 Departmental Poster Session. Her main focus of research was developing sensitive detection methods to detect DNA hybridization on metal and metal-oxide substrates.

**ACKNOWLEDGEMENTS**

First and foremost I would like to give all glory and honor to God, the source of all wisdom and understanding. He granted me His grace, strength and guidance at every step throughout the strenuous years of graduate student life. God has led me in wonderful ways and brought wonderful people along my way for whom I am thankful.

My husband Jabastine Moses, has been my constant source of inspiration. When I see him tirelessly persuing his MBA at Duke University and keeping a full time job it inspires me. He has motivated me immensely and listened to all my frustrations when my experiments failed and shared the happy moments of exciting results. He would push me as hard as he could to get more publications!! His love, friendship and support have carried me through these years.

My parents Chandra Anthireya and Jesudason Anthireya encouraged me from early on in life to work hard and do my best in everything. They supported my interest in science through school and college and made it possible for me to dream big and set high goals in life. Growing up they provided a loving atmosphere and instilled good discipline, which was much needed in my Graduate student life. My sister Sophia, was always ready to help me with my doubts in science especially in chemistry and taught me how to balance chemical equations! Without my family's support and prayers I would not be who I am today.

I would also like to acknowledge my friends Ruchira, Vishal and Sharan for the fun and laughter we shared and the motivation we got from each other to go for a Ph.D in Chemistry. My friends here at International Community Church have always wished me well, prayed with me for every obstacle, and rejoiced in every victory. I want to thank

each and every one of them, specially the Dinakaran's for their constant care, love and fellowship.

My life as a graduate student would not have been so rewarding if it not were for my research advisor Dr. Stefan Franzen. He has a way of inspring people with his passion for science. He is extremely resourceful and knowledgeable and yet would take time to discuss and explain concepts as many times as I requested. His enthusiasm would make me strive harder everytime I had a meeting with him. I also want to thank Jan Genzer, Daniel Feldheim and Paul Maggard for being on my committee and reviewing my diisertation. Dan and Paul have also contributed a lot to this thesis and I have benefited greatly by the fruitful discussions I had with both of them.

I would like to thank all those who have inspired me and supported me throughout my stay in NCSU. All the present and past members of Franzen research group have been very friendly and supportive. Also all the other wonderful people I met in NCSU, I want to thank you for your friendship and support.

TABLE OF CONTENTS

**CHAPTER 7**

## LIST OF TABLES

## LIST OF FIGURES

## LIST OF SCHEMES

# CHAPTER 1

# Introduction and Background

## *1.1 Introduction*

All living things have a characteristic set of chromosomes present in the nucleus of each cell. Biochemical studies carried out around 1940 indicated that the nuclear materials that make up the chromosomes are composed of DNA and proteins. Three billion chemical bases make up human DNA forming estimated 50,000 – 100,000 genes into what is called human genome. The human genome is contained within the 23 pairs of chromosomes in the nucleus of a human cell, plus one tiny type of chromosome contained in a cell's mitochondria. The genomic sequence provides access to the complete structures of all genes, including those without known function, their control elements, and, by inference, the proteins they encode, as well as all other biologically important sequences. The object of Human Genome Project was to decipher the entire nucleotide sequence of each of these DNA molecules – the location and identity of all the genes to determine which gene sequence is responsible for the genetic disorders. Also genetic mutations leading to diseases and cancer have been an area of intense investigation. Interesting research has been carried out to develop new techniques that would provide insight to the sequence-specific information of DNA. Constant efforts are put in to obtain this information in a cheaper, faster and economical manner.

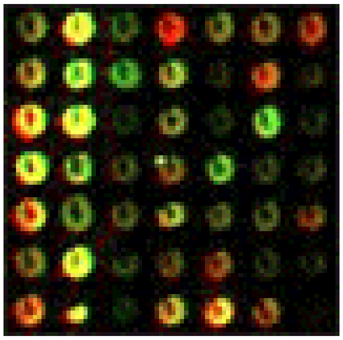

**Figure 1.1 Fluorescence based microarray**
http://www.gene-chips.com

DNA microarray, or DNA (gene) chips are an array of probes (DNA with known sequence) immobilized on a solid substrate. The DNA chip is then exposed to a solution of target (analyte) that may be complementary to one set of probes on the surface. The hybridization may be then detected directly or by a marker tagged to the target. An experiment with a single DNA chip can provide researchers information on thousands of genes simultaneously - a dramatic increase in throughput.

. In the present study, the focus is on creating a light-addressable biosensor array for detecting DNA, viruses and proteins on surface. To create a microarray compatable with the current technology many parameters have to be investigated in detail. Studies have been carried out on routine assays to understand the substrates, their surface-binding chemistry and factors affecting DNA hybridization on surface. A systematic study to obtain a robust and stable DNA monolayer and to characterize and optimize DNA hybridization on surfaces for better surface coverage and high hybridization yield will be conducted. It is important to achieve high selectivity, sensitivity and lower detection limit in comparison to the techniques used routinely for detection of DNA hybridization on the surface. Hence novel labels and attachment chemistry have been explored to develop an array system such that photoelectrochemical detection of hybridized target DNA or immobilized virus using dye-sensitized metal-oxide nanoparticles as labels.

## *1.2 Background*

### 1.2.1 DNA Morphology

Deoxyribonucleic Acid (DNA) is a polymer composed of monomer units known as nucleotides. Each nucleotide consists of a 5-carbon sugar (deoxyribose), a nitrogen containing base attached to the sugar, and a phosphate group. The deoxyribose is a five carbon sugar with a pentagonal structure. The phosphate in the DNA is hydrophilic and binds to the sugar. It has three reactive (-OH) groups of which two are involved in the formation of the sugar-phosphate backbone of each DNA strand. The hydrophobic bases are divided into two classes based on their chemical structure. Adenine (A) and guanine (G) are double ringed bases and are called purines, while pyrimidines are single ringed structures comprised of thymine (T) and cytosine (C). In the DNA polynucleotide strands, the nucleotides are joined with each other by '**phosphodiester linkages**' in which the phosphate group present at the C-5 of the sugar of one nucleotide gets attached to the C-3 of the sugar of the next nucleotide in the chain.

Bases

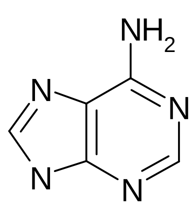


Adenine

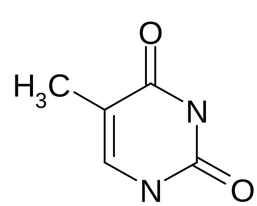


Thymine

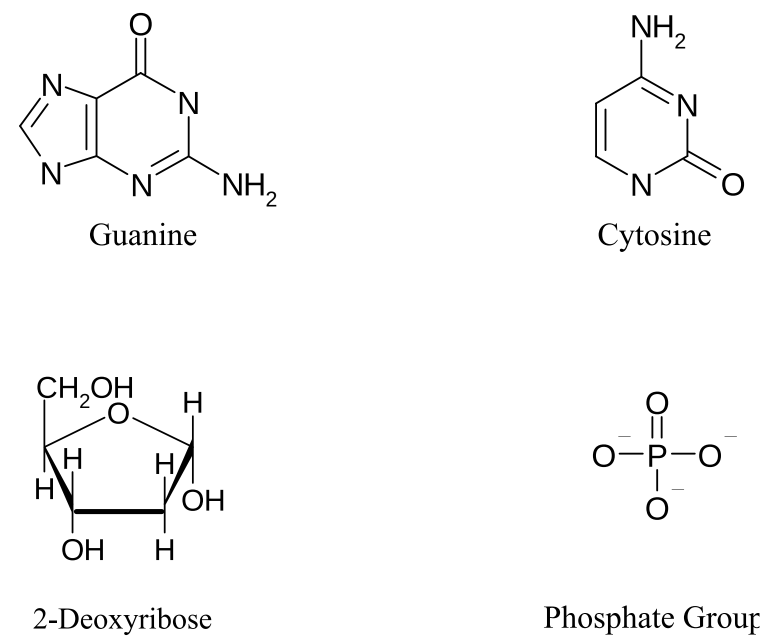


**Figure 1.2 A. Chemical components of DNA**

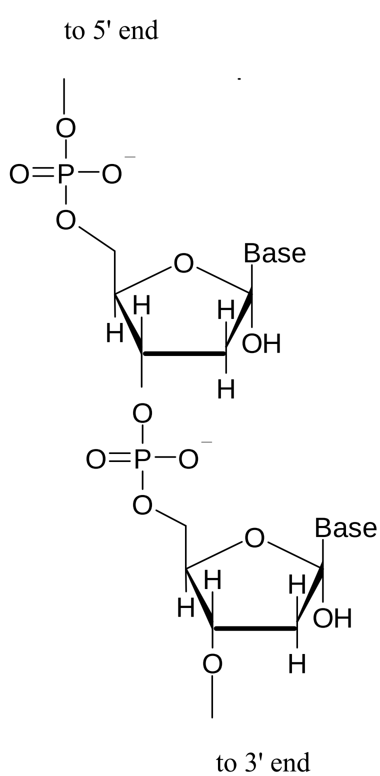


**Figure 1.2.B Phosphodiester linkage**

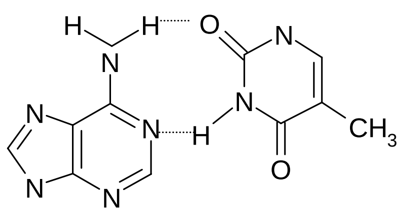

A - T

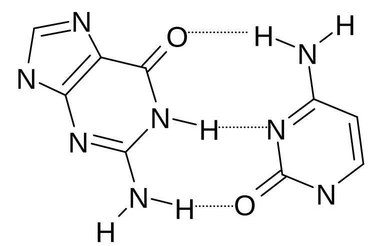

G - C

**Figure 1.3 Watson-Crick Interactions**

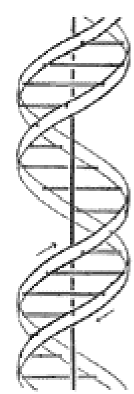



**Figure 1.4 B Form of DNA**

### 1.2.2 DNA hybridization and factors affecting hybridization efficiency

DNA hybridization is a process where two single strands of DNA that are complimentary to each other bind to each other through hydrogen bonding. The size of the nucleotide bases and the placement of the amino and carboxyl moeties on the ring make the pairing specific. Only a purine-pyrimidine base pair can be incorporated into the double helix at the right H-bonding distance. A G-C or A-T purine-pyrimidine pair has the moieties in the right position for bonding to occur. Purine-purine ring pairs would be too bulky and the pyrimidine-pyrimidine ring pairs too far for the formation of double helical structure. Figure 3 shows how adenine binds to thymine and guanine to cytosine through hydrogen bonds called as Watson-crick Interactions. As this bonding continues, the hydrophilic anionic phosphates turn themselves to the outer side while the hydrophobic bases orient themselves on the inner side forming a helical structure. James Watson and Francis Crick first described this structure in 1953. [1]

In 1961, nucleic acid hybridization technology first began with the work of Hall and Spiegelman. They hybridized the probe (oligonucleotide with known sequence) and target (oligonucleotide with unknown sequence) in solution and isolated the hybrids by equilibrium-density gradient centrifugation. [2]. But it was difficult to separate and free the hybridized oligos. It was not until the 1971 when surface-based hybridization detection assays were introduced to sequence and quantitate the unknown oligos. Immobilizing one of the oligos makes it easier to wash away the unreacted molecules, offering greater specificity. Immobilization of target oligo also prevents it from self-annealing while enabling the nucleic acid to form a hybrid when the probe is added in solution. The two broad categories in which the surface hybridization assays can grouped are – filter assays which use flexible and porous support membranes like nitrocellulose and nylon and microarrays which uses solid, nonporous support like metal or glass. The initial filter assays involved immobilizing the target on the support and exposing it to labeled probe solution, while in microarrays the probe is surface-bound and the target is labeled. Miller et al. in 1988 was the first group to use an unlabelled immobilized probe to capture a target RNA by hybridization. [2]. Incubation of the surface-bound probe and target is solution takes place under condition that favours duplex formation. There are parameters like temperature, length and composition of the oligo, salt concentration, formamide concentration and mismatch percentage between the two complimentary oligonucleotides that affect the hybridization efficiency and stability of the hybrid. Depending on the type of hybdridization assay employed the effect of the above mentioned parameters vary slightly. In this thesis, the focus is on surface-based hybridization assays (DNA microarrays).

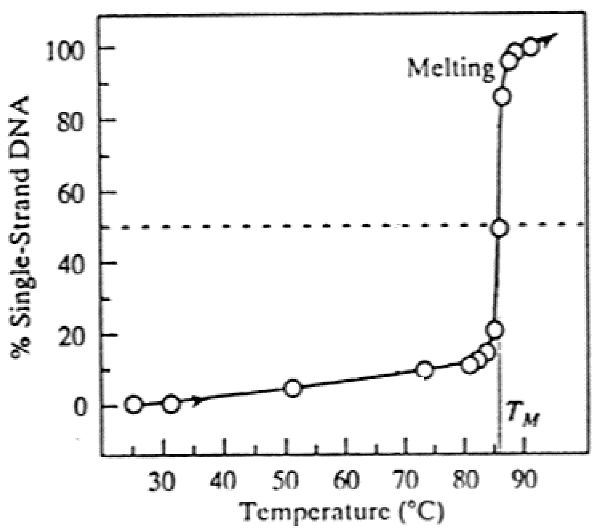


**Figure 1.5 Melting curve of DNA**

In a surface hybridization process, the single stranded target collides randomly with the surface-bound probe. When the complimentary strands according to the Watson-Crick pairing rule match up its called the "nucleation", following which the nucleic acids "zipper up" forming a double helical duplex. Zippering takes place rapidly compared to the nucleation event, which is the rate-limiting step for hybridization reaction. All the factors affecting the rate of hybridization and the stability of the hybrid is discussed in detail.

### 1.2.2.1 Nucleic Acid concentration

In theory, the rate of a reaction is proportional to the concentration of the reactants, i.e the concentration of the probe and the reactant. The overall reaction can be expressed in terms of depletion of target from the hybridization solution as:

$$\frac{-d[C_t]}{dt} = k[C_p][C_t] \tag{1.1}$$

where $-d[C_t]/dt$ is the rate at which target is depletes, k is the rate constant, $[C_p]$ is the concentration of the probe and $[C_t]$ is the target concentration. In theory the $[C_p]$ is not known accurately since a proportion of probe is not available for nucleation. At low concentration of probes the rate limiting step is nucleation while as at higher probe concentration the hybridization occurs rapidly and depletes the surrounding solution of the target strands and the diffusion of target to the probe becomes the rate-limiting step of the reaction. In case of DNA microarrays the target is in excess and so the rate of hybridization depends only on the probe concentration. To increase the hybridization rate higher probe concentration can be used but target diffusion has to be increased using smaller volumes and short lengths of oligos.

### 1.2.2.2 Salt concentrationtions

Monovalent cations like $[Na^+]$ stabilize the hybrid by electrostaticaly interacting with the DNA and its concentration in the hybridization buffers affects the rate of hybridization. Very mild changes in DNA hybridization rates were observed when salt concentration was changed from 0.4 M to 1.5 M. Typical DNA hybridization assays use 5xSSC (Saline sodium citrate) which is 0.9 M $[Na^+]$. To remove mismatched hybrids from the assay, washing with low salt concentration and high temperature (high stringency) is effective.

### 1.2.2.3 Temperature

The hybridization rate increases with the increase in temperature. The maximum hybridization rate is reached about 20-25 $^{o}C$ below the melting temperature, $T_m$ (the temperature at which 50% of the oligos are hybridized) of the hybrid and declines with further increase in the temperature. [3] Melting temperature for DNA: DNA hybrids in assays can be estimated by equation 1.2.

$$T_m = 81.5\ ^{o}C - 16.6\ (\log_{10}[M]) + 0.41(\%G{+}C) - 0.63\ (\%\ \text{Formamide}) - 600/L \qquad (1.2)$$

where [M] is the concentration of the monovalent cation, (%G+C) is the percentage of guanines and cytosines in the probe, (% Formamide) is the concentration of the formamide used in the hybridization solution and L is the chain length of the hybrid expressed in base pairs. The above equation holds true for [M] between 0.01-0.4 of monovalent cations and (%G+C) of 30-75 % and does not take base mismatch into account. As these relationships are derived from solution phase hybridization it can not predict the surface hybridizations accurately. It has been shown that in event of surface hybridization the Tm of the hybrid is lower than the solution. [4]

### 1.2.2.4 Length of the target

When the concentration of the probe on the surface is much larger than the concentration of the target, the hybridization kinetics are limited by the rate of diffusion of target. In such instance, shorter targets would ensure faster hybridization rate. Once the duplex is formed longer oligonucleotides form stable hybrid as more hydrogen bonds stabilize them.

### 1.2.2.5 Formamide Concentration

An average decrease of 0.63 $^{o}C$ per 1% formamide in $T_m$ is adopted for surface hybridization, from the calculated Tm for homopolymers hybrids in solution. Lowering the $T_m$ of the hybrid by formamide can be useful since incubation at high temperature run the risk of thermal degradation of the targets and desorption of probes from the surface.

### 1.2.2.6 Composition of oligo

The rate of hybridization increases to a very small extent as the (%G+C) increases in the target. But the stability of the hybrid is influenced greatly by the composition of the target. The GC base pair binds with three hydrogen bonds while the AT has only two hydrogen bonds. Hence GC base pairs offer grater stability to the hybrid and the effect of (%G+C) is seen in equation 2.2. A variation of 2-3% in GC composition of a hybrid can vary the melting temperature of the hybrid by 1 °C.

### 1.2.2.7 Mismatch Percentage

The rate of hybridization and $T_m$ will be reduced in presence of mismatches. Studies suggest that the rate of formation of hybrid under normal conditions would be reduced by a factor of two for every 10% mismatch [5] and the $T_m$ reduces by 1 °C for every 1% mismatch. The position of the mismatch base pair also affects the duplex stability and $T_m$.

### 1.2.2.8 Other Factors

There are other factors like pH of the hybridization buffer, time period of hybridization, reaction volume and presence of hybridization accelerators like polyethylene glycol

(PEG) affect the hybridization kinetics and also the stability of the hybrid, but has not been studied extensively.

## *1.3 History of Hybridization Assay*

With explosion of genomic information "one gene at a time" approach to gene expression had to be modified to accommodate monitoring of thousands of gene products simultaneously. Figure 1.6 shows the wealth of genetic information that can be procured from genetic analysis. Rapid sequencing of DNA for diagnostics and research purposes is the first level in understanding genomics. Functional genomics is the second means of gene expression analysis in which mRNA expression level is examined to identify target proteins and altering the gene expression in it. Proteomics – studying all the proteins expressed in a cell, is an excellent way to examine the proteins encoded by genes. Comparison of protein patterns in treated vs. untreated tissues can shed light on the disease causing proteins.

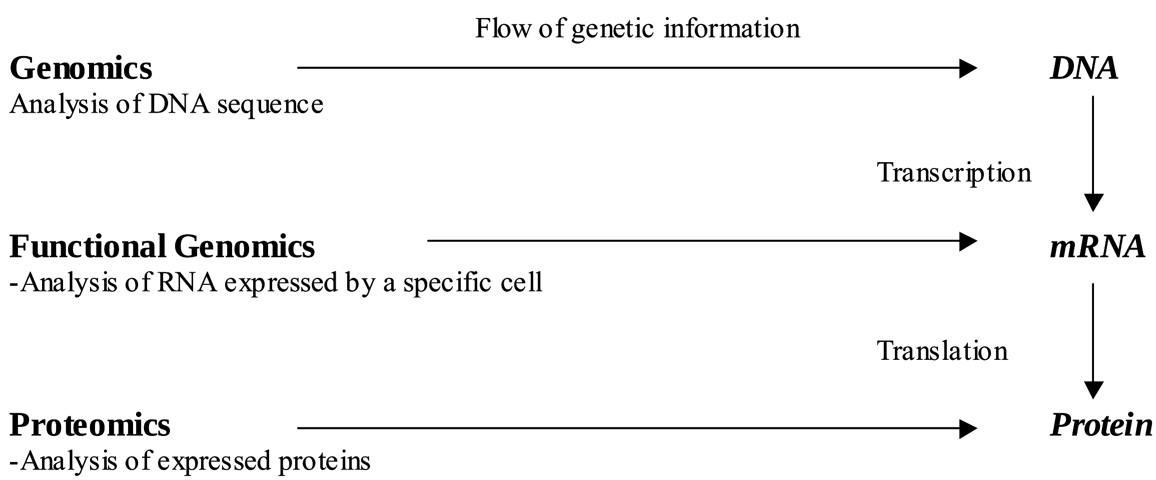


**Figure 1.6 Flow of genetic information chart**

DNA hybridization analysis in an array format provides a broad-based screen of gene expression by filtering through thousands of genes to identify physiologically important ones and to help understand patterns of gene expression and how the genes are regulated.

### 1.3.1 Southern Blotting Hybridization Assay

Hybridization of nucleic acids by immobilizing DNA on a substrate was first carried out by Southern Blotting Hybridization Assay. In spot blotting, crude or purified mixture of DNA is spotted on the surface of a derivatized nylon membrane or flexible nitrocellulose membrane, immobilized and detected by hybridization. The target is first obtained by digestion of genomic DNA by restriction enzymes. Gel electrophoresis has superior resolution properties hence used for fractionating the fragments. The DNA fragments that have been size fractionated can be identified by gel electrophoresis. The purified fragments (targets) separated by gel methods are transferred to a membrane support and this is known as southern transfer. The targets are then immobilized by baking or UV-crosslinking. These imbolized targets are exposed to a labeled solution of probes and hybridization is detected by autoradiography

### 1.3.2 DNA Microarrays

DNA microarrays or biochip assays utilize a solid substrate such as glass for immobilizing the probes and uses a fluorescence label to detect hybridization. The porous substrates used for filter hybridization needed a larger volume of sample and allows diffusion of the sample. In contrast solid substrates use small volumes, highly concentrated sample, and rapid hybridization kinetics. Non-porous substrates also prevent absorption of reagents and analytes into substarte matrix. Solid substrates provide exceptional quality of microarrays through uniform surface attachment chemistry and provide access to parallel analysis. The three major techniques used in manufacture of microarray are photolithography, ink-jetting and mechanical microspotting. Any of these three techniques can be used to immobilize thousands of DNA molecules of known sequences (probe) on the solid substrate in a high density in an array pattern. The array is exposed to a solution of mixture of unknown fluorescent-labeled targets. After washing the excess, the microaaray is developed by Confocal Scanning devices to determine the hybridization centers. The fluorescent emission is converted into digital output by suitable detectors. By comparing the pattern of fluorescence obtained and the known probe positions, the sequence of unknown targets can be determined in the given microarray. Active research is being carried out to develop oligonucleotide detection system, which is highly sensitive, and use inexpensive probes and monitoring equipments. Chad A. Mirkin *etal.* has studied both homogeneous and heterogeneous assays and developed nanoparticle based colorimetric and scanometric detection of oligonucleotides in an array format.

## *References*


1. Watson, J.D.C., F. H. C., Nature, 1953. **171**: p. 737-738.
2. George H. Keller, M.M.M., *DNA Probes*. 1989: Macmillan Publishers Ltd.
3. Beltz, G.A., Jacobs, K. A., Eickbush, T. H., Cherbas, P. T., and Kafatos, F. C., *Methods in enzymology*, ed. L.G. R. Wu, and U. Moldave. Vol. 100. 1983: Academic Press, NY. 266.
4. Kafatos, F.C., Jones, C. W., and Efstratiadis, A., Nucl. Acids. Res., 1979. **7**: p. 1541.

5. Bonner, T.I., Brenner, D. J., Neufield B. R., and Britten, R. J., J. Mol. Biol., 1973. **81**: p. 123.

# CHAPTER 2

# Detection of DNA hybridization on gold substrates by Polarization modulation infrared reflection absorption spectroscopy

# (PMIRRAS)

## Abstract

Polarization modulation infrared reflection absorption spectroscopy (PM-IRRAS) was used to detect DNA hybridization on gold surfaces. Mixed monolayers of 6-mercapto-1-hexanol (MCH) and single stranded DNA (ssDNA) with a C6-SH 5' modifier was first formed on the gold surface by co-deposition. Then hybridization with the complementary ssDNA strand was performed to obtain double stranded (dsDNA). The PM-IRRAS spectra obtained contained absorptive features indicative of DNA arising from the phosphodiester backbone and the purine and pyrimidine rings. An infrared signature of dsDNA was observed at 1655 $cm^{-1}$ that was absent in the ssDNA spectra. This band permitted the distinction between ssDNA and dsDNA to be made thus allowing for the detection of DNA hybridization on gold surfaces by PM-IRRAS.

## 2.1 Introduction

The detection of DNA hybridization on surfaces is an area of intense current investigation. A number of methods have recently been employed for analysis of surface hybridization including fluorescence,[1-4] chronocoulometry,[5-7] surface plasmon resonance[8,9] and colloidal labeling of nanoparticles.[10-12] The hybridization of DNA on gold surfaces is of particular interest because of the wide use of self-assembled monolayers on gold. However, despite the well-developed application of grazing angle Fourier transform infrared spectroscopy[13,14] there has been no direct detection of DNA hybridization on self-assembled monolayers of DNA. There have been numerous experimental studies on the DNA bases by infrared spectroscopy[15-25] and non-resonant[16,21,25-31] and resonant Raman spectroscopy.[32-36] These studies include using vibrational spectroscopy to probe B, A, and Z DNA forms[37-42] and to study drug and protein binding to DNA.[43-46] The vibrational spectra and energetics of the individual nucleic acids and the AT and GC base pairs have also been studied by semiempirical and DFT calculations.[47-49]

Self-assembled monolayers (SAMs) of DNA are prepared as mixed monolayers from a co-deposition solution of 6-mercapto-1-hexanol and single stranded DNA (ssDNA) followed by surface hybridization with the complementary ssDNA.[50] Here we report the first direct detection of DNA hybridization on a gold surface using polarization modulation infrared reflection absorption spectroscopy (PM-IRRAS). . The advantages of PM-IRRAS are threefold. First, labeling of the DNA with fluorescent tags or radioisotopes is not required. This technique is also non-intrusive allowing quick determination of the presence of single stranded DNA (ssDNA) or double stranded DNA (dsDNA) on the surface without contaminating the sample with an electrochemical agent. Thirdly, this technique can distinguish between the A, B, and Z forms of dsDNA on the surface. Single-pass attenuated total reflection (ATR)-FTIR spectra were taken of the ssDNA and dsDNA samples to verify the modes obtained with PM-IRRAS. ATR-FTIR spectra were also taken at various levels of hydration to determine the degree of hydration of the DNA strands on the surface. These comparisons provide an experimental link between bulk samples and analytical applications for detecting 10 picomoles (based on the surface coverage of DNA and the sampling area of PM-IRRAS) of DNA or less on a surface.[10] The experiments performed here establish the application of grazing angle FTIR spectroscopy to the observation DNA hybridization and detection of DNA-drug interactions using surface-attached DNA. Density Functional Theory (DFT) calculations of the individual DNA bases and base pairs were performed to yield calculated frequency spectra of ssDNA and dsDNA that were in excellent agreement with experimentally observed bands.

## *2.2 Methods and Materials*

### 2.2.1 DNA Monolayer Formation.

The mixed self-assembled monolayers (SAM) were prepared on clean polycrystalline gold deposited on a glass slide containing a chromium oxide passivation layer (Evaporated Films, Inc., cleaned with piranha solution (70% conc. $H_2SO_4$: 30%$H_2O_2$ (30%) (CAUTION, piranha solution reacts violently with organic chemicals) and rinsed with millipore 18 MΩ deionized water (BARNSTEAD E-PURE). The single-stranded DNA (ssDNA) (Applied Biosystems) probe strand was modified at the 5' end with a C6-S-disulfide modifier (Applied Biosystems). The ssDNA was deprotected to form the C6-SH linker as described elsewhere.[10] A co-deposition solution of 6-mercapto-1-hexanol (MCH) (Sigma-Aldrich) and ssDNA (probe strand) was used to form the mixed SAM on the gold surface with a 0.10 mole fraction of ssDNA in a 1μM MCH solution in 1 M potassium phosphate buffer (pH 7.0) for 16 hours at room temperature as shown in Figure 2.1 A. In some studies discussed in this dissertation another method of deposition of ssDNA and MCH on the gold substrate was employed. This is called "sequential" deposition method in which the cleaned gold slide was first incubated in a 1 μM ssDNA probe solution in 1 M potassium phosphate buffer (pH 7.0) for 16 hours at room temperature. The DNA modified gold substrate was then exposed to 1mM MCH solution in water for an hour. The schematic step by step deposition scheme is shown in Figure 2.1 B. The gold slides were then rinsed with 18 MΩ deionized water and placed in a 1X SSC (saline sodium citrate) (Fisher Scientific) at 65°C for one hour and then cooled to room temperature over four additional hours with or without target ssDNA (exact complement to the probe ssDNA on the gold surface) for hybridization (2.5 nmol of target ssDNA). The surfaces were then rinsed in 18 MΩ deionized water and dried with nitrogen gas. Both ssDNA strands were comprised of 30 bases and the probe strand had a sequence of 5'-GGAGACTGTTATCCGCTCACAATTCCACAC-3' and the target ssDNA was the exact complement of the probe ssDNA strand. The solution hybridization mixture, containing the two complementary ssDNA strands (in 1X SSC), was heated to 85°C for five minutes and then cooled to room temperature for 30 minutes to obtain dsDNA for solution FTIR measurements. The excess salt from the dsDNA solution was removed using Centricon YM-3 centrifugal filter units (Millipore) and 18 MΩ deionized water as the wash solvent.

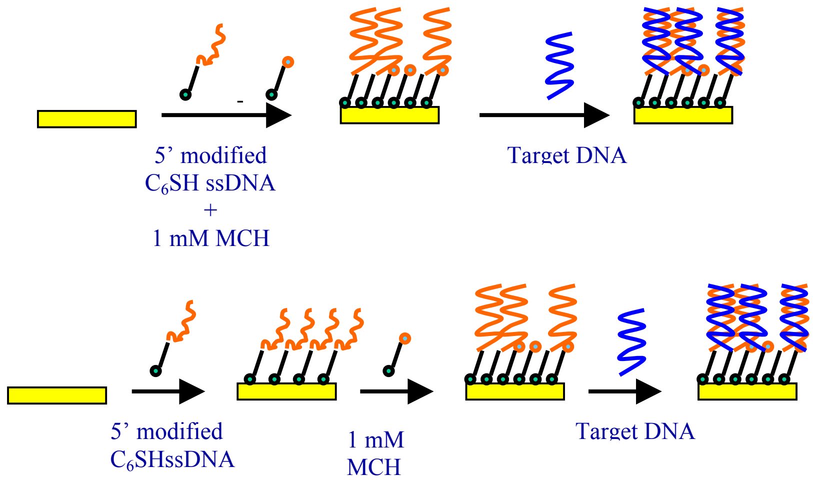


**Figure 2.1 Formation of DNA monolayer by A. Codeposition route B. Sequential route**

### 2.2.2 Polarization Modulation Infrared Reflection Absorption Spectroscopy (PM-IRRAS)

The PM-IRRAS spectra were recorded on a Bio-Rad FTS 7000 spectrometer equipped with a step scan interferometer, liquid nitrogen cooled narrow band MCT detector, globar source, and a UDR-8 filter. The IR radiation was typically phase modulated at frequencies of 400 or 800Hz at an amplitude of 1.0 or 2.0 λ HeNe while stepping at 0.5 - 2.5 Hz. A gold grid polarizer was used to obtain either s- or p-polarized radiaton, which was then modulated by a Hinds ZnSe PEM operating at 37 KHz and amplitude of 0.5 λ (strain axis 45 degrees to the polarizer) before reflecting off the sample at an incident angle of 80 degrees from the surface normal. The spectra were recorded at room temperature at a resolution of 8 $cm^{-1}$ and were the result of 4 scans with a spectral range of 900 – 1800 $cm^{-1}$. The digital signal processing (DSP) algorithm incorporated into the Bio-Rad spectrometer software was used to obtain the spectra. This instrument allowed the gold slide containing the monolayer to also be the reference to obtain the absorption spectra. The solution single-pass ATR FTIR spectra of the DNA (~20 – 200mM) were taken using an IR microscope (model number UMA-500) attached to a Bio-Rad Digilab FTS 6000 FTIR spectrometer equipped with a Cassegranian objective containing a germanium crystal for single-pass attenuated total reflection (ATR). The spectrometer was equipped with a liquid nitrogen cooled MCT/A detector and the spectra were recorded at a resolution of 2 $cm^{-1}$ with a spectral range of 650 - 4000 $cm^{-1}$. The absorption spectra were the result of the average of multiplies of 64 scans and were recorded at room temperature.

### 2.2.3 Density Functional Theory (DFT) Calculations.

The geometry optimization and vibrational frequency calculations of the individual DNA bases and complementary base pairs were done using the MSI (Molecular Simulations, Inc) quantum chemistry software program DMol3 at the North Carolina Supercomputer Center (NCSC) on either the IBM RS/6000 SP. DMol3 is an ab initio (first principles) software package that utilizes density functional theory.[51] These calculations were done in the gas phase using the DNP basis set, the GGA functional, and the method of finite differences for calculating the vibrational frequencies. The MSI software Insight II was used to build the models and to visualize the eigenvector projections of the vibrational modes of the models.

## *2.3 Results and Discussion*

Figure 2.2 A and 2.2 B show the PM-IRRAS spectra corresponding to the mixed monolayer of MCH and ssDNA before and after hybridization with the complementary ssDNA with a hybridization temperature of 65°C and 85°C respectively recorded at an incident angle of 80 degrees. The hybridization temperature was varied to obtain efficient hybridization while minimizing ssDNA strand loss from the gold surface. The ssDNA and dsDNA spectra contain absorptive features indicative of DNA for both temperatures. For instance, the modes centered at 1082 and 1238 $cm^{-1}$ correspond to the symmetric and asymmetric $PO_2^-$ group of the DNA phosphodiester backbone.[52,53] The mode centered at 1188 $cm^{-1}$ is a well-known deoxyribose structural marker mode. [54] The combination of the asymmetric $PO_2^-$ group mode at 1238 $cm^{-1}$ and the deoxyribose mode at 1188 $cm^{-1}$ is indicative of A-form DNA structure consistent with the low humidity environment in the current PM-IRRAS configuration.[54,55] The modes at 1464 and 1514 $cm^{-1}$ result from the purine and pyrimidine (DNA bases) ring modes,[52,53] while the region from 1600 – 1750 $cm^{-1}$ is due to carbonyl (C=O), C=N stretching and exocyclic -$NH_2$ bending vibrations in the DNA bases.[52,56] However, the intensities of these bands are not the same at 65°C and 85°C due to the quantity and orientation of the DNA on the surface. The intensity for the ssDNA and dsDNA spectra for 85°C is lower than the corresponding spectra with a hybridization temperature of 65°C. This observation suggests that strand loss is occurring at the higher temperature due to thiolate desorption.

The major distinction between the PM-IRRAS spectra for ssDNA and dsDNA in Figures 2.2A and 2.2 B is the presence of a band at 1655 $cm^{-1}$ in the dsDNA spectra, which is absent in the ssDNA spectra. This distinction is observed at both hybridization temperatures. The intensity change in this region represents changes in hydrogen bonding between complementary bases that occur upon formation of a double helix and the quantity of DNA on the surface.[52] The infrared signature at 1655 $cm^{-1}$ of dsDNA thus permits the detection of DNA hybridization on gold surfaces by PM-IRRAS.

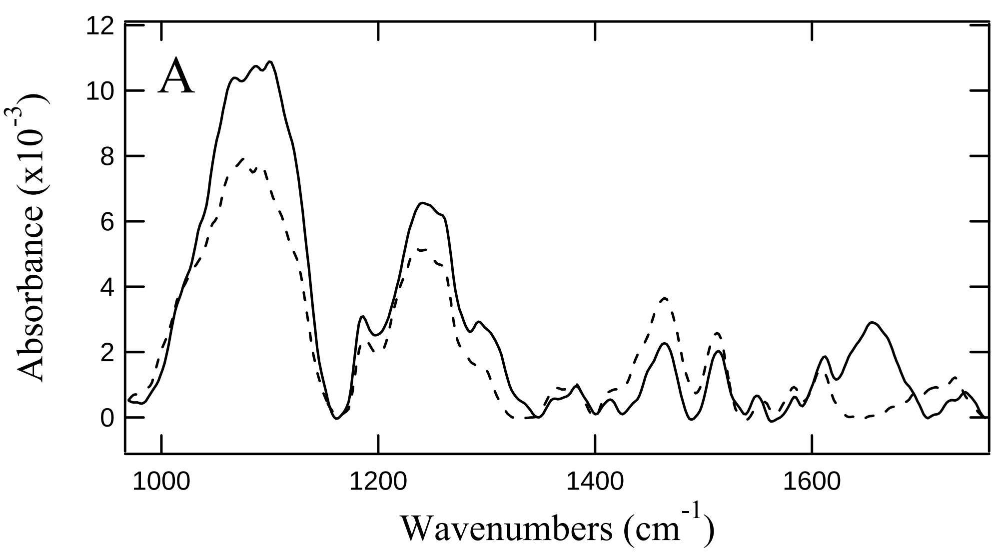

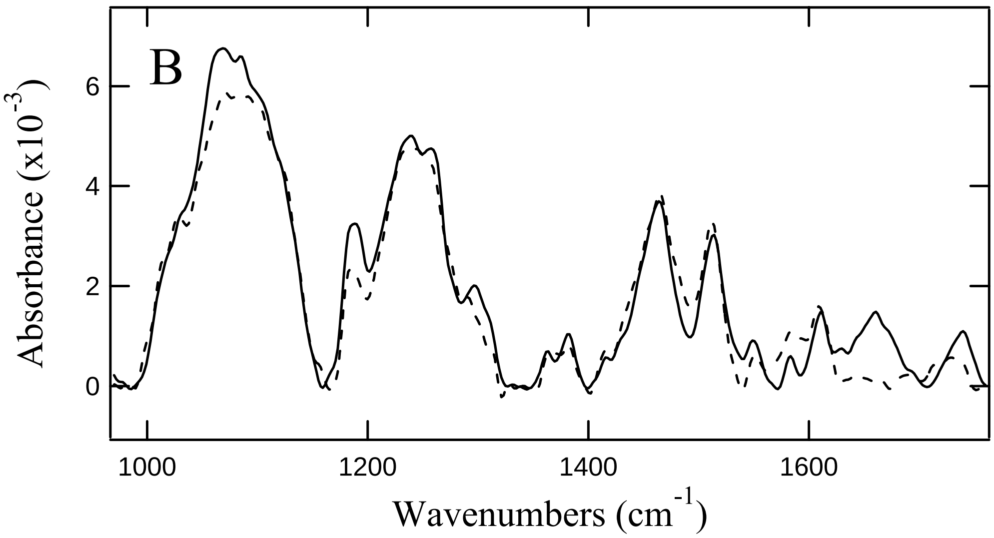


**Figure 2.2 PM-IRRAS spectra of a mixed monolayer of 6-mercapto-1-hexanol and single stranded DNA before (dashed spectrum) and after hybridization (solid spectrum) with the complementary single stranded DNA strand to obtain double stranded DNA with a hybridization temperature of 65°C (A) or 85°C (B) recorded at an incident angle of 80 degrees.**

Figure 2.3 shows the single-pass ATR FTIR spectra of ssDNA and dsDNA strands in aqueous solution to verify the absorptive features observed in the PM-IRRAS spectra of ssDNA and dsDNA are due to these DNA species. These spectra contain similar features as seen in the PM-IRRAS spectra corresponding to these species on a gold surface. However the absorptive features present in Figure 2.3 for ssDNA and dsDNA are not identical due to the hydrogen bonding between complementary bases in the dsDNA.[52] The features can be assigned, as done above, to arising from the phosphodiester backbone and the purine and pyrimidine rings of the DNA bases. However, ssDNA has two modes in the high frequency region at 1594 and 1681 $cm^{-1}$ that are replaced with a single mode at 1658 $cm^{-1}$ in dsDNA. Therefore ssDNA and dsDNA can be distinguished in both solution and on the gold surface using infrared spectroscopy. The sample conditions under single-pass ATR-FTIR resemble those of a hydrated DNA fiber. [54]

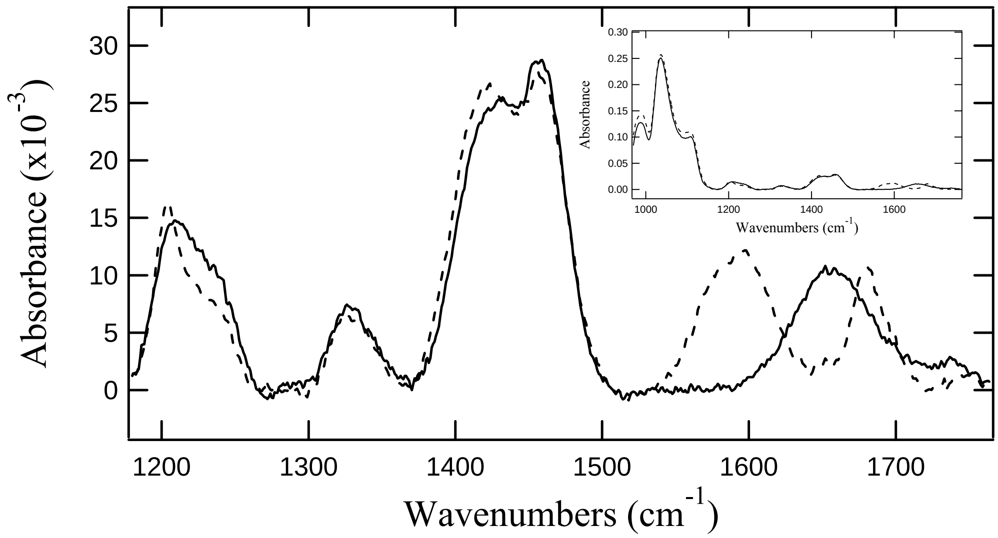


**Figure 2.3. Solution single-pass ATR FTIR spectra of single stranded DNA (dashed spectrum) and double-stranded DNA (solid spectrum) corresponding to the same DNA strands used for the probe and target single stranded DNA on the gold surfaces. The concentration of the DNA solutions was approximately 200mM. The inset shows the larger spectral range from 970 - 1760 $cm^{-1}$.**

Figure 2.4 shows the single-pass ATR FTIR spectra of ssDNA in aqueous solution as a function of hydration to estimate the amount of hydration in the DNA monolayers on the gold surfaces. Initially, the bending vibration mode of water at 1638 $cm^{-1}$ masks the carbonyl and amino hydrogen bonding region of the spectra and the other modes in the spectra cannot be discerned due to a low concentration of DNA.[17] However, as the water begins to evaporate the concentration of the DNA in the IR radiation path begins to increase and the masking bending mode of water begins to decrease. Finally, only water of hydration is present in the sample permitting observations of the absorptive features of the DNA. Based on the absence of the water bending mode in the PM-IRRAS spectra, it can concluded that only the water of hydration is present on the gold surface of the DNA monolayers.

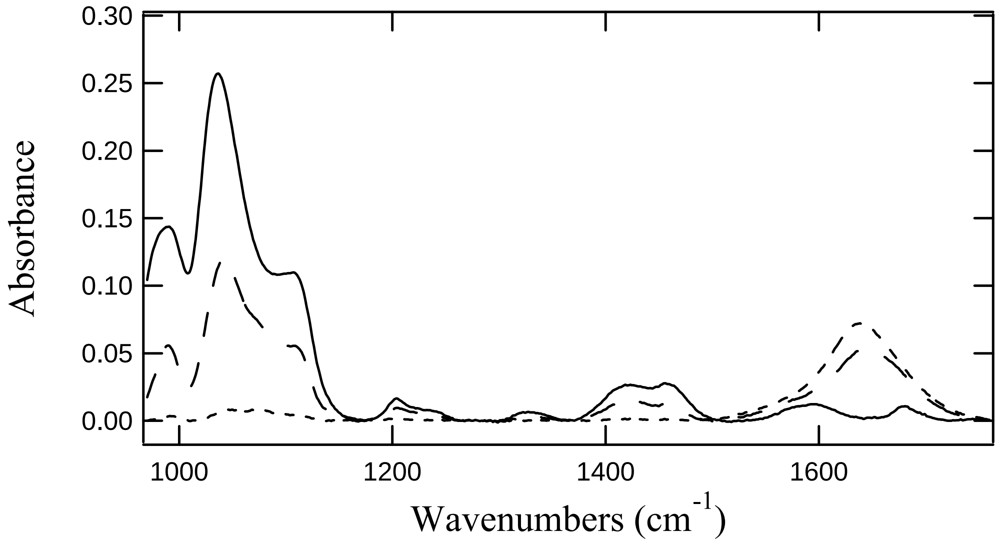


**Figure 2.4. Solution single-pass ATR FTIR spectra of single stranded DNA recorded as a function of hydration and concentration in aqueous solution. The spectra correspond to least concentrated ~20 mM (- - -), more concentrated (-- -- --), and most concentrated ~200 mM (solid spectrum) of the single stranded DNA used as the probe strand on the gold surfaces. The most concentrated sample is nearly in a gel state.**

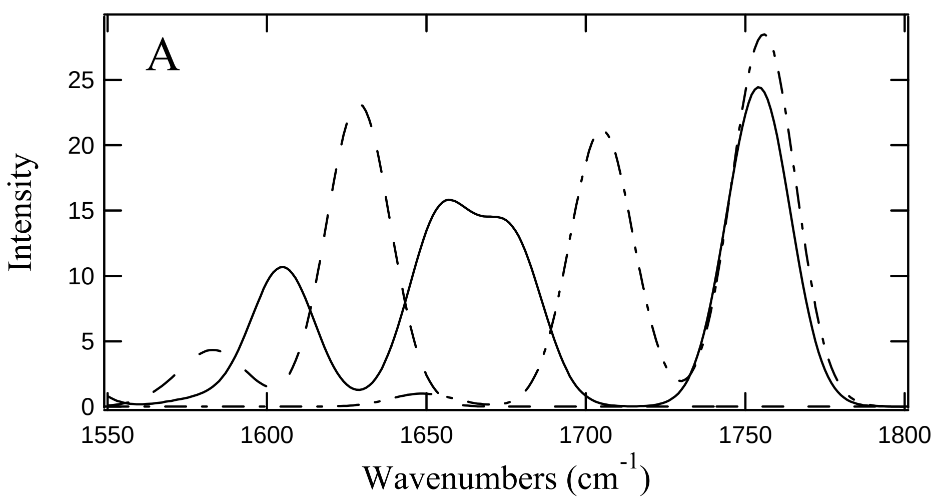

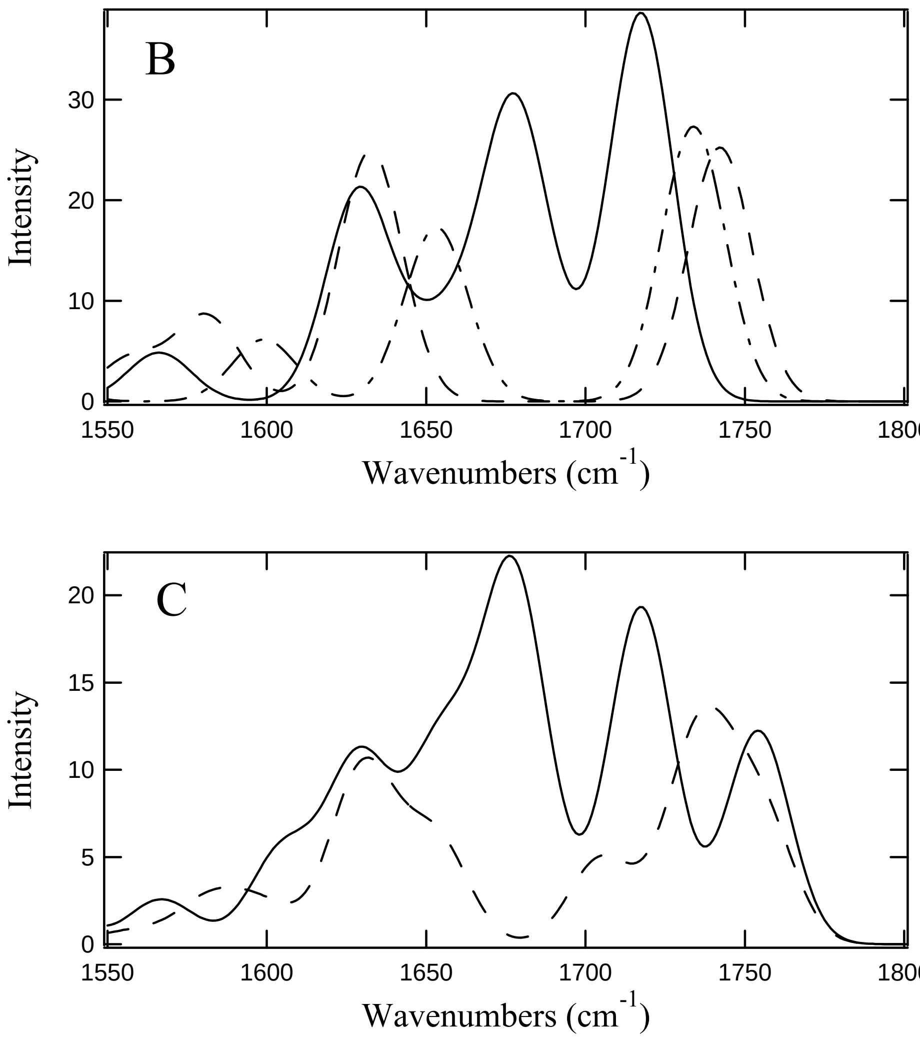


**Figure 2.5. Dmol3 calculated frequency spectra of A. adenine (-- --), thymine (-- ˙ --, and the adenine-thymine base pair (solid spectrum), B. guanine (-- --), cytosine (-- ˙ --), and the guanine-cytosine base pair (solid spectrum), C. probe ssDNA before (dashed spectrum) and after hybridization (dsDNA) (solid spectrum) using the weighted average of the calculated spectra of either the individual bases or base pairs, respectively. All spectra have a Gaussian width of 20 $cm^{-1}$.**

Figure 2.5 shows the density functional theory (DFT) calculated frequency spectra of the individual DNA bases, DNA base pairs, and their weighted average to obtain calculated frequency spectra corresponding to the ssDNA and dsDNA used in the DNA monolayers on gold. Figure 2.5 A specifically shows the DFT calculated vibrational spectrum of adenine, thymine, and the adenine-thymine (AT) base pair in the 1550 – 1800 $cm^{-1}$ region. The adenine calculated spectrum has three modes at 1572, 1584, and 1629 $cm^{-1}$ due mostly from $NH_2$ bending (and some ring deformation). The thymine calculated spectrum has a mode at 1649 $cm^{-1}$ due to C-C stretching and two modes at 1705 and 1756 $cm^{-1}$ resulting from carbonyl stretching. The calculated spectrum of the AT base pair resulted in four modes at 1605, 1655, 1676, and 1754 $cm^{-1}$. The modes at 1605 and 1655 $cm^{-1}$ result from $NH_2$ bending, the mode at 1642 $cm^{-1}$ is a ring deformation mode, the mode at 1676 $cm^{-1}$ results from N-H bending, while the mode at 1754 $cm^{-1}$ results from a carbonyl stretching motion. These spectra illustrate a blue shift of the $NH_2$ bending modes upon base pair formation due to hydrogen bonding which involves this group. The $NH_2$ bending motion of adenine becomes more constrained in the base pair and hence the frequency of the $NH_2$ bend increases. The carbonyl stretching frequency of the carbonyl group of thymine involved in hydrogen bonding in the AT base pair decreases in frequency upon base pair formation. This red shift is the result of a weakening of the C=O force constant due to hydrogen bonding. The other carbonyl stretching frequency of thymine decreases minimally since this carbonyl group is not involved in hydrogen bonding with adenine in the AT base pair. These shifts are in qualitative agreement with previous semiempirical calculations.[47]

Figure 2.5 B shows the DFT calculated frequency spectra of guanine, cytosine, and the guanine-cytosine (GC) base pair in the region of 1550 – 1800 $cm^{-1}$. The calculated spectrum of guanine shows two modes at 1582 and 1632 cm-1 primarily due to $NH_2$ bending and one carbonyl stretching mode at 1742 $cm^{-1}$. The cytosine calculated frequency spectrum shows two modes at 1524 and 1653 $cm^{-1}$ resulting from ring deformation (and C=N stretching), a mode at 1599 $cm^{-1}$ due to $NH_2$ bending, and a carbonyl stretching mode at 1733 $cm^{-1}$. The GC base pair calculated frequency spectrum shows six modes at 1565 ($NH_2$ and N-H bending, carbonyl stretching), 1628 and 1634 (primarily $NH_2$ and N-H bending, small component of carbonyl stretching and ring deformation), 1676 ($NH_2$ bending, carbonyl stretching), and 1684 and 1717 $cm^{-1}$ ($NH_2$ and N-H bending, carbonyl stretching). Similar to the calculated spectrum of the AT base pair relative to the spectra of the individual bases, the GC calculated spectrum shows a blue shift in the $NH_2$ (and N-H) bending frequency and a red shift in the carbonyl stretching frequency for those groups involved in hydrogen bonding in the GC base pair relative to the individual bases.

Figure 2.5 C shows the DFT calculated frequency spectra corresponding to the probe ssDNA strand and the dsDNA (after hybridization with target ssDNA) strand used in the monolayers on gold in the 1550 – 1800 $cm^{-1}$ region. These spectra were obtained by weighting the individual (for ssDNA) or the base pairs (for dsDNA) spectra in the appropriate amount corresponding to the sequence of the probe and target ssDNA strands used. These show the $NH_2$ and N-H bending modes and the carbonyl stretching frequencies as discussed above for the individual bases and base pairs. The main difference between these two spectra is the existence of an infrared signature mode at 1655 $cm^{-1}$ in the dsDNA spectrum that is absent in the calculated ssDNA spectrum. This result is consistent with the observed differences in the surface and bulk FTIR spectra of the corresponding ssDNA and dsDNA strands. The models and the eigenvector projections of these modes are in the Supplementary Materials.

## 2.4 Conclusion

Polarization modulation infrared reflection absorption spectroscopy (PM-IRRAS) was successfully used to detect DNA hybridization on a gold surface. The most pronounced spectral changes between ssDNA and dsDNA are in the nucleobase hydrogen bonding region from 1550 $cm^{-1}$ to 1720 $cm^{-1}$. Surface hybridization was detected by an increase in absorption intensity at 1655 $cm^{-1}$ in dsDNA. Comparison of the single-pass ATR-FTIR spectra of ssDNA solutions with the PM-IRRAS method showed that a minimal amount of water was present in the DNA monolayers on gold due to the absence of the water bending mode, $\nu_{H\text{-}O\text{-}H}$, at 1638 $cm^{-1}$ in the PM-IRRAS spectra. This observation is significant because, if present, $\nu_{H\text{-}O\text{-}H}$ masks the region of the DNA spectrum that contains the most information. The spectral features of surface attached DNA are similar to those of fiber DNA at low humidity.[54] However, ssDNA does not form fibers and thus the conversion of ssDNA to dsDNA cannot be detected by FTIR spectroscopy so that the observed spectral changes associated with hybridization reported here are unique. The PM-IRRAS spectra were in excellent agreement with DFT calculated spectra of dsDNA and ssDNA. The calculated frequency spectra of the DNA bases and base pairs show that the difference between ssDNA and dsDNA results from the blue shift of the $NH_2$ and N-H bending modes and a red shift in the carbonyl stretching frequency due to hydrogen bonding between the complementary bases. These changes permit detection of DNA hybridization on samples for which the surface coverage is $4 \times 10^{12}$ molecules/$cm^2$.[10] The measurements shown in Figure 2.2 demonstrate the feasibility of detecting DNA hybridization on samples with this surface coverage. These results suggest that the PM-IRRAS technique can be used to observe binding events to surface-immobilized DNA or RNA. The fact that A-form structure is observed in the spectra presented here indicates that the current configuration can be used directly to observe binding events to surface-immobilized RNA. The PM-IRRAS method can be used in theory in high humidity conditions favoring B-form DNA. Thus, in addition to the detection of DNA hybridization, PM-IRRAS has the potential for use in the study of protein and drug binding to RNA and DNA.

## *Acknowledgements*

This work was done in collabration with Stefan Franzen, Scott Brewer, Simon Lappi and David Draphco and was the subject of publication, in Langmuir, 2002. Selina Moses was supported by Applied Biosystems Ltd.

## *References*

1)Fodor, S. P. A.; Read, J. L.; Pirrung, M. C.; Stryer, L.; Lu, A. T.; Solas, D. *Science* **1991**, *251*, 767-773.
2)Lockhart, D. J.; Winzeler, E. A. *Nature* **2000**, *405*, 827-836.
3)Bulyk, M. L.; Gentalen, E.; Lockhart, D. J.; Church, G. M. *Nature Biotechnology* **1999**, *17*, 573-577.
4)Chee, M.; Yang, R.; Hubbell, E.; Berno, A.; Huang, X. C.; Stern, D.; Winkler, J.; Lockhart, D. J.; Morris, M. S.; Fodor, S. P. A. *Science* **1996**, *274*, 610-614.
5)Esch, M. B.; Locascio, L. E.; Tarlov, M. J.; Durst, R. A. *Anal. Chem.* **2001**, *73*, 2952-2958.
6)Steel, A. B.; Herne, T. M.; Tarlov, M. J. *Anal. Chem.* **1998**, *70*, 4670-4677.
7)Steel, A. B.; Herne, T. M.; Tarlov, M. J. *Bioconjugate Chemistry* **1999**, *10*, 419-423.
8)He, L.; Musick, M. D.; Nicewarner, S. R.; Salinas, F. G.; Benkovic, S. J.; Natan, M. J.; Keating, C. D. *J. Am. Chem. Soc.* **2000**, *122*, 9071-9077.
9)Brockman, J. M.; Frutos, A. G.; Corn, R. M. *J. Am. Chem. Soc.* **1999**, *121*, 8044-8051.
10)Sauthier, M.; Carroll, R.; Gorman, C.; Franzen, S. *Langmuir* **2001**, *in press*.
11)Cao, Y. W.; Jin, R.; Mirkin, C. A. *J. Am. Chem. Soc.* **2001**, *123*, 7961-7962.

12)Demers, L. M.; Mirkin, C. A.; Mucic, R. C.; Reynolds, R. A.; Letsinger, R. L.; Elghanian, R.; Viswanadham, G. *Anal. Chem.* **2000**, *72*, 5535-5541.
13)Allara, D.; Nuzzo, R. *Langmuir* **1985**, *1*, 52-66.
14)Allara, D.; Nuzzo, R. *Langmuir* **1985**, *1*, 45-52.
15)Chin, S.; Scott, I.; Szczepaniak, K.; Person, W. B. *J. Am. Chem. Soc.* **1984**, *106*, 3415-3422.
16)Delabar, J. M.; Majoube, M. *Spectrochim. Acta* **1978**, *34A*, 129-140.
17)Falk, M.; Hartman, K. A.; Lord, R. C. *J. Am. Chem. Soc.* **1963**, *85*, 387-391.
18)Graindourze, M.; Smets, J.; Zeegers-Huyskens, T. H.; Maes, G. *J. Mol. Struct.* **1990**, *222*, 345-364.
19)Hirakawa, A. Y.; Okada, H.; Sasagawa, S.; Tsuboi, M. *Spectrochim. Acta* **1985**, *41A*, 209-216.
20)Kyogoku, A. Y.; Higuchi, S.; Tsuboi, M. *Spectrochim. Acta* **1967**, *23A*, 969-.
21)Lewis, T. P.; Miles, H. T.; Becker, E. D. *J. Phys. Chem.* **1984**, *88*, 3253-3260.
22)Thijs, R.; Zeeger-Huyskens, T. *Spec. Acta* **1984**, *40A*, 307-313.
23)Thomas Jr., G. J. *Biopolymers* **1969**, *7*, 325-334.
24)Tsuboi, M.; Kyogoku, Y.; Shimanouchi, T. *Biochim. Biophys. Acta* **1962**, *55*, 1-12.
25)Tsuboi, M.; Takahashi, S.; Harada, I. *Infrared and Raman spectra of nucleic acids - Vibrations in the base residues*; Tsuboi, M.; Takahashi, S.; Harada, I., Ed.; Academic Press: Lodon, 1973; Vol. 2, pp 92-143.
26)Lane, M. J.; Thomas Jr., G. J. *Biochemistry* **1979**, *18*, 3839-3846.
27)Lord, R. C.; Thomas Jr., G. J. *Spectrochim. Acta* **1967**, *23A*, 2551-2591.
28)Lord, R. C.; Thomas Jr., G. J. *Biochim. Biophys. Acta* **1967**, *142*, 1-11.
29)Nishimura, Y.; Tsuboi, M.; Nakano, T.; Higuchi, S.; Sato, T.; Shida, T.; Uesugi, S.; Ohtsuka, E.; Ikehara, M. *Nucl. Acids Res.* **1983**, *11*, 1579-1588.
30)Nishimura, Y.; Tsuboi, M.; Sato, T. *Nucl. Acids Res.* **1984**, *12*, 6901-6908.
31)Peticolas, W. A.; Kubasek, W. L.; Thomas, G. A.; Tsuboi, M. *Nucleic Acids*; Peticolas, W. A.; Kubasek, W. L.; Thomas, G. A.; Tsuboi, M., Ed.; John Wiley and Sons: New York, 1987; Vol. 1, pp 82-133.
32)Ziegler, L. D.; Hudson, B.; Strommen, D. P.; Peticolas, W. L. *Biopolymers* **1984**, *23*, 2067-2081.
33)Tsuboi, M.; Nishimura, Y.; Hirakawa, A. Y.; Peticolas, W. L. *Resonance Raman spectroscopy and normal modes of the nucleic acid bases*; Tsuboi, M.; Nishimura, Y.; Hirakawa, A. Y.; Peticolas, W. L., Ed.; John Wiley and Sons: New York, 1988; Vol. 2, pp 109-179.
34)Toyama, A.; Takino, Y.; Takeuchi, H.; Harada, I. *J. Am. Chem. Soc.* **1993**, *115*, 11092-11098.
35)Toyama, A.; Kurashiki, E.; Watanabe, Y.; Takeuchi, H.; Harada, I. *J. Am. Chem. Soc.* **1991**, *113*, 3615-3616.
36)Fodor, S. P. A.; Rava, R. P.; Hays, T. R.; Spiro, T. G. *J. Am. Chem. Soc.* **1985**, *107*, 1520-1529.
37)Pohl, F. M.; Ranade, A.; Stockburger, M. *Biochim. Biophys. Acta* **1973**, *335*, 85-92.
38)Erfurth, S. C.; Kiser, E. J.; Peticolas, W. L. *Proc. Natl. Acad. Sci.* **1972**, *69*, 938-941.
39)Erfurth, S. C.; Bond, P. J.; Peticolas, W. L. *Biopolymers* **1975**, *14*, 1245-1257.
40)Benevides, J. M.; Thomas Jr., G. J. *Nucl. Acids Res.* **1983**, *11*, 5747-5761.
41)LaFleur, L.; Rice, J.; Thomas Jr., G. J. *Biopolymers* **1972**, *11*, 2423-2437.

42)Thamann, T. J.; Lord, R. C.; Wang, A. H. J.; Rich, A. *Nucl. Acids Res.* **1981**, *9*, 5443-5457.
43)Lu, D. S.; Nonaka, Y.; Tsuboi, M.; Nakamoto, K. *J. Raman Spec.* **1990**, *21*, 321-326.
44)Takeuchi, H.; Sasamori, J. *Biopolymers* **1995**, *35*, 359-367.
45)Hud, N. V.; Milanovich, F. P.; Balhorn, R. *Biochemistry* **1994**, *33*, 7528-7535.
46)Grygon, C. A.; Spiro, T. G. *Biochemistry* **1989**, *28*, 4397-4402.
47)Hrouda, V.; Florian, J.; Hobza, P. *J. Phys. Chem.* **1993**, *97*, 1542-1557.
48)Florian, J.; Leszczynski, J.; Johnson, B. G. *J. Mol. Struc.* **1995**, *349*, 421-426.
49)Guerra, C.; Bickelhaupt, F.; Snijders, J.; Baerends, E. *J. Am. Chem. Soc.* **2000**, *122*, 4117-4128.
50)Herne, T. M.; Tarlov, M. J. *J. Am. Chem. Soc.* **1997**, *119*, 8916-8920.
51)Delley, B. *J. Phys. Chem.* **1990**, *92*, 508-517.
52)Tsuboi, M. *Prog. Theor. Phys. Supp.* **1961**, *17*, 99-107.
53)Falk, M.; Hartman, K. A.; Lord, R. C. *J. Am. Chem. Soc.* **1963**, *85*, 391-394.
54)Taillandier, E.; Liquier, J. *Methods Enz.* **1992**, *211*, 307-335.
55)Taillandier, E.; Liquier, J.; Ghomi, M. *J. Mol. Struct.* **1989**, *214*, 185-211.
56)Liquier, J.; Coffinier, P.; Firon, M.; Taillandier, E. *J. Biomol. Struct. Dyn.* **1991**, *9*, 437-445.

# CHAPTER 3

# Colloidal labeling for DNA hybridization detection on gold substrates

# *3.1 Introduction to nanoparticles*

## 3.1.1 Optical and redox properties of nanoparticles

Metal nanoparticles have been investigated widely since the studies of colloidal gold by Faraday in the 1800s[1]. The size, shape and composition of the nanoparticles influence their properties [2] . Properties of nanoparticles are different from their bulk counterparts due to the reduced dimensionality and modification of functional properties. The conduction band present in the bulk is absent in nanometals in the case of metallic nanoparticles but there are discrete states at the band edge of the particles. Also depending on the size, shape and the interatomic distance, the free electrons oscillate at a particular frequency. In case of gold colloids, these electrons at the surface of the colloid can absorb electromagnetic radiation that matches with the frequency of oscillation of the conduction electron and exhibit a strong absorbance band called the Surface plasmon band in the visible spectrum. The plasmon frequency band is present around 520 nm for gold nanoparticles but for very small particles of size 2 nm, it disappears. Also for bigger particles the plasmon band shifts to a higher wavelength. This is the test for aggregation of gold colloid as the color of the gold nanopartcles turns from pink to blue. As clusters of bigger particles are formed the plasmon band shifts.

Metal nanoparticles also exhibit high extinction coefficients. For instance, a 10 nm gold colloid has a extinction coefficient of the order of $\sim 10^8\ M^{-1}\ cm^{-1}$. Transition metals like Co show a magnetic behaviour that is size dependent. Metal oxide nanoparticles such as titanium dioxide exhibit increased redox properties while gold nanoclusters exhibit an increase in catalytic activity that cannot be duplicated by bulk gold particles.

Semiconductor nanoparticles like CdSe or CdS called "quantum dots" can also be functionalized with streptavidin or carboxylates for biological applications. Their fluorescence quantum yields are higher compared to conventional fluorescent dyes reducing the limit of detection.

The properties of nanoparticles make them interesting tools in biology, optics and for labeling chemistry. Gold colloids have been extensively used for DNA hybridization, [3] [4, 5] [6] protein assays [7], immunoassays [8, 9][10] [11], cell targeting and delivery [12]. One of the important areas of application of the properties related to aggregation of metallic nanoparticles is for the analyte detection. The plasmon band of monomer gold nanoparticles is near 520 nm and a solution has a dark pink color. Upon aggregation due to addition of salt the solution turns to blue or purple. The origin of this effect is the reduction in the Debye length $1/\kappa$ that permits closer approach of the nanoparticles. According to Derjaguin-Landau-Verwey-Overbeek (DLVO) theory the reduced electrostatic repulsion tips the balance of the potential energy in favor of the attractive van der Waal's term resulting flocculation and aggregation. A blue color is also observed when colloidal gold aggregates in response to the addition of an analyte in the case of antibody-labeled immunogold. This phenomenon is the used for many common assays including the home pregnancy test, in which a sufficient concentration of human chorionic gonadotropin (hCG) present in the urine sample will produce flocculation/aggregation of colloidal gold labeled with hCG-antibody. The color change arises due to the creation of a gold structure of larger dimension and the frequency of the plasmon band depends on the dimensions of the cluster.

### 3.1.2 Stability of colloids

Nanoparticles are colloids dispersed in fluid suspensions. The stability of the the colloids is determined by the balance of three forces – van der Waals attraction, electrostatic repulsion and the randomizing thermal energy. Mutual dipole interactions (Van der Waals attraction) due to the polarizibility of the colloid cause the colloids to flocculate and aggregate over time. Derjaguin, Landau, Verwey and Overbeek proposed (DLVO theory) that the electrostatic charge on the surface of colloids will cause repulsive interaction and prevent aggregation. This repulsive force keeps the colloids stable [13]. According to DLVO theory, the van der Waals attraction due to the polarizibilty of the colloids is compenasated by the electrostatic repulsion due to the electrical double layer between the two colloids. The electrostatic repulsion varies as $e^{-\kappa r}$ and van der waals attraction varies as $r^{-2}$. The electrical double layer prevents the colloids from coming near the vicinity of each other where the attractive forces can draw them together. But in some conditions the electrical double layer reduces in thickness causing the van der Waals attraction to be the predominant force causing aggregation of colloids. The conditions for flocculation is given by the Debye equation

$$x=(\varepsilon T/8\pi n e^2 \nu^2)^{1/2} \qquad 3.1$$

where $\varepsilon$ is the dielectric constant of the solution , T is the temperature, n is the concentration of the salt present and $\nu$ is the valence of the salt. According to the equation 3.1 a high concentration of salt of high valence will cause the colloids to flocculate by reducing the Debye length.

Metal colloids are normally stabilized with a charged polyanionic molecule or a biomolecule which offers steric stability to the colloid. Citrate is the most common stabilizer that is used to stabilize gold colloid with a weakly binding layer of charged ligands. Citrates can be easily replaced by more stable chemical entities like mercaptoalkanoic acids, thiols and mercaptoalkylamines. [14-16] [17]

Other charged molecules used for stabilizing gold colloid by electrostatic interaction are Bis(*p*-sulfonatophenyl)- phenylphosphine (BSPP) and mercaptoundeconoic acid (MUA). Gold colloids labeled with oligonucleotides are used in the DNA-array based detection systems [18]

## *3.2 Adsorption of Ru(II) and Os(II) Polypyridyl Complexes on Gold and Silver Nanoparticles*

To understand the properties of gold nanoparticles better a study on detection of adsorption of Ru(II) and Os(II) Polypyridyl Complexes on Gold and Silver Nanoparticles was carried out by Single Photon Counting Emission Measurements. The present study describes a new application of Ruthenium(II) tris bipyridine ($Ru(bpy)_3^{2+}$) and Osmium(II) tris bipyridine ($Os(bpy)_3^{2+}$) as phosphorescent labels for the quantification of surface binding of molecules to gold and silver nanoparticles. The fraction of $Ru(bpy)_3^{2+}$ and $Os(bpy)_3^{2+}$ that is in solution can be distinguished from the surface bound fraction by the relative lifetimes and integrated emission yields as determined by time-correlated single photon counting (TCSPC) spectroscopy. The emission on Au and Ag nanoparticles is quenched by a process that may involve both energy and electron transfer. Complementary steady state measurements were carried out in order to confirm surface attachment of the phosphorescent label molecules. The emission followed Stern-Volmer behavior when 10 nm Au and 20 nm Ag nanoparticles were added to solutions of

$Ru(bpy)_3^{2+}$ and $Os(bpy)_3^{2+}$. The results demonstrate a useful probe for the measurement of surface binding of labeled peptides proteins and other macromolecules on metallic nanoparticles.

### 3.2.1 Introduction

The direct observation of molecular properties on nanoparticle surfaces has wide application as a means of probing the electronic nature of the surface and the electrostatic environment of the colloid as well. These colloidal constructs may serve as electrochemical probes as well as optical probes[19]. For example, the study of surface enhanced phenomena with Raman, IR and other non-linear spectroscopies relies on knowledge of the molecular structure and a model for their geometric relationship to the surfaces of nanoparticles. Investigation of the electrostatic environment suggests that the stabilizer has a profound effect on the electrostatic field at the surface of the nanoparticle. These effects are important since they relate to interparticle repulsions that stabilize the colloidal suspensions. Moreover, the preparation of stable nanoparticle constructs that use DNA or proteins as recognition elements require an understanding of the effect of electrostatics on the particle surface. The nature of the adsorption process and the effect of adsorption on molecular properties is important both for the optical and electronic properties of molecules on surfaces.

Steady state emission studies of molecules on surfaces have indicated that quenching occurs when molecules are in the vicinity of a metal [20-22] Electron transfer between Ru(II) and Os(II) polypyridyl complexes linked to polymers have been widely studied [23-25] Recently, Murray and coworkers reported steady-state emission quenching of $Ru(bpy)_3^{2+}$ on Au nanoparticles with radii smaller than required in order for the colloids to exhibit plasmon bands [21] Herein, we study the quenching of emission of $Ru(bpy)_3^{2+}$ and $Os(bpy)_3^{2+}$ on Au and Ag surfaces. The emission quenching is observed both in steady state and using time-correlated single-photon counting (TCSPC) emission measurements. Compared to steady state emission measurements, TCSPC has the advantage that one can distinguish a component that contributes only a few percent to the total emission signal using the lifetime of that component. The goal of these studies is to establish a direct measurement of the number of particles bound to the surface of the nanoparticle as well as the extent of the quenching. These studies demonstrate the general utility of time-resolved emission spectroscopy for the detection of molecules on nanoparticle surfaces.

## 3.2.2 Methods and Material

### 3.2.2.1 Materials

10 nm trisodium citrate stabilized gold colloids and 20 nm trisodium citrate stabilized silver colloids were purchased from Ted Pella. Inc. More stable preparations of gold nanoparticles were obtained by replacement of citrate by $HS(CH_2)_7COOH$ (mercaptooctanoic acid, MO). Concentration of the gold sol was determined by the absorption at $\omega_{\text{Fröhlich}}$ = 19 200 $cm^{-1}$ (521 nm) for 10 nm Au. Ruthenium(II) tris bipyridine ($Ru(bpy)_3^{2+}$) was purchased from Alfa Aesar. Osmium(II) tris bipyridine ($Os(bpy)_3^{2+}$) was obtained as a gift from T. J. Meyer.

### 3.2.2.2. Steady-State Methods

All absorption measurements were made on a Hewlett Packard 8453 Chemstation Photo Diode Array Spectrophotometer with attached Chemstation software using 0.5 cm cuvettes. Steady state emission spectra were recorded on a PTI Quantamaster Luminescence Spectrometer (MD-5020) or an ISS K2 phase fluorometer. Samples were sparged with Argon prior to measurements.

### 3.2.2.3. Time-Resolved Emission methods

The apparatus consists of a commercially available Argon ion laser whose continuous output is used to pump a mode-locked Ti:Sapphire laser. The Ti:Sapphire laser output is frequency doubled to 423 nm using a BBO crystal to produce ~1 ps pulses with a pulse energy of ~.26 nJ/pulse. This pulse train is pulse picked and the repetition rate selected to be roughly 5 times the natural lifetime of the sample. Luminescence lifetime data was collected using the time-correlated single photon counting technique published earlier [23]. Samples were sparged with argon for ~ 45 minutes prior to use.

### 3.2.3 Results

### 3.2.3 1 Steady-State spectra

**System I: $Ru(bpy)_3^{2+}$ adsorbed onto 10 nm MO-stabilized Au colloids.**

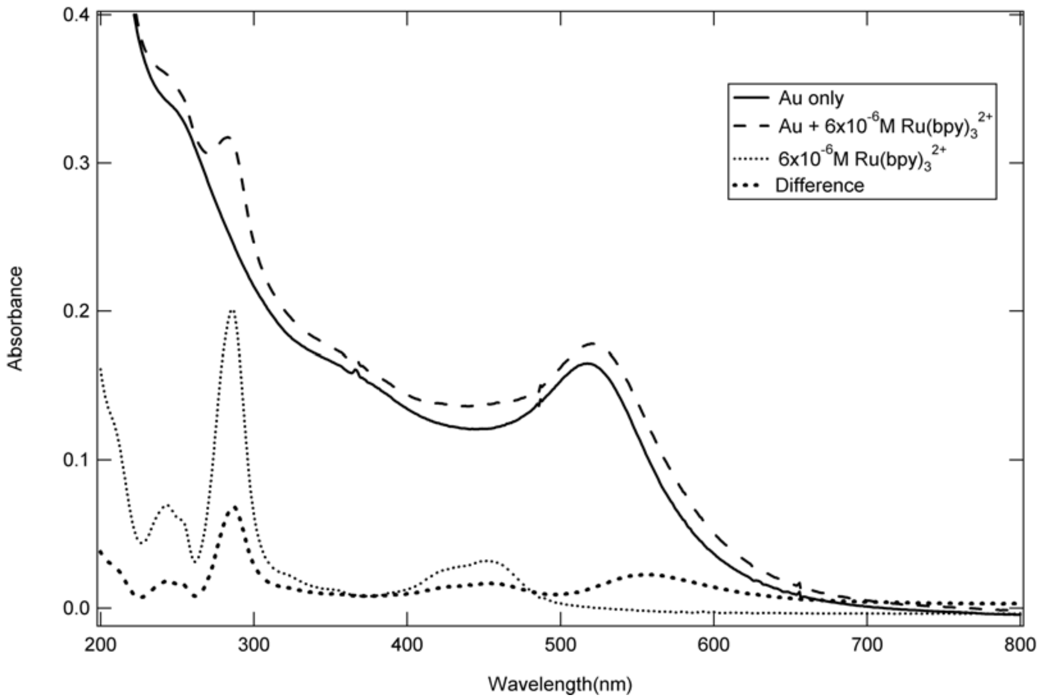


**Figure 3.1. UV-VIS absorption spectra of 6x10-6M Ru(bpy)32+ adsorbed onto 10 nm mercaptooctanoate (MO) stabilized Au colloids (3.1x10-9 M), which corresponds to a ratio of Ru(bpy)32+/Au ~2000. The mixture was allowed to equilibrate for ~1 h before spectra were taken. Monomer spectra of the Au colloids and the Ru(bpy)32+ complex at equivalent concentrations are also included. The difference spectrum was obtained by subtracting the monomer spectrum of Au colloids from the spectrum of the mixture.**

Figure 3.1 shows the ground-state absorption spectrum of $Ru(bpy)_3^{2+}$ adsorbed onto 10 nm mercaptooctanoate (MO) stabilized Au colloids. The spectrum shows an intense band centered at 521nm, which corresponds to the Fröhlich frequency of 10 nm Au, as well as an additional band centered around 286 nm from the $Ru(bpy)_3^{2+}$-complex. From comparison with the monomer spectra, it is also possible to see the contribution from the metal-to-ligand charge transfer (MLCT) $Ru(bpy)_3^{2+}$-band centered at 450 nm. Upon adsorption, the shape and width of the Au plasmon band remained relatively unchanged, which confirms the presence of single colloids, and the peak of the gold plasmon band was shifted >5 nm, indicating a slight change in the dielectric function of the Au surface from the adsorption of $Ru(bpy)_3^{2+}$. Thus we are confident that our system still consists of monomer Au colloids with electrostatically adsorbed $Ru(bpy)_3^{2+}$. Interestingly, the difference spectrum suggests that the $Ru(bpy)_3^{2+}$ bands are reduced in intensity.

The emission spectra for this system (see Supporting Information) clearly shows the high-energy band around 590 nm from Ru*-Ru transitions. The relative intensities of $Ru(bpy)_3^{2+}$ and Ru-Au emission shows that the presence of Au leads to extensive quenching of the $Ru(bpy)_3^{2+}$ excited state. Also, the contribution from the Au-colloids is negligible. There is clearly significant free (unbound) $Ru(bpy)_3^{2+}$ and as discussed below, most of the emission observed is likely to arise from the unbound fraction.

**System II: $Ru(bpy)_3^{2+}$ adsorbed onto 10 nm citrate-stabilized Au colloids.**

The system depicted in Figure 3.2 shows essentially the same spectral features as the MO-stabilized system shown in Figure 3.1, taking into account that the $Ru(bpy)_3^{2+}$ concentration for the citrate-stabilized system is decreased by a factor of ~7 to adjust for the relative stabilizing properties of the passivating ligand (citrate versus MO). From the plasmon band of the Au colloids, the same conclusions can be drawn as for the MO-stabilized system; the $Ru(bpy)_3^{2+}$ is indeed adsorbed onto the colloids (although the shift is smaller), and the system is not aggregating.

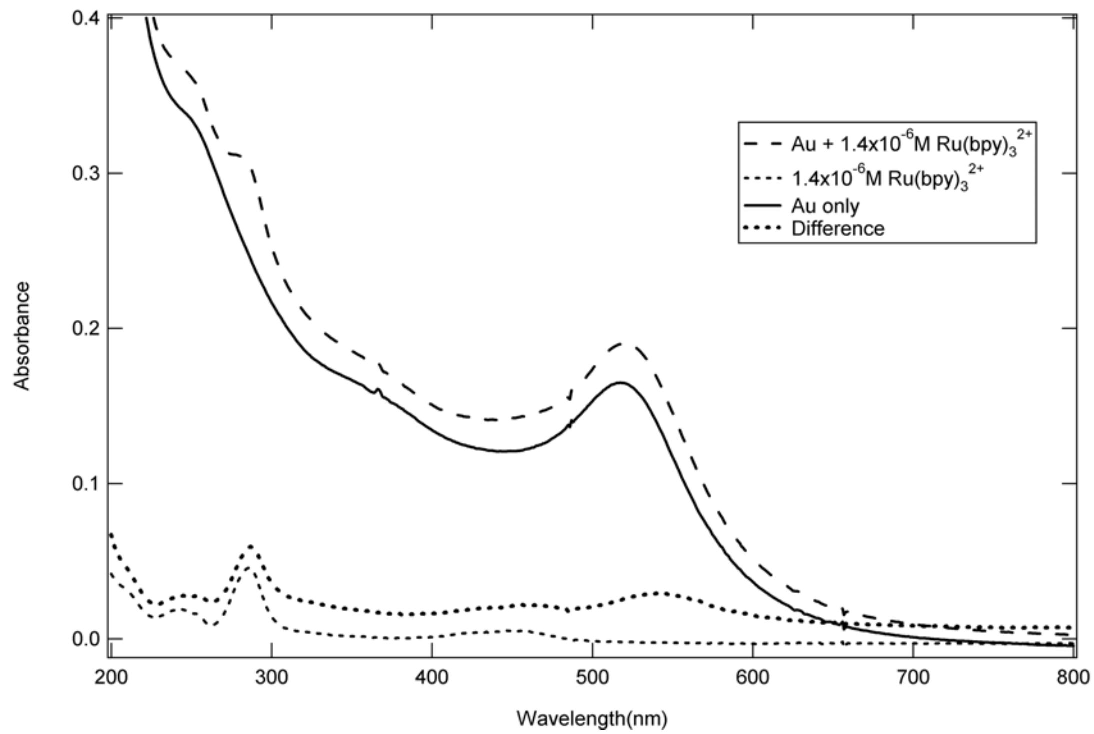


**Figure 3.2. UV-VIS absorption spectra of 1.4x10$^{-6}$ M $Ru(bpy)_3^{2+}$ adsorbed onto 10 nm citrate stabilized Au colloids (4.7x10$^{-9}$ M), which corresponds to a ratio of $Ru(bpy)_3^{2+}$/Au ~300. The mixture was allowed to equilibrate for ~1 h before spectra were taken. Monomer spectra of the Au colloids and the $Ru(bpy)_3^{2+}$ complex at equivalent concentrations are also included. The difference spectrum was obtained by subtracting the monomer spectrum of Au colloids from the spectrum of the mixture.**

However, the difference spectrum shows that the citrate-stabilized system deviates from its MO-stabilized counterpart, in that the bands of the $Ru(bpy)_3^{2+}$ are not bleached as a result of the adsorption. The MLCT band of $Ru(bpy)_3^{2+}$ is observed at a higher frequency than the plasmon frequency of Au. The emission spectra for this system (see Supporting Information) show the same trend as for the MO-stabilized system. The relative intensities of $Ru(bpy)_3^{2+}$ and Ru-Au emission indicate that the presence of Au leads to extensive quenching of the $Ru(bpy)_3^{2+}$ excited state.

**System III: $Ru(bpy)_3^{2+}$ adsorbed onto 20 nm citrate-stabilized Ag colloids.**

Figure 3.3 shows the ground-state absorption spectrum of $Ru(bpy)_3^{2+}$ adsorbed onto 20 nm citrate stabilized Ag colloids.

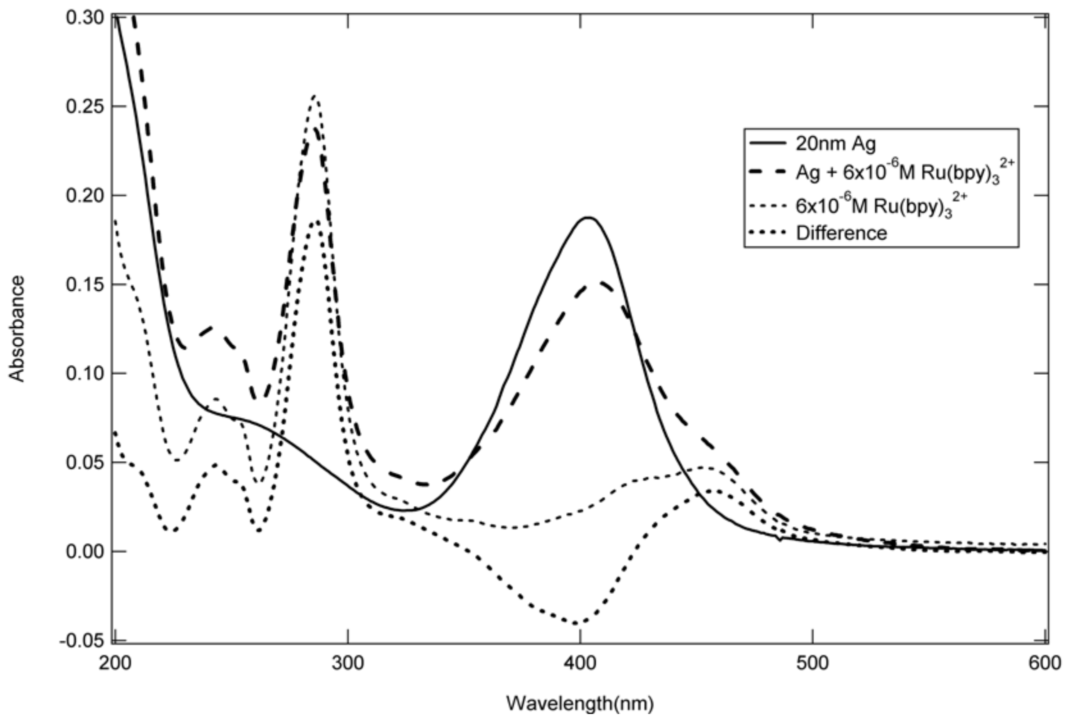


**Figure 3.3. UV-VIS absorption spectra of 6x10$^{-6}$ M Ru(bpy)$_3^{2+}$ adsorbed onto 20 nm citrate stabilized Ag colloids. The mixture was allowed to equilibrate for ~2 h before spectra were taken. Monomer spectra of the Ag colloids and the Ru(bpy)$_3^{2+}$ complex at equivalent concentrations are also included. The difference spectrum was obtained by subtracting the monomer spectrum of Ag colloids from the spectrum of the mixture.**

The spectrum shows an intense band centered at 400 nm, which corresponds to the Fröhlich frequency of 20 nm Ag, as well as an additional band centered around 286 nm from the Ru(bpy)$_3^{2+}$-complex. From comparison with the monomer spectra, it is also possible to see the contribution from the metal-to-ligand charge transfer (MLCT) Ru(bpy)$_3^{2+}$-band centered at 450 nm. Upon adsorption, the shape and width of the Ag plasmon band remained relatively unchanged and confirms the presence of single colloids. The peak was shifted ~5 nm, indicating a slight change in the dielectric function of the Ag surface from the adsorption of Ru(bpy)$_3^{2+}$. As can be seen from the difference spectrum, altering the colloidal substrate from Au to Ag nanoparticles resulted in a substantial bleaching of the Ru(bpy)$_3^{2+}$ 450 nm-band, which is consistent with previous results for dye molecules on citrate-coated nanoparticles [26] (see below). The colloidal stability of the Ag nanoparticles was much higher than its Au counterpart. The emission data (see Supporting information) demonstrates that the interaction between adsorbate and colloidal substrate in the Ag-colloid system is comparable to the Au-colloid equivalents. Furthermore, substantial unbound $Ru(bpy)_3^{2+}$ molecules are present.

**System IV: $Os(bpy)_3^{2+}$ adsorbed onto 20 nm citrate-stabilized Ag colloids.**

Figure 3.4 shows the ground-state absorption spectrum of $Os(bpy)_3^{2+}$ adsorbed onto 20 nm citrate stabilized Ag colloids. The spectrum shows an intense band centered at 400 nm, which corresponds to the Fröhlich frequency of 20 nm Ag, as well as bands from the $Os(bpy)_3^{2+}$-complex, centered around 286 nm and 450 nm, and an additional, weaker band that extends out to ~700 nm.

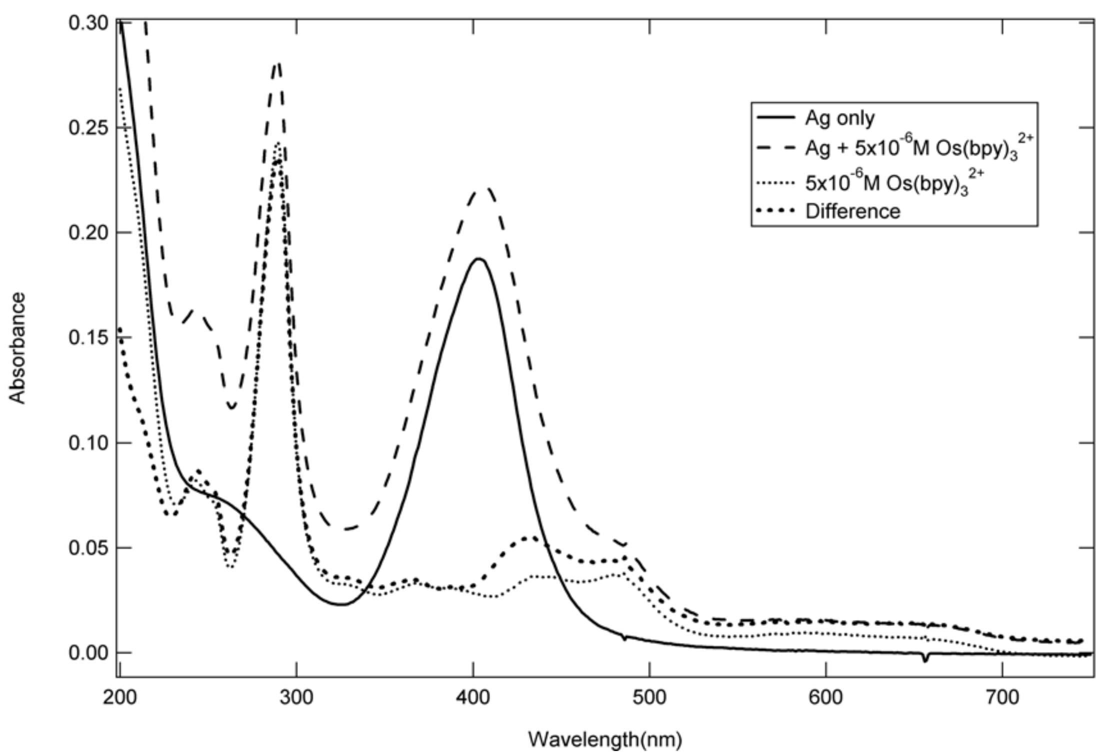


**Figure 3.4. UV-VIS absorption spectra of $5x10^{-6}$ M $Os(bpy)_3^{2+}$ adsorbed onto 20 nm citrate stabilized Ag colloids . The mixture was allowed to equilibrate for ~1 h before spectra were taken. Monomer spectra of the Ag colloids and the $Os(bpy)_3^{2+}$ complex at equivalent concentrations**

**are also included. The difference spectrum was obtained by subtracting the monomer spectrum of Ag colloids from the spectrum of the mixture.**

Upon adsorption, the shape and width of the Ag plasmon band remained relatively unchanged, which confirms the presence of single colloids, and the peak was shifted slightly, indicating a slight change in the dielectric function of the Ag surface from the adsorption of $Os(bpy)_3^{2+}$. Interestingly, the emission data (see supplementary information) suggest that the presence of Ag colloids quenches the intensity of the Os-band centered around 720 nm much less than for the corresponding Ru-system.

### 3.2.3.2 Time-Resolved Data

Time-resolved data was obtained for both the adsorbate systems and for the colloidal substrate-adsorbate constructs. Table 3.1 summarizes the essential characteristics of each system, including the measured lifetimes. For all general functions used to fit the time-resolved data, see Supporting Information.

**System I: $Ru(bpy)_3^{2+}$ adsorbed onto 10 nm MO-stabilized Au colloids.**

Figure 3.5 shows the time-resolved data for 6μM $Ru(bpy)_3^{2+}$ in aqueous solution. As expected, $Ru(bpy)_3^{2+}$ decays with single exponential kinetics and a lifetime of 623 ns. Time-resolved emission data for the colloidal substrate-adsorbate constructs, as shown in Figure 3.5, demonstrate a clear deviation from this single-exponential behavior. Figure 3.5 depicts System I with a biexponential decay. The biphasic model used five parameter function ($A_1\exp\{-t/\tau_1\} + A_2\exp\{-t/\tau_2\} + B$), resulting in a correlation coefficient of ~0.75. The fit parameters were $A_1 = 0.68$ with $\tau_1 = 1.2$ ns and $A_2 = 0.31$ , with $\tau_2 = 598$ ns and $B = 0.01$.

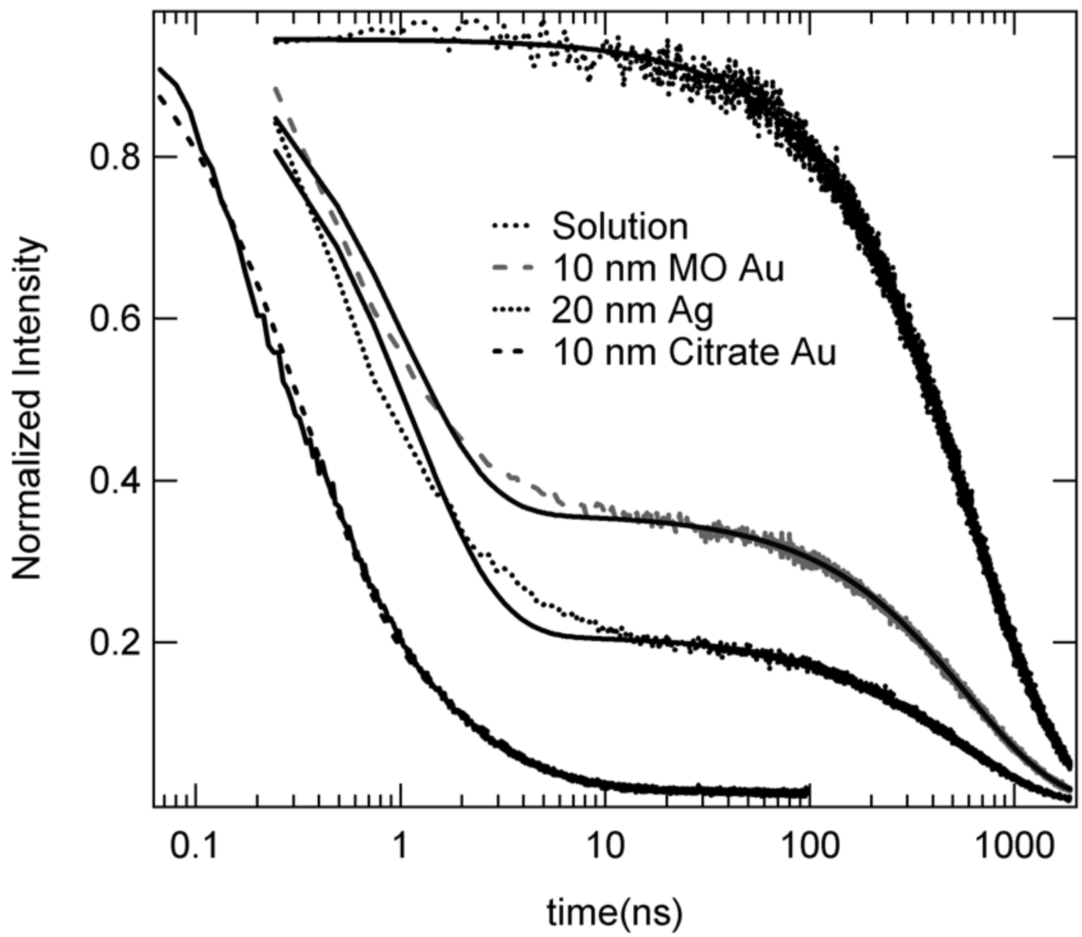


**Figure 3.5. Time-Resolved emission from $Ru(bpy)_3^{2+}$ in solution and adsorbed onto various colloids. The colloids include 10 nm mercaptooctanoate (MO) stabilized Au colloids ($3.1x10^{-9}$ M), 20 nm citrate stabilized Ag colloids and 10 nm citrate stabilized Au colloids ($4.7x10^{-9}$ M). Given a solution concentration of $6x10^{-6}$ M $Ru(bpy)_3^{2+}$/Au for the MO stabilized colloids the ratio of $Ru(bpy)_3^{2+}$:Au is ~2000. Lower concentrations had to be used for the citrate stabilized colloids in order to avoid aggregation. Given a solution concentration of $1.4x10^{-6}$ M $Ru(bpy)_3^{2+}$ in solution the ratio of $Ru(bpy)_3^{2+}$:Au was ~300. The excitation wavelength was 423 nm and emission was detected at 640 nm. Each kinetic trace was normalized by setting the maximum intensity equal to 1. The experimental fits shown in the Figure all used a biexponential function. Experimental data are shown as a dashed line, and the predicted fit is shown as a solid line.**

To improve the fit, a triexponential, seven parameter function ($A_1\exp\{-t/\tau_1\}$ + $A_2\exp\{-t/\tau_2\}$ + $A_3\exp\{-t/\tau_3\}$ + B) was imposed upon the system, which resulted in a significant increase in the correlation coefficient from ~0.75 to ~0.93, thus suggesting that the emission at 630(or 620) nm in System I is comprised of three components.

**System II: $Ru(bpy)_3^{2+}$ adsorbed onto 10 nm citrate-stabilized Au colloids.**

The adsorption of $Ru(bpy)_3^{2+}$ to 10 nm Au colloids with a trisodium citrate passivating layer required a concentration roughly 1/7 lower than for System I. If the concentration is increased beyond that value, flocculation occurs. The data depicted in Figure 3.5 show a marked decrease in the phosphorescence lifetime for $Ru(bpy)_3^{2+}$ adsorbed onto the citrate-coated colloid. The data were fit to single exponential, biexponential and triexponential functions. A clear deviation from single-exponential decay was evident, but there was no significant improvement (< 0.01) of the correlation coefficient upon adding a third exponential. The fit parameters for a biexponential model were $A_1 = 0.8$ with $\tau_1 = 0.32$ ns and $A_2 = 0.2$ , with $\tau_2 = 2.6$ ns. As can be seen, none of these observed lifetimes were characteristic of unassociated $Ru(bpy)_3^{2+}$ (see Table 3.1). These results indicate that essentially all of the $Ru(bpy)_3^{2+}$ is adsorbed to, or at least associated with, the nanoparticle.

| **Adsorbate** | **Substrate** | **Lifetimes τ (ns)** | **Relative population** | **Lifetime designation[a]** |
|---|---|---|---|---|
| $Ru(bpy)_3^{2+}$ | - | 623.0 | 1.00 | Solution |
| | | 0.8 | 0.60 | Surface |
| $Ru(bpy)_3^{2+}$ | 10 nm Au[b] | 4.5 | 0.12 | Surface |
| | | 605.3 | 0.31 | Solution |
| $Ru(bpy)_3^{2+}$ | 10 nm Au[c] | 0.3 | 0.80 | Surface |
| | | 2.6 | 0.20 | Surface |
| $Ru(bpy)_3^{2+}$ | 20 nm Ag[c] | 1.1 | 0.75 | Surface |
| | | 533.0 | 0.21 | Solution |
| $Os(bpy)_3^{2+}$ | - | 23.0 | 1.00 | Solution |
| $Os(bpy)_3^{2+}$ | 20 nm Ag[c] | 0.4 | 0.54 | Surface |
| | | 22.0 | 0.42 | Solution |

Table 3.1: Lifetimes and Calculated Populations for Mixed Polypyridyl-Colloid Systems

**System III: $Ru(bpy)_3^{2+}$ adsorbed onto 20 nm citrate-stabilized Ag colloids.**

We collected a transient of 5 μM $Ru(bpy)_3^{2+}$ adsorbed to 20 nm Ag colloids, as shown in Figure 3.5 to investigate the effect of changing the nature of the metallic substrate, and to verify the assumption that the adsorbate concentration does not affect the number of species contributing to the emission. The data depicted in Figure 3.5 were treated similarly to the previous data, resulting in a best fit for a biexponential decay, indicating one surface-confined species and one unattached species. The fit parameters were $A_1$ = 0.75 with $\tau_1$ = 1.1 ns and $A_2$ = 0.21 , with $\tau_2$ = 533 ns. Addition of a third exponential resulted in little or no improvement of the correlation coefficient.

**System IV: $Os(bpy)_3^{2+}$ adsorbed onto 20 nm citrate-stabilized Ag colloids.**

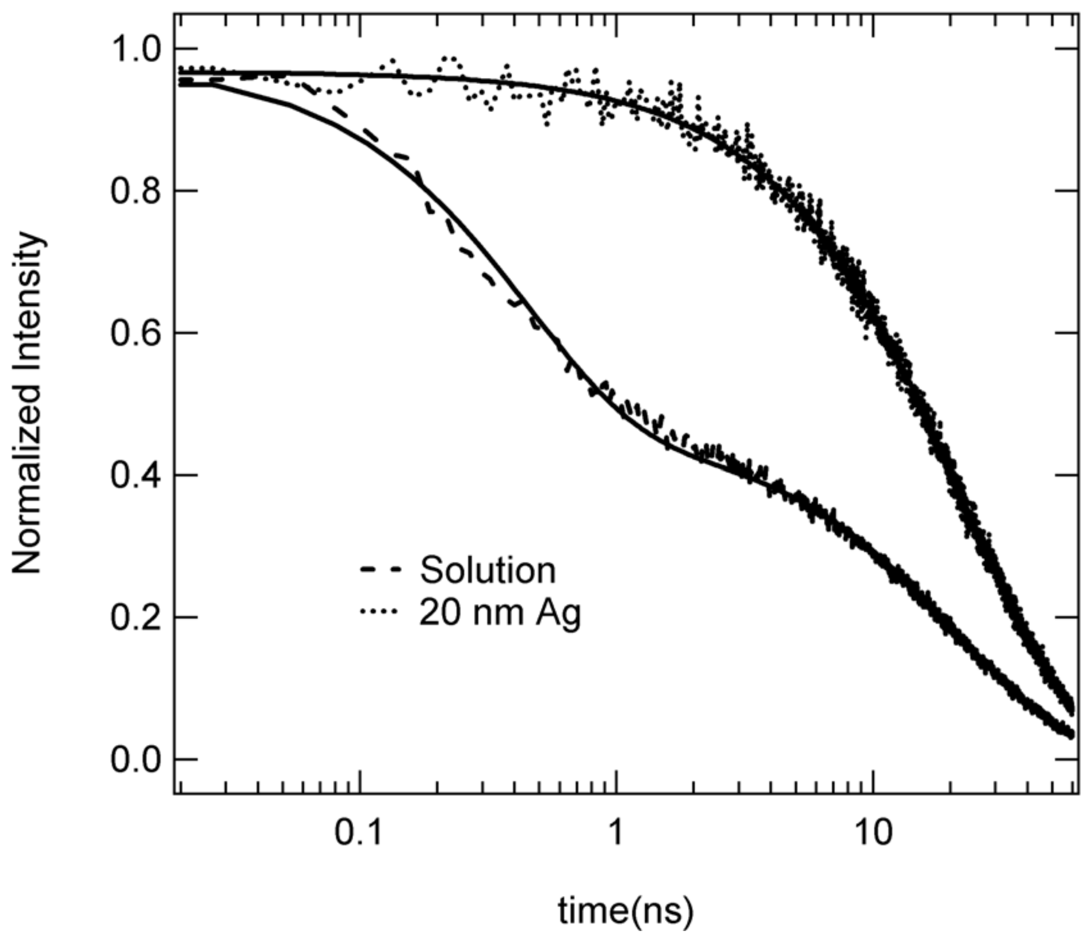


**Figure 3.6. Time-Resolved emission data, detected at 780 nm, of $5x10^{-6}$ M $Os(bpy)_3^{2+}$ in aqueous solution and on 20 nm citrate stabilized Ag colloids is shown. The excitation wavelength for these systems was also 423 nm. The experimental data for $Os(bpy)_3^{2+}$ in aqueous solution were fitted to a single-exponential function, and the data for the mixed $Os(bpy)_3^{2+}$ colloid system were fit to a biexponential function. Each kinetic trace was normalized by setting the maximum intensity equal to 1. Experimental data are shown as a dashed line, and the predicted fit is shown as a solid line.**

Figure 3.6 shows time-resolved data for 5μM $Os(bpy)_3^{2+}$ in aqueous solution. As for $Ru(bpy)_3^{2+}$, $Os(bpy)_3^{2+}$ decays with single-exponential kinetics with a lifetime of 23 ns. The mixed system was fit to a multiexponential decay and, as for System III, was best fitted to a biexponential function. The fit parameters were $A_1 = 0.54$ with $\tau_1 = 0.40$ ns and $A_2 = 0.42$ , with $\tau_2 = 22$ ns. . Thus, it may be suggested that changing the central atom of the polypyridyl complex does not change the adsorption characteristics.

### 3.2.4 Discussion

A comparison can be made with earlier work on aromatic dye molecule adsorbates [20] [26-28] by substituting Au colloids for Ag colloids. The plasmon band of an Ag colloid is blue-shifted relative to the MLCT band of $Ru(bpy)_3^{2+}$. According to an electromagnetic mechanism, the surface selection rule predicts that for an adsorbate-substrate interaction, any component of the transition dipole parallel to the surface does not contribute to the absorption[29] Assuming that this selection rule is valid for $Ru(bpy)_3^{2+}$ and $Os(bpy)_3^{2+}$ adsorbed to Au and Ag colloids, then bleaching should be observed in the absorption spectrum. If the excitation were isotropic (i.e. no symmetry breaking) then one would expect that roughly 2/3 of the intensity should be reduced. A simple interpretation states that the x and y transition moments are in the plane of the nanoparticle surface while the z-component transition moment is perpendicular and can be interrogated by the perpendicular component of p-polarized light. However, solution Stark effect and other measurements strongly suggest that symmetry breaking results in an oriented MLCT transition that favors one bipyridine over the others. In this case the transition moment is more nearly parallel to the surface and the effect of adsorption should be quite different than that observed for aromatic dye molecules. There is some reduction in intensity for $Ru(bpy)_3^{2+}$ adducts on Au and Ag, but not for $Os(bpy)_3^{2+}$ adducts on Ag. The fact that there is substantial absorbance for surface adsorbed $Ru(bpy)_3^{2+}$ suggests that a probe of the emission lifetime of the surface-bound fraction will provide a quantitative means to estimate the surface-bound fraction.

For an idealized adsorption process between the adsorbate and the colloidal substrate, where the equilibrium constant for the adsorption process is $\sim\infty$, and where adsorption does not progress beyond monolayer coverage, the Ru emission would be expected to follow a single exponential decay, with a shorter lifetime than that of $Ru(bpy)_3^{2+}$ in free solution. This would indicate that all of the $Ru(bpy)_3^{2+}$ is bound to the colloidal surface.

A realistic model is comprised of a biexponential decay; a highly populated fast component representing the fraction of surface-bound $Ru(bpy)_3^{2+}$, and a less populated, slower component representing the fraction of $Ru(bpy)_3^{2+}$ still in solution.

The biexponential model takes into account the role of the equilibrium constant K for the adsorption process. The most applicable model for an adsorption isotherm for this process is the Langmuir adsorption isotherm (eq 3.2)

$$KC' = \frac{\theta}{1-\theta} \tag{3.2}$$

where $\theta$ is the fractional surface coverage, K is the equilibrium constant for surface binding and C' is the bulk concentration of adsorbate. To provide a more realistic model of this system, the Frumkin isotherm (eq 3.3) describes adsorption where there are interactive forces between adsorbates.

$$KC' = \left(\frac{\theta}{1-\theta}\right)e^{f\theta} \qquad (3.3)$$

The Frumkin parameter f takes into account adsorbate repulsion (or attraction) by assuming that the apparent free energy of binding to the substrate changes linearly with particle coverage. Equation 3.3 describes systems with repulsive forces between adsorbates when $f > 0$, and attractive forces when $f < 0$. When there are no long-range interactions between adsorbates, equation 3.3 simplifies to equation 3.2.

Not all of the data of adsorbed nanoparticles can be fit to a biexponential model that is easily converted into a Langmuir or Frumkin analysis. The comparison of different passivating layers provides a means to examine the effects of surface adsorption in competition with different chemical groups. For example, citrate appears to be easily displaced from Au and Ag colloids compared to other passivating layers such as phosphines and alkane-thiols. An alternative passivating layer is mercaptooctanoate (MO), which is introduced to the colloids by means of an exchange process. The initial passivating layer (trisodium citrate) is displaced by the MO through chemisorption of the thiol. Thus it is entirely possible that the new passivating layer has imperfections in which the $Ru(bpy)_3^{2+}$ can fit, or that the fractional surface coverage of MO is less than unity. Considering this, the triexponential function may provide a good and realistic fit, and can physically be interpreted as the three components: 1)free $Ru(bpy)_3^{2+}$ (slowest component), 2)$Ru(bpy)_3^{2+}$ electrostatically adsorbed to the passivating layer on the colloidal surface, and 3)$Ru(bpy)_3^{2+}$ "wedged in" between the surface of the passivating layer and the Au surface (fastest component).

The phosphorescence quantum yield is given by (eq 3.4):

$$\Phi_{phosphorescence} = \frac{k_{phosphorescence}}{k_q + k_{ISC} + k_{phosphorescence}} \tag{3.4}$$

Equation 3.4 indicates that there is an intrinsic emission yield $\Phi_{phosphorescence} = k_{phosphorescence}/(k_{ISC} + k_{phosphorescence})$, where $k_{ISC}$ is the intersystem crossing rate from the MLCT state back to the ground state. The observed phosphoorescence yield for $Ru(bpy)_3^{2+}$ in deoxygenated solution is 0.042+/- 0.002 (at 25$^o$C) [30]. Given that the observed phosphorescence rate constant in solution is $k_{obs} = k_{ISC} + k_{phosphorescence}$ we have that the intrinsic phosphorescence rate constant is $k_{phosphorescence} = \Phi_{phosphorescence}k_{obs} = 7.24x10^4\ s^{-1}$. The quenching rate constant is significantly greater than the intersystem crossing rate constant. The physical origins of the quenching process due to surface adsorption will be discussed below.

The quenching process could arise from energy transfer, electron transfer or an enhanced intersystem crossing rate constant. All of these quenching processes can be considered within the approximations of first order time-dependent quantum mechanics. For energy transfer or electron transfer the rate constant is:

$$k_{ET} = \frac{\hbar^2}{2\pi}|V^2|FC \tag{3.5}$$

Where V is the electronic coupling and FC is the Franck-Condon factor. V is an electronic factor that can be expressed in terms of the electronic wave functions.

$$V = \left\langle \Psi_{MLCT} | H | \Psi_{Ru^{3+}Au^{-}} \right\rangle \qquad (3.6)$$

where Ψ represents the electronic wave function. The subscripts indicate that photoexcited state and one of the possible charge separated states, respectively. The FC factor is given by:

$$FC = \sum_{v,v'=0}^{\infty} \left\langle \chi_v^{MLCT} | \chi_{v'}^{Ru^{3+}Au^{-}} \right\rangle^2 \rho \qquad (3.7)$$

where $\chi_v$ and $\chi_{v'}$ are the nuclear wave functions for the reactant and product states, respectively. The term ρ represents the density of states. The same formalism applies to ISC, however, in that case the Hamiltonian corresponds to the spin orbit term. We regard an enhanced $k_{ISC}$ rate constant as the least plausible mechanism [19]. Although Au may provide some perturbation to the spin orbit term the central ruthenium in the $Ru(bpy)_3^{2+}$ adduct is likely to dominate. The density of phonon states near a metal is not the same as solution, but there is no evidence to support a large increase in the density of relevant phonon states.

It is often thought that energy transfer is responsible for quenching of fluorescence or phosphorescence due to surface states of a metal [6, 19, 21, 31-36]. For a dipole-dipole mechanism, energy transfer requires that the absorption spectrum of the acceptor have significant overlap with the emission spectrum of the donor [33, 34, 37]. For an optical coupling the plasmon band of the nanoparticle is likely to play an important role in the coupling. The plasmon band of Au ($\omega_{\text{Fröhlich}}$ ~ 19,200 $cm^{-1}$) is approximately at the same frequency as the emission from $Ru(bpy)_3^{2+}$. As observed in Figure 3.5 the rate constant for emission of $Ru(bpy)_3^{2+}$ adsorbed onto both Au and Ag particles are quite similar. Since Ag has a plasmon band at much higher energy ($\omega_{\text{Fröhlich}}$

~ 26,300 $cm^{-1}$) it is not likely that a dipole-dipole mechanism is operative in the case of Ag even if it were in the case of Au nanoparticles.

There is also an orientational requirement for energy transfer [34]. The probability is modulated by the angle between the transition moment of the donor and acceptor. In the case of a molecule on gold, this means that the molecular transition moment must be parallel to thesurface in order to couple into the plasmon band. As discussed above for the observed absorption spectrum, symmetry breaking likely gives rise to a MLCT transition that is localized to a ligand perpendicular to the surface. Hence, coupling of the radiative transition to the metal could not occur as required by an energy transfer mechanism. Similar considerations apply to $Os(bpy)_3^{2+}$ where the emission spectrum is quite different and yet the time constant for deactivation on the surface of an Ag colloid is quite similar to that of $Ru(bpy)_3^{2+}$.

Since the dipole-dipole mechanism does not apply, the mechanism for the quenching of $Ru(bpy)_3^{2+}$ and $Os(bpy)_3^{2+}$ luminescence must involve either energy transfer by the Dexter mechanism or electron transfer [38] An electron transfer mechanism for deactivation is not only reasonable, but has precedent in a large number of metal complexes where various ligand-to-metal charge transfer states can provide a route to rapid deactivation of a molecule[20, 27, 39-41] [39-41]. Kamat and coworkers have reported direct spectroscopic evidence for electron transfer between a gold nanoparticle and a surface-bound fluorophore induced by pulsed laser irradiation[27, 42] [42]. A classic example of this type of rapid deactivation is found in iron porphyrins where the non-radiative decay has a time constant of ca. 3 ps [43]. In the present case the non-radiative decay times range from 400 ps to 1200 ps on Au and Ag nanoparticles. In other words, the observed decay times are not vastly different for $Ru(bpy)_3^{2+}$ and $Os(bpy)_3^{2+}$ complexes adsorbed onto the surfaces of Ag or Au nanoparticles. Rapid electron transfer (charge injection) from $Ru(bpy)_3^{2+}$ or similar ruthenium complexes into $TiO_2$ semi-conductors is well-known and has been studied in order to maximize the efficiency of collection of sunlight on semi-conducting electrodes [44-46]. While recombination does not occur in the $TiO_2$ system, it likely occurs in Au and Ag nanoparticles. The sequential electron transfer quenching mechanism is given in Eqn. 3.8.

$Ru(bpy)_3^{2+}$ - **Au** → $Ru(bpy)*_3^{2+}$ (MLCT) - **Au** → $Ru(bpy)_3^{3+}$ - **Au**$^{-}$ → $Ru(bpy)_3^{2+}$ - **Au** (3.8)

Energy transfer by the Dexter mechanism is essentially a double electron transfer [38]. If the two electron transfer processes shown in Eqn. 3.8 occur in a concerted mechanism then the quenching is formally equivalent to Dexter energy transfer.

### 3.2.5 Conclusion

A method of determining the number of surface-adsorbed molecules has been demonstrated for both Au and Ag nanoparticles. The method provides an estimate of surface displacement reactions, since the time constant for deactivation of an adsorbed probe molecule depends on the proximity to the Au or Ag surface. For Au nanoparticles, a profound difference is observed between citrate stabilization and MO stabilization. The $Ru(bpy)_3^{2+}$ complexes displace citrate and are apparently adsorbed directly onto the nanoparticle. However, for MO stabilized Au nanoparticles there were three kinetic phases suggesting that some displacement occurred, but that there was also a fraction of the $Ru(bpy)_3^{2+}$ complexes more loosely associated with the surface. For these complexes the time constant lies between that for a physisorbed complex and for $Ru(bpy)_3^{2+}$ in solution.

The systems studied provide evidence for an electron transfer deactivation mechanism. The similarity in deactivation lifetimes for all of the polypyridyl complexes adsorbed to nanoparticles suggests that electron transfer from the MLCT state to the surface followed by back electron transfer provides the dominant deactivation mechanism that competes with luminescence. The distinction between electron transfer and energy transfer quenching reduces to the difference in time scale. If the forward and reverse electron transfers are concerted the electron transfer mechanism is formally identical to Dexter energy transfer.

## *3.3 Sandwich Hybridization Assay of DNA*

Dunn and Hassell first described the sandwich hybridization format in 1977. The sandwich assay is more advantageous than the routine direct hybridization because of its simple approach and higher specificity. The sample immobilization step is eliminated and crude samples can be analyzed with relative ease. The specificity is higher than direct hybridization assays owing to the fact that two hybridization events have to occur to generate a hybridization signal. [47] To further lower the detection limit in comparison to fluorescence spectroscopy, target can be labeled with colloidal gold nanoparticles. Mirkin et al. [48] [18] used a flatbed scanner for detection in a scheme where gold and silver nanoparticles were used, yielding detection as low as 50 fM. The target oligonucleotide was covalently attached to a gold colloid through a Au-S bond. When the target hybridizes with its complementary probe strand on the polycrystalline gold substrate, tapping mode AFM can be employed to visually see the colloids. As the microscope tip taps across the gold substrate, an apparent height image is obtained. The 10nm gold colloids are higher than the gold surface, so they appear as yellow dots on the AFM images.

### 3.3.1 Instrumentation

Tapping mode AFM was performed to view the gold substrate to determine the number of gold colloids bound to the substrate through hybridized DNA. An average particle count was obtained per square centimeter.

### 3.3.2 Methods and material

Target oligonucleotides were prepared by combining one equivalent of T20 oligonucleotide with one equivalent of 10nm gold colloids at varying concentrations in a 0.1M sodium chloride 0.01M sodium citrate hybridization solution. The target solution stirred for 1 hour at room temperature. A gold slide containing a mixed monolayer of 20% R20 oligonucleotide (the complement of T20) and 80% 6-mercapto-1-hexanol was then immersed in the target solution. The temperature was brought to 45°C for 1 hour then slowly cooled to room temperature over a 16 hour period. AFM was used to analyze the samples. Figure 3.7 A demonstrates an increase in target hybridization with an increase in target concentration. Figure 3.7 B, a plot of particles/cm$^2$ vs. target concentration, demonstrates that hybridization is directly proportional to target concentration. A 20% R20 probe slide was also exposed to a 6nM non-complementary target solution. The AFM image is shown in Figure 3.7 C and plotted in Figure 3.7 B. The results showed a small amount of non-specific binding.

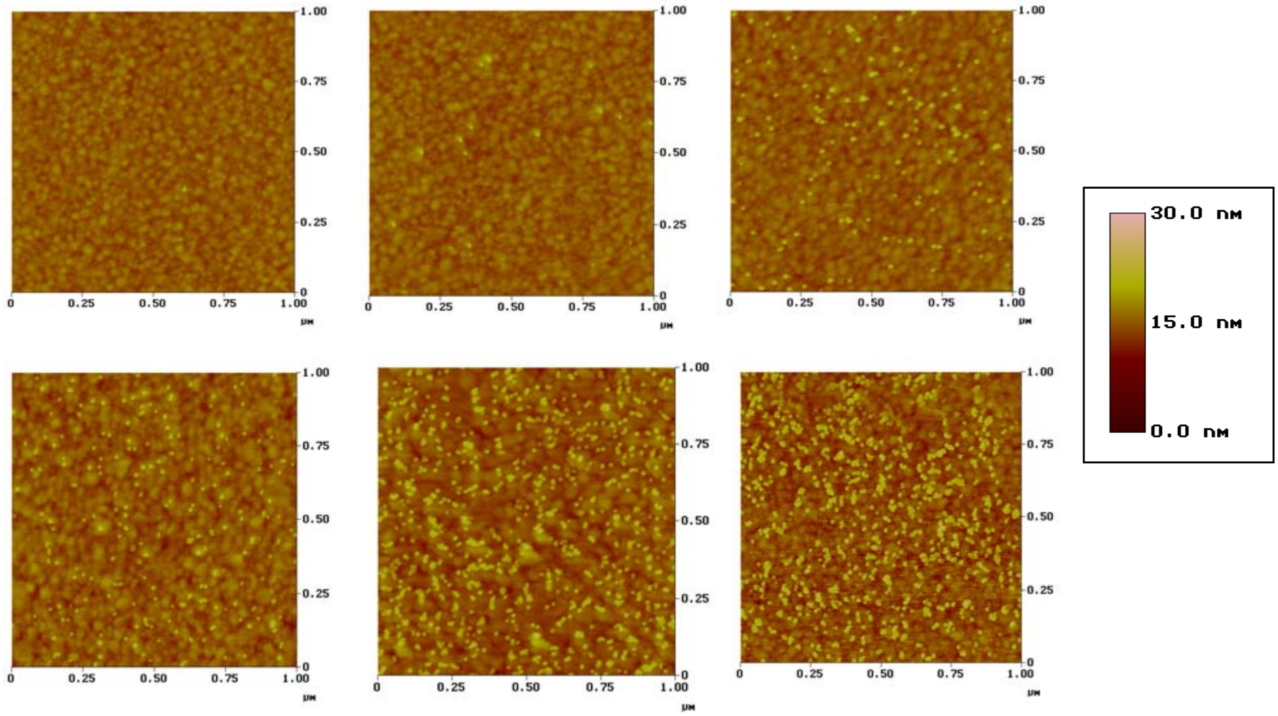


**Figure 3.7 A Target solution at various concentrations during hybridization: 0.25nM (A), 0.50nM (B), 1.0nM (C), 2.0nM (D), 4.0nM (E), and 6.0nM (F)**

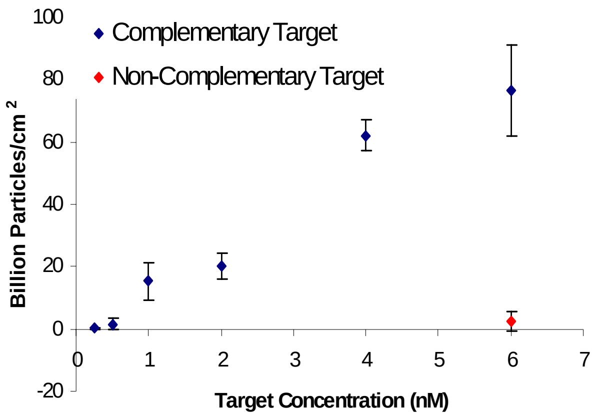


**Figure 3.7. B Plot of Particle count vs target concentration.**

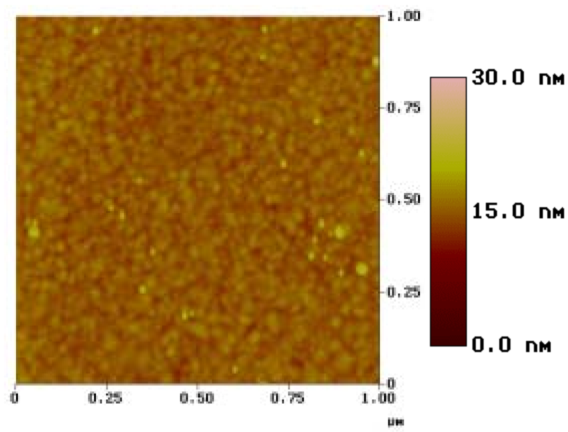


**Figure 3.7.C AFM image of noncomplimentary sequence checked for non specificity at 6 nM target concentration**

The probe DNA strand, the oligonucleotide functionalized nanoparticle label and the targets to be detected were designed to cohybridise in a sandwich assay. [48] [18] The concentration of gold colloid was kept constant at 250 pM and the ratio of DNA(R15D) strands per gold colloid was varied as 1, 10 and 100. The results were analyzed using AFM and Figure 3.9 shows clearly that hybridization efficiency increases on increasing the ratio of oligonucleotide to colloid. The binding curve of this result is plotted in Figure 3.10.

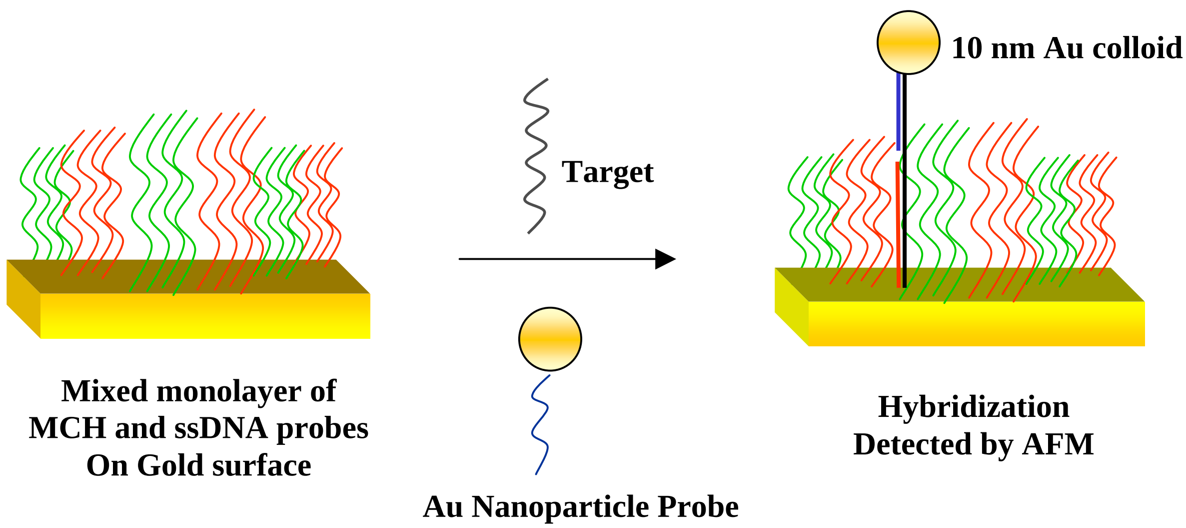

Figure 3.8 Schematic of hybridization assay in a sandwich assay format.

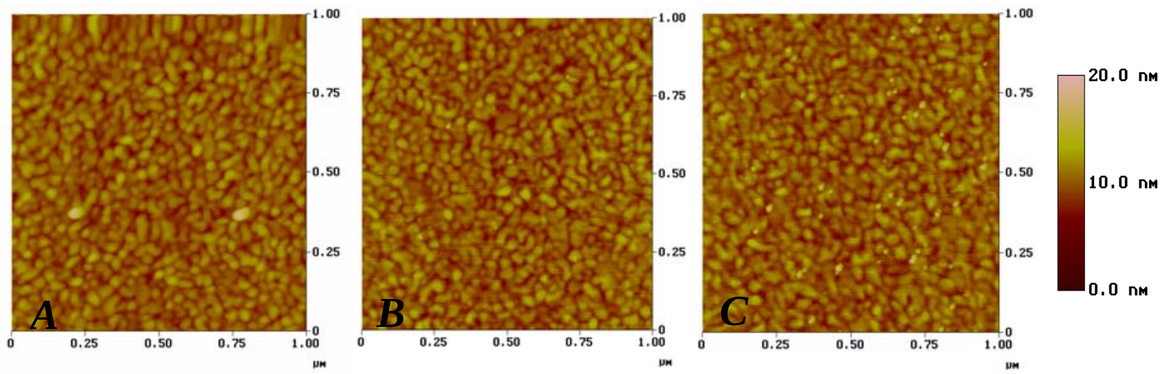


**Figure 3.9. AFM Images from Avidity Study - varying ratio of target oligonucleotide to gold colloid: 0.5 (A), 5.0 (B), and 50 (C).**

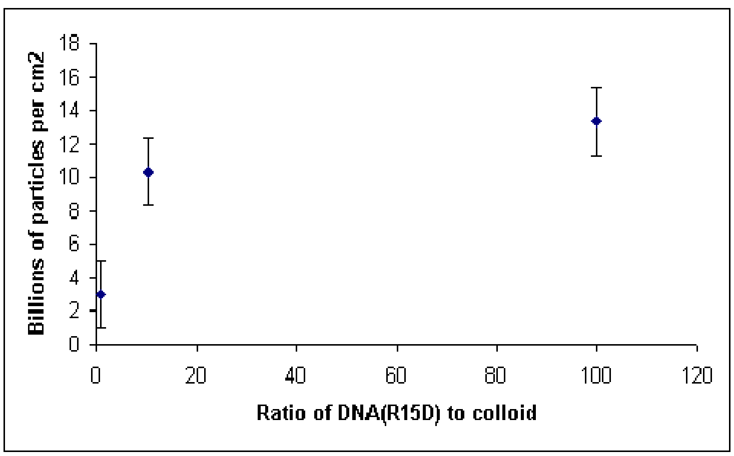


**Figure 3.10. Bnding Curve from Avidity Study-varying ratio of target oligonucleotide to gold colloid: 1 (A), 10 (B), and 100 (C).**

## *Acknowledgements*

This work was done in collaboration with Wilhelm R. Glomm (NCSU) and John M. Papanikolas at UNC – Chapel Hill. S.F. gratefully acknowledges support from NSF Grant MCB-9874895.

## *References*


1. Faraday, M., Philos. Trans. R. Soc. London, 1857(147): p. 145.
2. Link, S.A.E.-S., Int. Rev. Phys. Chem., 2000. 19: p. 409.
3. He, L., Musick, M. D., Nicewarner, S. R., Salinas, F. G., Benkovic, S. J., Natan, M. J. & Keating, C. D., Journal of the American Chemical Society, 2000. 122: p. 9071-9077.
4. Ramanathan, M., Weinstock-Guttman, B., Nguyen, L. T., Badgett, D., Brownscheidle, C. & Jacobs, L. D., Annals of Neurology, 2000. 48: p. 280.
5. Gerion, D., Parak, W. J., Williams, S. C., Zanchet, D., Micheel, C. M. & Alivisatos, A. P., Journal of the American Chemical Society, 2002. 124: p. 7070-7074.
6. Wang, G.L., J. Zhang, and R.W. Murray, DNA binding of an ethidium intercalator attached to a monolayer-protected gold cluster. Analytical Chemistry, 2002. 74(17): p. 4320-4327.
7. Gole, A., Dash, C., Soman, C., Sainkar, S. R., Rao, M. & Sastry, M., Bioconjugate Chemistry, 2001. 12: p. 684-690.
8. Yang, W.J., Trau, D., Renneberg, R., Yu, N. T. & Caruso, F., Journal of Colloid and Interface Science, 2001. 234: p. 356-362.
9. Schaertl, S., Meyer-Almes, F. J., Lopez-Calle, E., Siemers, A. & Kramer, J., Journal of Biomolecular Screening, 2000. 5: p. 227-237.
10. Schultz, S., Mock, J., Smith, D. R. & Schultz, D. A., Journal of Clinical Ligand Assay, 1999. 22: p. 214-216.
11. Ishihara, K., Inoue, H., Kurita, K. & Nakabayashi, N., Journal of Biomedical Materials Research, 1994. 28: p. 1347-1355.
12. Muller, R.H., Lherm, C., Herbort, J., Blunk, T. & Couvreur, P., International Journal of Pharmaceutics, 1992. 84: p. 1-11.
13. W. B. Russel, D.A.S., and W. R. Schowalter, Colloidal Dispersions. 1989: Cambridge University Press, Cambridge.
14. Cao, Y.W.J., R.; Mirkin, C. A., J. Am. Chem. Soc.; (Communication), 2001. 123(32): p. 7961-7962.
15. Templeton, A.C., Hostetler, M. J., Kraft, C. T. & Murray, R. W., J. Am. Chem. Soc.; (Communication), 1998. 120: p. 1906-1911.
16. Templeton, A.C., et al., Gateway reactions to diverse, polyfunctional monolayer-protected gold clusters. Journal of the American Chemical Society, 1998. 120(19): p. 4845-4849.
17. Templeton, A.C., M.P. Wuelfing, and R.W. Murray, Monolayer protected cluster molecules. Accounts of Chemical Research, 2000. 33(1): p. 27-36.
18. Taton, T.A.L., G.; Mirkin, C. A., J. Am. Chem. Soc.; (Communication), 2001. 123: p. 5164-5165.
19. Sudeep, P.K., et al., Fullerene-functionalized gold nanoparticles. A self-assembled photoactive antenna-metal nanocore assembly. Nano Letters, 2002. 2(1): p. 29-35.
20. Ipe, B.I., et al., Photoinduced charge separation in a fluorophore-gold nanoassembly. Journal of Physical Chemistry B, 2002. 106(1): p. 18-21.

21. Huang, T. and R.W. Murray, Quenching of Ru(bpy)(3) (2+) fluorescence by binding to Au nanoparticles. Langmuir, 2002. 18(18): p. 7077-7081.
22. Forster, R.J. and T.E. Keyes, Redox properties of ground and electronically excited states: [Ru(bpy)(2)Qbpy](2+) monolayers. J. Phys. Chem. B, 1998. 102: p. 10004-10012.
23. Fleming, C.N., et al., Ultrafast excited-state energy migration dynamics in an efficient light-harvesting antenna polymer based on Ru(II) and Os(II) polypyridyl complexes. Journal of the American Chemical Society, 2001. 123(42): p. 10336-10347.
24. Fleming, C.N., et al., Energy transfer between Ru(II) and Os(H) polypyridyl complexes linked to polystyrene. Journal of Physical Chemistry A, 2002. 106(10): p. 2328-2334.
25. Shaw, G.B., C.L. Brown, and J.M. Papanikolas, Investigation of interligand electron transfer in polypyridyl complexes of Os(II) using femtosecond polarization anisotropy methods: Examination of Os(bpy)(3)(2+) and Os(bpy)(2)(mab)(2+). Journal of Physical Chemistry A, 2002. 106(8): p. 1483-1495.
26. Franzen, S., et al., Optical Properties of Dye Molecules Adsorbed on Single Gold and Silver Nanoparticles. The Journal of Physical Chemistry A, 2002. 106(28): p. 6533-6540.
27. Kamat, P.V., Photophysical, Photochemical and Photocatalytic Aspects of Metal Nanoparticles. Journal of Physical Chemistry B, 2002. 106: p. 7729-7774.
28. Thomas, K.G., J. Zajicek, and P.V. Kamat, Surface binding properties of tetraoctylammonium bromide-capped gold nanoparticles. Langmuir, 2002. 18(9): p. 3722-3727.
29. McHale, J.L., Molecular Spectroscopy. 1 ed, ed. J. Challice. 1999, Upper Saddle River: Prentice Hall. 463.
30. Houten, V. and R.J. Watts, Temperature Dependence of the Photophysical and Photochemical Properties of the Tris(2,2'-bipyridyl)Ruthenium Ion in Aqueous Solution. JACS, 1976. 98(16).
31. Javier, A., et al., Energy transport in CdSe nanocrystals assembled with molecular wires. Journal of Physical Chemistry B, 2003. 107(2): p. 435-442.
32. Lakowicz, J.R., et al., Radiative Decay Engineering 2. Effects of Silver Island Films on Fluorescence Intensity, Lifetimes, and Resonance Energy Transfer. Analytical Biochemistry, 2002. 301: p. 261-277.
33. Sirota, M., et al., Spectroscopic Properties of Molecular-Wire/Semiconductor Nanocrystalline Superstructures. Journal of Physical Chemistry B, 2001. 105: p. 6792-6797.
34. Dulkeith, E., et al., Fluorescence quenching of dye molecules near gold nanoparticles: Radiative and nonradiative effects. Physical Review Letters, 2002. 89(20): p. art. no.-203002.
35. Perez-Luna, V.H., et al., Fluorescence biosensing strategy based on energy transfer between fluorescently labeled receptors and a metallic surface. Biosensors & Bioelectronics, 2002. 17(1-2): p. 71-78.

36. Maxwell, D.J., J.R. Taylor, and S.M. Nie, Self-assembled nanoparticle probes for recognition and detection of biomolecules. Journal of the American Chemical Society, 2002. 124(32): p. 9606-9612.
37. Forster, T., 10th Spiers memorial lecture - transfer mechanisms of electronic excitation. Disc. Faraday Soc., 1959. 27: p. 7-17.
38. Altarell, M. and D.L. Dexter, Simultaneous energy transfer and optical absorption in concensed matter. Phys. Rev. B, 1973. 7: p. 5335-5344.
39. Nikoobakht, B., et al., The quenching of CdSe quantum dots photoluminescence by gold nanoparticles in solution. Photochemistry and Photobiology, 2002. 75(6): p. 591-597.
40. Enger, O., et al., Photocurrent generation at a fullerene self-assembled monolayer-modified gold electrode cast with a polyurethane membrane. Journal of Materials Chemistry, 2000. 10: p. 2231-2233.
41. Kamat, P.V. and B. Shanghavi, Inerparticle Electron Transfer in Metal/Semiconductor Composites. Picosecond Dynamics of CdS-Capped Gold Nanoclusters. Journal of Physical Chemistry B, 1997. 101(39): p. 7675-7679.
42. Kamat, P.V., M. Flumiani, and A. Dawson, Metal-metal and metal-semiconductor composite nanoclusters. Colloids and Surfaces a-Physicochemical and Engineering Aspects, 2002. 202(2-3): p. 269-279.
43. Franzen, S., et al., Heme photolysis occurs by ultrafast excited state metal-to-ring charge transfer. Biophysical Journal, 2001. 80(5): p. 2372-2385.
44. Kuciauskas, D., et al., Transient absorption spectroscopy of ruthenium and osmium polypyridyl complexes adsorbed onto nanocrystalline TiO2 photoelectrodes. J. Phys. Chem. B, 2002. 106: p. 9347-9358.
45. Yang, M., D.W. Thompson, and G.J. Meyer, Charge-transfer studies of iron cyano compounds bound to nanocrystalline $TiO_2$ surfaces. Inorg. Chem., 2002. 41: p. 1254-1262.
46. Kalyanasundaram, K. and M. Gratzel, Applications of functionalized transition metal complexes in photonic and optoelectronic devices. Coord. Chem. Rev., 1998. 177: p. 347-414.
47. George H. Keller, M.M.M., DNA Probes. 1989: Macmillan Publishers Ltd.
48. Taton, T.A.M., C. A.; Letsinger, R. L., Science, 2000. 289: p. 1757.

# CHAPTER 4

## Characterization and quantitation of ssDNA and detection of hybridization of DNA on gold substrates

## *Abstract*

Single and double stranded deoxy ribonucleic acid (DNA) molecules attached to self-assembled monolayers on gold surfaces were characterized by a number of optical and electronic spectroscopic techniques. The DNA-modified gold surfaces were prepared through the self-assembly of 6-mercapto-1-hexanol and 5'-$C_6H_{12}SH$ -modified single-stranded DNA (ssDNA). Upon hybridization of the surface-bound probe ssDNA with its complimentary target, formation of double-stranded DNA (dsDNA) on the gold surface is observed and in a competing process, probe ssDNA is desorbed from the gold surface. The competition between hybridization of ssDNA with its complimentary target and ssDNA probe desorption from the gold surface has been investigated in this paper using X-ray photoelectron spectroscopy (XPS), chronocoulometry, fluorescence and polarization modulation-infrared reflection absorption spectroscopy (PM-IRRAS). The formation of dsDNA on the surface was identified by PM-IRRAS by a dsDNA IR signature at ~1678 $cm^{-1}$ that was confirmed by density functional theory (DFT) calculations of the nucleotides and the nucleotides base pairs. The presence of dsDNA through the specific DNA hybridization was additionally confirmed by atomic force microscopy (AFM) through colloidal gold nanoparticle labeling of the target ssDNA. Using these methods strand loss was observed even for DNA hybridization performed at 25 $^{o}$C for the DNA monolayers studied here consisting of attachment to the gold surfaces by single Au-S bonds. This finding has significant consequence for the application of self-assembled monolayer technology in the detection of oligonucleotide hybridization on gold surfaces.

## 4.1 Introduction

DNA arrays have numerous applications in the fields of diagnostics, genome sequencing and gene mapping.[1-4] A variety of substrates such as glass,[5,6] indium tin oxide (ITO) [7,8] and gold[9-11] have been used to develop sensitive, high throughput genomic arrays. The formation of these arrays typically involves a self-assembly process. For instance on gold surfaces, thiol-modified ssDNA is used to attach the probe strands to the surface. Some assays use gold nanoparticles to detect the presence of DNA targets.[12] A number of assays rely upon gold-thiol attachment chemistry that is known to be both thermodynamically and kinetically labile.[13] Thus, it is important to understand the consequences of DNA hybridization at gold surfaces, particularly at the elevated temperatures often used to accelerate hybridization kinetics.

Gold surfaces coated with self-assembled monolayers with attached ssDNA and dsDNA have been characterized by several techniques including fluorescence,[14-17] surface plasmon resonance,[11,18-22] electrochemistry[4,10,23] and infrared spectroscopy.[24] However, fundamental work on the characterization of DNA-modified surfaces is still needed to fully understand these systems. The quantitation of DNA hybridization and integrity of the surface adlayer at various temperatures are both outstanding issues that need to be addressed.

In this study, several different techniques were used to characterize ssDNA monolayers on planar gold surfaces. The self-assembled monolayers (SAMs) of DNA were prepared using a 5'-$C_6H_{12}SH$ ssDNA probe strand and 6-mercapto 1-hexanol. The techniques utilized to investigate the ssDNA modified gold surfaces included X-ray photoelectron spectroscopy (XPS), polarization modulation infrared reflectance absorption spectroscopy (PM-IRRAS), chronocoulometry and fluorescence, while PM-IRRAS and atomic force microscopy (AFM) were used to determine the presence of dsDNA on the gold surfaces through surface DNA hybridization. The stability of ssDNA self-assembled monolayers on gold was investigated through thermal desorption studies at a variety of temperatures used in typical hybridization procedures. Density functional theory calculations were also performed on the individual nucleotides and nucleotide base pairs to allow insight into the spectroscopic difference between single and double-stranded DNA observed experimentally using infrared spectroscopy on gold surfaces.

## *4.2 Methods and Materials*

### 4.2.1 Materials

Polycrystalline gold deposited on a glass microscope slide containing a chromium oxide passivation layer was obtained from Evaporated Metal Films, Inc. Millipore 18 MΩcm water was used for all solutions from a BARNSTEAD E-PURE system. All the oligonucleotides were received from Applied Biosystems Incorporated. $KH_2PO_4$, $K_2HPO_4$ (KP buffer) and saline-sodium citrate (20XSSC) were purchased from Fisher Scientific. 6-Mercapto-1-hexanol (MCH) was purchased from Sigma-Aldrich. Tris(hydroxymethyl)-aminomethane was purchased from Bio-Rad Laboratories and hexaammineruthenium(III) chloride $[Ru(NH_3)_6]^{3+}$ was purchased from Strem Chemicals. Mercaptoethanol (MCE) was purchased from Fisher Scientific.

### 4.2.2 DNA Monolayer Formation

Gold slides were first cleaned with piranha solution (70% conc. $H_2SO_4$: 30%$H_2O_2$ (30%); CAUTION: piranha solution reacts violently with organic chemicals) and rinsed with 18 MΩcm deionized water. The single-stranded DNA (ssDNA) probe strand was modified at the 5' end with a $C_6$-S-disulfide modifier that was deprotected to form the 5' $C_6$-SH linker as reported previously. [12] A 1 μM solution of the probe was made in 1 M potassium phosphate buffer (pH 7.0) into which the cleaned gold slides were soaked overnight (16 hours) followed by a 1hr deposition in 1 mM MCH in water. The gold slides were then rinsed with 18 MΩcm deionized water and placed in a hybridization solution of 1X SSC at 25 °C, 45 °C, 65 °C or 85 °C with 1 μM target ssDNA (exact complement to the probe oligo on the gold surface). Surface DNA hybridization was achieved by gradually cooling to room temperature over a period of 3 hours. The surfaces were then rinsed in 18 MΩcm deionized water and dried with nitrogen gas. For AFM studies, the target was labeled with gold nanoparticles as reported previously. [12]. The high concentration of salt commonly used for hybridization results in aggregation of gold colloids used as target DNA label. Therefore, in all the experiments reported in this paper 0.15 M NaCl is used in the hybridization solution to prevent gold nanoparticle aggregation.

For the desorption studies, a co-deposition solution containing mole fraction of 0.1 and 0.9 of ssDNA and MCH, respectively for a total concentration of in 1 μM. The buffered solution (1 M potassium phosphate buffer, pH 7.0) was used to make the MCH/ssDNA mixed monolayer. DNA hybridization was attempted on substrates with co-deposited ssDNA/MCH monolayers, however, the hybridization yield was observed to be much lower most likely due to the fact that the monolayer formation is not as complete (defect-free) as for the sequential deposition substrates. Therefore, we present only DNA hybridization data obtained on substrates prepared by sequential deposition.

### 4.2.3 Oligonucleotides.

With the exception of the DNA desorption studies reported here, the probe ssDNA sequence used for the XPS, PM-IRRAS, AFM and electrochemistry experiments was 5'-AACCAGGATTATCCGCTCAC -3' (P1) the target was the exact complement to the probe ssDNA strand. For the AFM experiment the target had a 5' $C_6$-SH linker that was labeled with 10 nm gold colloid. P2 probe ssDNA was used for the gold-thiol desorption experiments with a sequence of 5'-AACCAGGATATCCGCTCACAATTCC-3' (P2). Both ssDNA probe strands had a 5' $C_6$-SH linker. The ssDNA probe used for the fluorescence studies was a 30-mer with a sequence of 5'-SH-$C_6$-GGAGACTGTTATCCGCTCAGAATTCCACAC-F 3' (P3), where F is a fluorescein.

## *4.3 Instrumentation*

### 4.3.1 X-ray Photoelectron Spectroscopy (XPS)

All XPS spectra were recorded on a Riber LAS 2000 Surface Analysis System equipped with a cylindrical mirror analyzer (CMA) and a MAC2 analyzer with Mg K$\alpha$ X-rays (model CX 700 (Riber source) ($h\nu$ = 1253.6 eV). The incident angle at which the X-rays hit the sample was 20$^o$ from the plane of the surface. The analyzer is 75$^o$ from the plane of the surface. The angle between the incident X-rays and the analyzer is 55$^o$. The spectral resolution for all the scans was 1.0 eV and the spectra were the result of 10 scans. XPS spectra were baseline corrected and the peaks were fitted using Gaussian line shapes. Internal normalization was not carried out for the N 1s peaks.

### 4.3.2 Polarization Modulation Infrared Reflection Absorption Spectroscopy (PM-IRRAS).

The PM-IRRAS spectra were recorded on a Digilab FTS 6000 spectrometer equipped with a step scan interferometer, liquid nitrogen cooled narrow band MCT detector, globar source and a UDR-8 filter. The IR radiation was typically phase modulated at frequencies of 400 or 800Hz at an amplitude of 1.0 or 2.0 λ HeNe while stepping at 0.5 - 2.5 Hz. A gold grid polarizer was used to obtain either s- or p-polarized radiaton, which was then modulated by a Hinds ZnSe PEM operating at 37 KHz and amplitude of 0.5 λ (strain axis 45 degrees to the polarizer) before reflecting off the sample at an incident angle of 80 degrees from the surface normal. The spectra were recorded at room temperature at a resolution of 8 $cm^{-1}$ and were the result of a single scan with a spectral range of 900 – 1800 $cm^{-1}$. The digital signal processing (DSP) algorithm incorporated into the Digilab spectrometer software was used to obtain the spectra. This technique eliminated the need for a separate reference bare gold slide.

### 4.3.3 Density Functional Theory (DFT) Calculations.

The geometry optimization and vibrational frequency calculations of the individual DNA bases and complementary base pairs were done using density functional theory (DFT) as implemented in the quantum chemistry software program DMol3 (Accelrys, Inc.). [25] The calculations were performed at the North Carolina Supercomputer Center (NCSC) on the IBM RS/6000 SP. These calculations were done in the gas phase using the DND basis set, the GGA functional [26] and the method of finite differences for calculating the vibrational frequencies. The Accelrys, Inc. software

Insight II was used to build the models and to visualize the eigenvector projections of the calculated vibrational modes of the models.

### 4.3.4 Electrochemical Measurements.

Chronocoulometry was performed on an EG & G Princeton Applied Research instrument (Potentiostat Model 273A). A three electrode cell consisting of Ag/AgCl as the reference electrode and a Pt wire as the counter electrode was used for the electrochemical measurements. The electrode area was 0.36 $cm^2$. The measurements were done in Tris buffer (pH 7.1) in the presence and absence of 50 μM $[Ru(NH_3)_6]^{3+}$ after purging it thoroughly with $N_2$ gas.

The surface density of probe DNA can be calculated using the assumption that one $[Ru(NH_3)_6]^{3+}$ molecule binds to the anionic phosphodiester backbone of DNA for every three bases [4] The integrated Cottrell equation, which expresses charge Q, as a function of time, can be used to calculate the surface excess term.

$$Q = \frac{2nFAD_0^{1/2}C_0^*}{\pi^{1/2}}t^{1/2} + Q_{dl} + nFA\Gamma_0 \qquad (4.1)$$

Where n is the number of electrons per molecule for reduction, $F$ is Faraday constant (C/equiv), $A$ the electrode area ($cm^2$), $D_0$ the diffusion coefficient ($cm^2/s$), $C_0^*$ bulk concentration ($mol/cm^2$), $Q_{dl}$ the capacitive charge(C), and $nFA\Gamma_0$ the charge from the reduction of $\Gamma_0$ ($mol/cm^2$) of adsorbed $[Ru(NH_3)_6]^{3+}$. The surface excess term $\Gamma_0$ denotes the amount of redox marker confined at the surface of the electrode. The double layer charge and the charge due to reaction of species adsorbed on the electrode surface can be differentiated from the charge due to reaction of redox molecules that diffuse to the electrode surface. The difference of the chronocoulometric intercepts of the experiments done under identical conditions with and without the redox marker yields the surface term. The surface density on the electrode surface can be calculated from this term using the relation

$$\Gamma_{\mathrm{DNA}} = \Gamma_0 \left( z/m \right) (N_A) \qquad (4.2)$$

### 4.3.5 Atomic Force Microscopy.

The gold surface modified with ssDNA/MCH and hybridized with 10 nm gold colloid labeled complimentary target DNA was imaged by Digital Instruments Nanoscope IIIa Scanning Probe Microscope in tapping mode. AFM images were captured with Nanoscope IIIa software version 4.23r6. The images were captured at 1μm scan size with a height scale of 30 nm.

### 4.3.6 Fluorescence Measurements

. The probe ssDNA labeled with a fluorescein tag on the 3' end was displaced from the gold surface by placing the slide in a 12 mM MCE solution,[27] and heating to 45 °C for at least 8 hours. This displacement procedure was repeated a second time to ensure complete removal, followed by two washes in KP buffer. The solution fluorescence measurements were recorded on a PTI QuantaMaster Model C-60/2000 spectrofluorometer with an excitation wavelength of 492 nm and the emission maximum was detected at 520 nm. The concentration of ssDNA displaced from the gold slide was determined from a calibration curve of the fluorescence peak area vs. known ssDNA concentrations (data not shown). These ssDNA concentrations from the displaced ssDNA were used to determine the surface coverage on the gold slides prior to the displacement of the ssDNA by MCE. The area of the cut gold piece was determined by comparing the weight of the as-received gold slide (with a known surface area) to the weight of the cut gold substrate piece, assuming uniform thickness.

## *4.4 Results*

The competition between DNA hybridization and desorption of thiolated ssDNA and dsDNA (hybridized) strands from the gold surface prevents separate quantitation of these two phenomena. Therefore, we have studied the desorption separately in a series of experiments on ssDNA modified gold surfaces. Data relevant to DNA hybridization to ssDNA probe molecules is presented subsequently.

### 4.4.1 ssDNA Modified Gold Surfaces

#### 4.4.1.1 X-ray photoelectron spectroscopy (XPS).

The XPS spectra of nitrogen (1s) for an adlayer of MCH/ssDNA on a gold slide is shown in Figure 4.1 fit to a Gaussian line

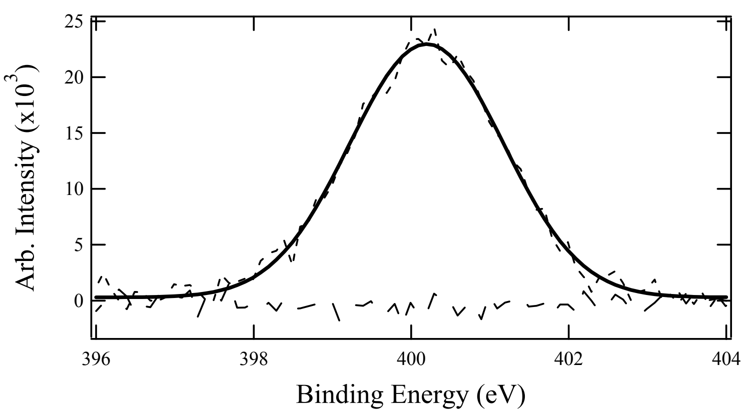


**Figure 4.1. XPS spectra of the N 1s region for a mixed monolayer of MCH/ssDNA. The dashed line corresponds to an adlayer of MCH in all three spectra. The raw data (dots) were fit to Gaussian line shapes (solid).**

shape. The area of the Gaussian line shape is proportional to the amount of nitrogen on the surface. A pure MCH monolayer (Figure 4.1) on a gold slide was used as a control that did not exhibit any detectable nitrogen signal. Hence, the N 1s signal for the MCH/ssDNA modified gold surface arises entirely from the nitrogen in the purine and pyrimidine bases of DNA. As seen in Figure 4.1, the peak at 400.2 eV corresponds to the N 1s orbital from the ssDNA on the surface. Since temperature is a key factor in determining the hybridization yield of DNA on surfaces, further studies were carried out to quantitate the loss of ssDNA probe strands from the gold substrate upon heating in the hybridization buffer in the presence or absence of its compliment at various temperatures. Substrates with a mixed monolayer of MCH/ssDNA were heated up to 25 °C, 45 °C, 65 °C and 85 °C in a 1XSSC solution for an hour and cooled down to room temperature over a period of three hours and analyzed by XPS. The N 1s areas were compared to determine the relative surface coverage of DNA on the gold surface.

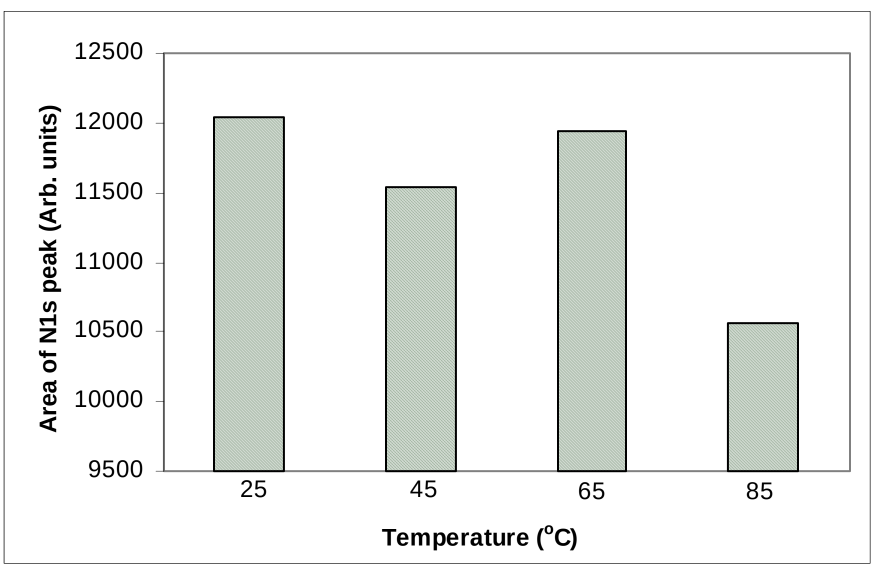


**Figure 4.2. Plot of N 1s XPS peak area as a function of temperature of an adlayer of MCH/ssDNA on gold heated to 25 °C, 45 °C, 65 °C and 85 °C respectively in 1XSSC.**

Figure 4.2 shows the plot of peak areas of the N 1s signal of a MCH/ssDNA monolayer on a gold surface as a function of temperature at which it was subjected to heating in 1XSSC buffer. The surface coverage decrease relative to the MCH/ssDNA sample at 25 °C is ~4%, ~0% and ~12% for 45 °C, 65 °C and 85 °C, respectively. The peak area of N 1s shows a steady decrease with the increase in temperature with the exception of 65 $^{o}$C, which seems to experience minimal ssDNA probe loss on the surface due to the hybridization conditions relative to the other temperatures studied.

#### 4.4.1.2 Polarization modulation infrared reflection absorption spectroscopy (PM-IRRAS).

PM-IRRAS was employed to characterize a mixed monolayer of MCH/ssDNA on a gold surface prior to hybridization. The raw data obtained by PM-IRRAS results in absorptive features corresponding to the surface species on a Bessel function background. Therefore baseline correction must be performed to analyze the spectra. Due to the short length of the ssDNA used for modifying the surface the signal intensity was low, as shown in Supporting Information, hence the baseline correction in this region was not easily discernable. Consequently, the same baseline correction was applied to all of the PM-IRRAS spectra and no baseline points were chosen in the 1550 – 1750 cm$^{-1}$ region due to peak positions shifts that occur between ssDNA and dsDNA on the gold surface (see below) to avoid any artifacts due to this processing step. In order to analyze the ssDNA and dsDNA PM-IRRAS spectra on the surface of gold, the spectra were fit to multiple Gaussian line shapes. The fit parameters for the Gaussians used to fit the ssDNA PM-IRRAS spectrum including the peak positions are given in Table 4.2. These modes in the 1550 – 1750 cm$^{-1}$ are indicative of the presence of ssDNA on the gold surface and result primarily form carbonyl stretching and N-H$_{(2)}$ bending vibrations from the DNA nucleobases. These modes are verified with density functional theory (DFT) calculations and difference spectra were utilized to determine peak position shifts and intensity differences between ssDNA and dsDNA at two different hybridization temperatures as shown below. Difference spectra were then utilized to determine peak position shifts and intensity differences between ssDNA and dsDNA at two different temperatures as shown below.

### 4.4.1.3 Chronocoulometry.

Chronocoulometric response of a gold surface modified with a mixed monolayer of MCH/ssDNA in the presence and absence of the electroactive species $[Ru(NH_3)_6]^{3+}$ can be used to quantitate ssDNA (See supporting Information). $[Ru(NH_3)_6]^{3+}$ (50 μM) was added to the Tris buffer electrolyte solution. As first described by Tarlov and coworkers[4], $[Ru(NH_3)_6]^{3+}$ ion pairs with ssDNA at the electrode surface and can be detected with chronocoulometry. Subtracting the chronocoulometric response of a bare electrode, and assuming a 1:3 binding ratio of $[Ru(NH_3)_6]^{3+}$:ssDNA yields quantitative results regarding the number of ssDNA strands bound to the gold electrode. The chronocoulometric intercepts for the gold substrate modified with MCH are nearly the same in the absence and presence of $[Ru(NH_3)_6]^{3+}$ thus ruling out the possibility of nonspecific adsorption of $[Ru(NH_3)_6]^{3+}$ at the gold surface in the absence of ssDNA.

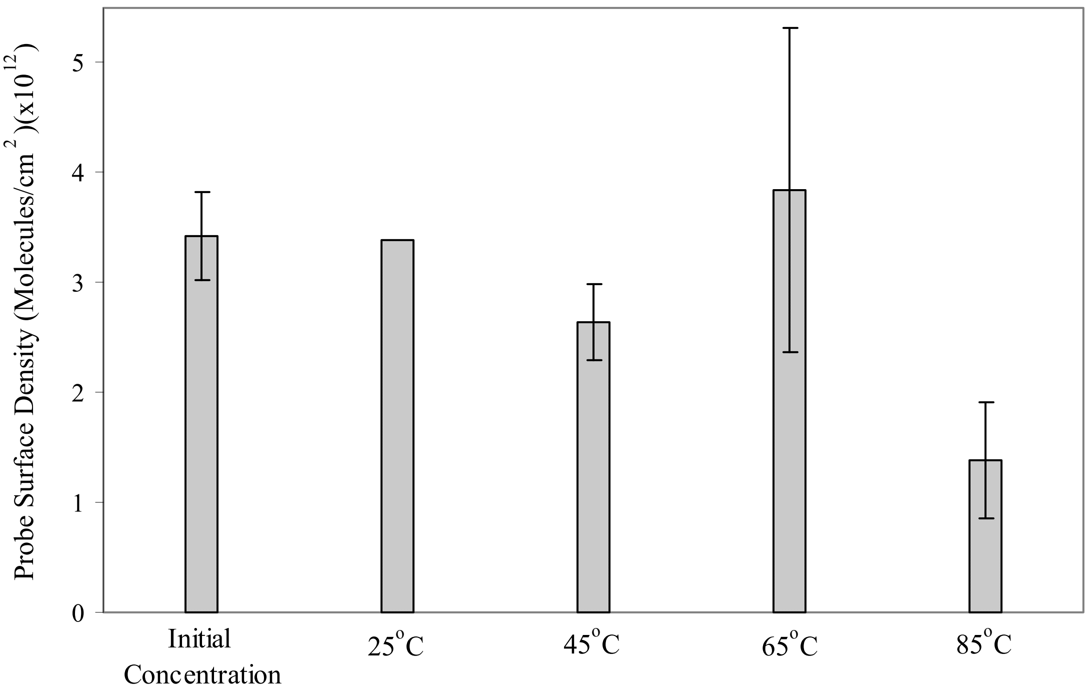


**Figure 4.3. Plot of surface probe density MCH/ssDNA adlayer on gold initially and after heating in 1XSSC at 25 °C, 45 °C, 65 °C and 85 °C respectively.**

Figure 4.3 is a plot of the probe surface density of ssDNA on the gold substrate calculated using the chronocoulometric data for the initial MCH/ssDNA monolayer and then exposing it to 1XSSC solution at 25 °C, 45 °C, 65 °C and 85 $^o$C under otherwise identical conditions. As observed with the XPS results, the surface coverage of probe DNA on the surface decreases under mock hybridization conditions with increasing temperature except at 65 $^o$C where an unexpectedly high signal was observed in multiple measurements. These results suggest that there is a balance between the loss of probe DNA from the gold surface and the temperature at which it is heated in hybridization buffer in the absence of complimentary target DNA. These results are in agreement with previous studies that have reported a loss of probe ssDNA strands from the surface due to desorption[24] at temperatures higher than the melting temperature of the dsDNA oligos where an increase in the hybridization yield might occur.

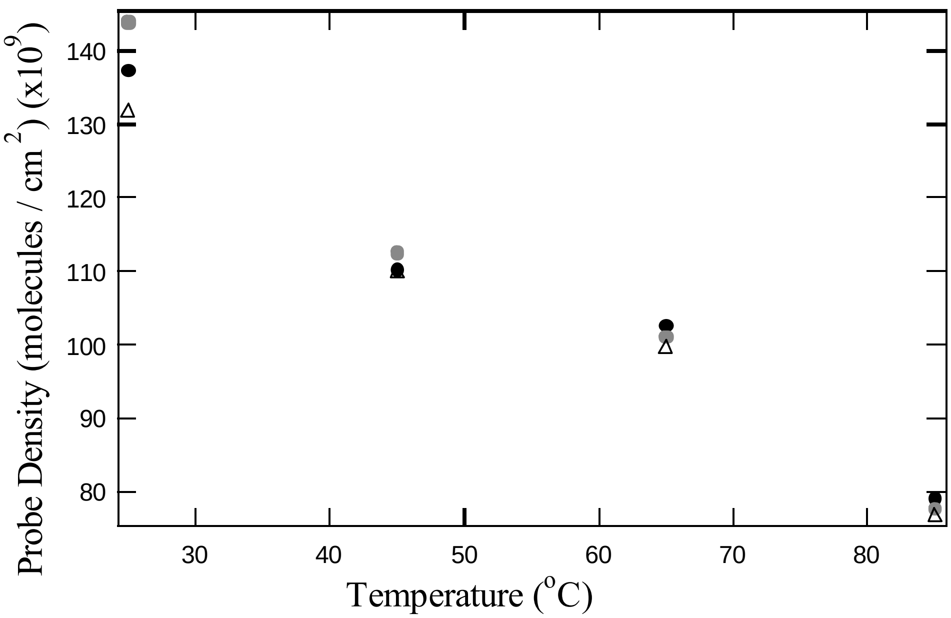


**Figure 4.4. Surface density of fluorescent tagged probe DNA adsorbed on gold substrates at 25 ºC, 45 ºC, 65 ºC, and 85 ºC.**

### 4.4.1.4 Fluorescence.

The fluorescence study in Figure 4.4 illustrates a linear trend with a decrease in the number of probe ssDNA strands (P3) adsorbed on the gold surface with an increase in temperature. The calculated probe density is ~ $10^{11}$ molecules/cm$^2$, a factor of 10 lower than the probe density calculated from the Cottrell equation. The fluorescence experiments on gold surfaces must contend with the quenching of fluorescein fluorescence and thus the measurements of the surface-attached oligonucleotides are always *ex situ* measurements of DNA extracted from the surface. Any losses or quenching from solution species will tend to reduce the fluorescence and result in a lower measured value for the surface coverage. Any incomplete displacement by MCE will also result in a lower value. Despite numerous replicates the fluorescence experiments yielded systematically lower values for the surface coverage than obtained by chronocoulometry.

## 4.4.2 DNA Hybridization on Gold Surfaces

### 4.4.2.1 X-ray photoelectron spectroscopy (XPS).

Table 4.1 present data obtained from the N 1s XPS spectra of the result of hybridization with the target to the surface-attached probe strand at 25 °C and 45 °C, respectively (see Supporting Information). These temperatures were chosen to investigate the competitive process of ssDNA strand loss and surface DNA hybridization. The MCH/ssDNA modified gold surfaces exposed to the complimentary ssDNA strand at 25 °C and 45 °C showed a decrease in the N 1s peak area by 17.7% and 39.1% respectively relative to the MCH/ssDNA modified surface. These results are shown in Table 4.1 and are indicative that probe desorption from the surface is the dominant process occurring and not DNA hybridization.

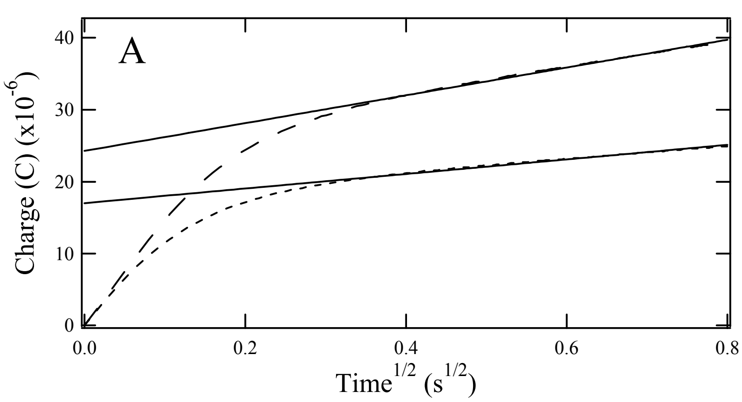

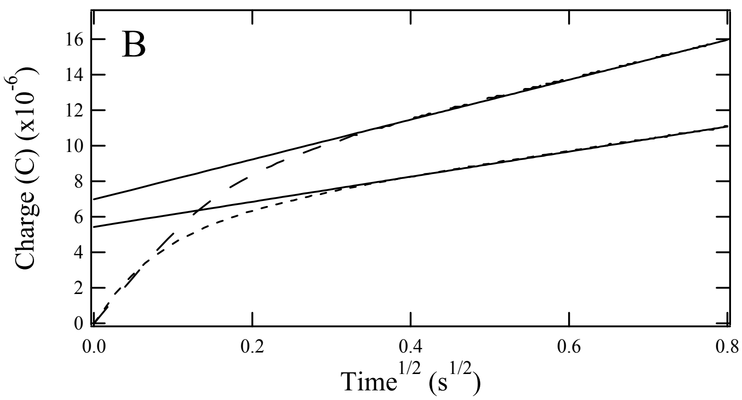


**Figure 4.5. Chronocoulometric response curves for modified electrode surfaces in the absence (dots) and presence (dashes) of 50 μM $[Ru(NH_3)_6]^{3+}$ in a buffer solution extrapolated to time zero from the linear portion of the curve (solid). A. dsDNA hybridized at 25 ºC. B. dsDNA hybridized at 45 ºC to a mixed MCH/ssDNA adlayer (solid) on a gold surface.**

### 4.4.2.2 Chronocoulometry.

Figure 4.5 shows the chronocoulometric response of a gold surface modified with a mixed monolayer of MCH/ssDNA hybridized with its complimentary strand at 25 °C (A) and 45 °C (B). $[Ru(NH_3)_6]^{3+}$ (50 μM) was added to the Tris buffer electrolyte solution to quantitate the amount of DNA on the surface. An average of at least three measurements was calculated to determine the probe density on the electrode surface for each temperature. Desorption of probe strands from the gold surface is seen at temperatures as low as 25 °C. The surface coverage for the gold electrode hybridized at either 25 °C or 45 °C is less than that of the MCH/ssDNA mixed monolayer at the corresponding temperature. The MCH/ssDNA sample that was hybridized with the complimentary target at 25 °C showed a 16±4 % decrease in surface coverage while the sample hybridized at 45 °C showed a decrease of 30±11 %.

### 4.4.2.3 Polarization modulation infrared reflection absorption spectroscopy (PM-IRRAS)

. As previously reported, PM-IRRAS allows for the detection of DNA hybridization on a gold surface as shown in Figure 4.6A and 4.6B. [24] The difference spectra (6C) are the result of subtracting the ssDNA spectra from the dsDNA spectra.

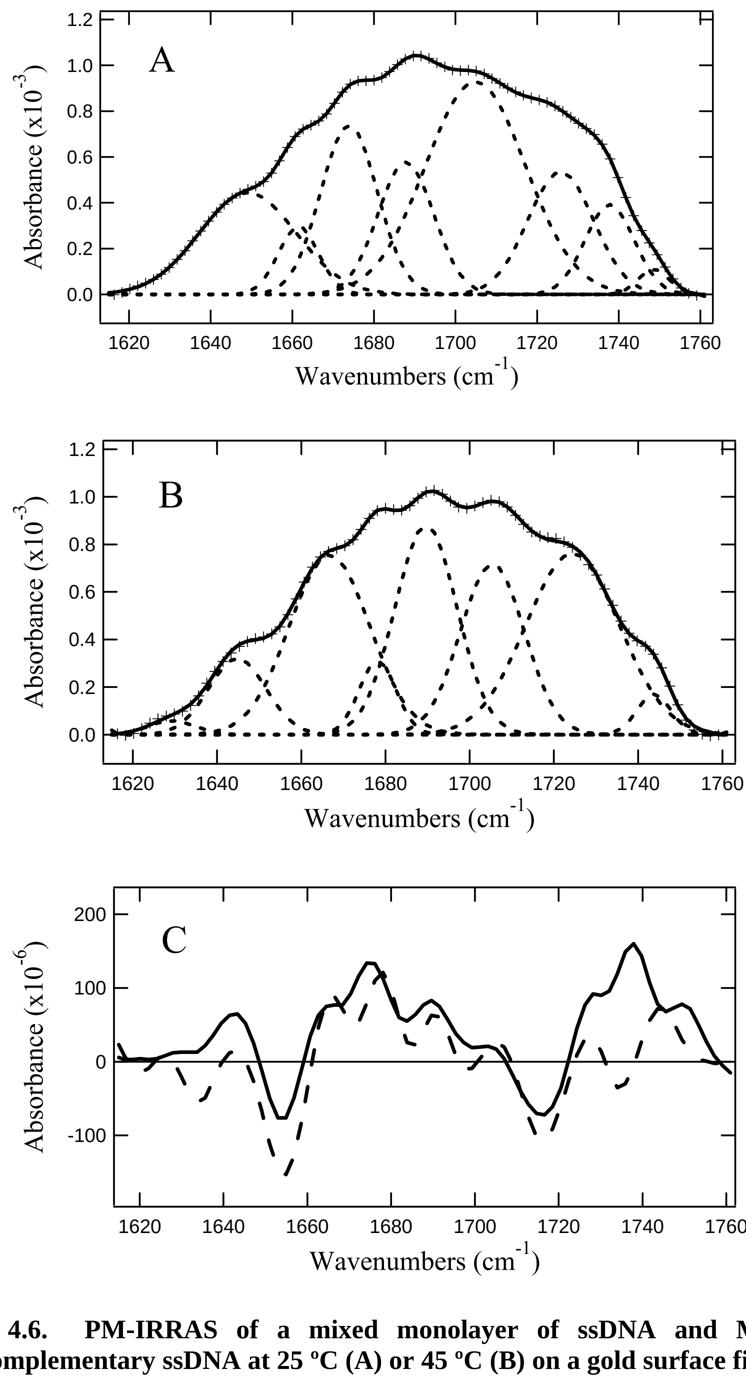


**Figure 4.6. PM-IRRAS of a mixed monolayer of ssDNA and MCH hybridized with the complementary ssDNA at 25 ºC (A) or 45 ºC (B) on a gold surface fitted to Gaussian line shapes and (C) is the difference spectra obtained by subtracting the ssDNA spectra from the dsDNA**

**spectra. The solid and dashed lines correspond to the 25 ºC and 45 ºC difference spectra, respectively.**

The distinction between ssDNA and dsDNA occurs in the 1550-1750 $cm^{-1}$ region as shown in Figure 4.6 and is due to the H-bonds formed during base pair formation in dsDNA relative to ssDNA. This H-bonding spectral region shows the dsDNA infrared signatures at 1674 $cm^{-1}$ and 1678 $cm^{-1}$ for dsDNA at 25 °C and 45 °C respectively with the decrease of the bands at 1655 $cm^{-1}$ and 1717 $cm^{-1}$ relative to the ssDNA spectrum. These IR modes are due to $NH_{(2)}$ bending and C=O stretching modes, respectively that are directly affected by hybridization due to the Watson-Crick H-bonds formed in dsDNA that are absent in ssDNA. These hydrogen bonds result in a blue shift in the N-H and $N\text{-}H_2$ bending motions and a red shift in the carbonyl stretching motions resulting in a dsDNA IR signature. [24] PM-IRRAS also allows a comparison of hybridization at two different temperatures to be made. Figures 4.6A and 4.6B show that the IR bands for dsDNA have different features for surface hybridization at 25 °C or 45 °C. These differences are possibly due to varying amounts of dsDNA on the surface because of differing efficiencies of surface DNA hybridization at the these two temperatures. However, the surface selection rules [28] prevent the hybridization yields from being determined by PM-IRRAS because the orientations of ssDNA and dsDNA are not the same. Moreover, at the present time, we do not have sufficient information to make a model of the conformation of either ssDNA or dsDNA at the surface.

The origin of the observed infrared spectroscopic differences between ssDNA and dsDNA was confirmed using density functional theory (DFT) as shown in Figure 4.7. The models used for the DFT calculations were the individual nucleotides and the corresponding nucleotide base pairs.

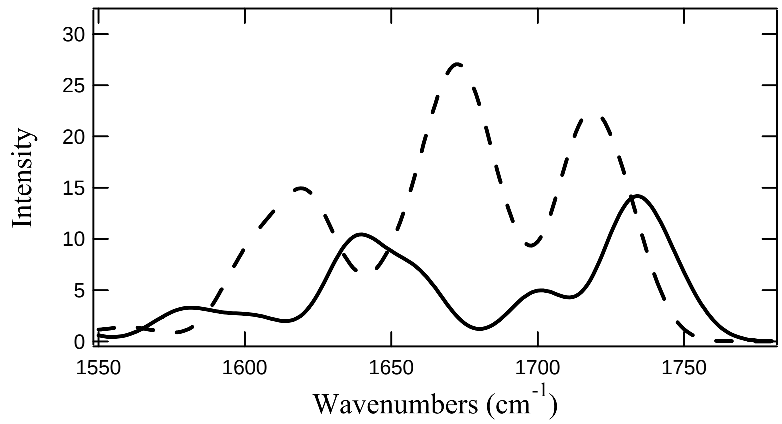


**Figure 4.7. DFT calculated infrared spectra of ssDNA (solid) and dsDNA (dashed) using a weighted average of the DFT calculated infrared spectra of the individual and nucleotides along with the corresponding nucleotide base pairs according to the experimental DNA sequence used in the experiments.**

The structures were first optimized and then a vibrational frequency calculation was performed on each of the DFT optimized structures of the DNA nucleotides and nucleotide base pairs. These calculated frequencies were plotted using a Gaussian width of 10 $cm^{-1}$ and a weighted average of the nucleotides or nucleotide base pairs spectra were used to generate the ssDNA and dsDNA spectra of the P1 oligo used in the DNA experiments on gold surfaces shown above. The calculated dsDNA spectrum exhibited a dsDNA infrared signature that was not present in the calculated ssDNA spectrum. The position of dsDNA infrared signature was calculated to be at 1673 $cm^{-1}$. This calculated dsDNA infrared signature agrees well with the experimentally determined dsDNA IR signature on both a gold surface as shown in Figure 4.6 and in solution (data not shown). These DFT calculations show that the modes in the 1550-1780 $cm^{-1}$ region are primarily due to $NH_{(2)}$ bending and carbonyl stretching motions in the nucleobases. These functional groups are involved in Watson-Crick hydrogen bonds upon base pair formation in dsDNA that are absent in ssDNA. These hydrogen bonds therefore shift the frequencies of these motions in dsDNA relative to ssDNA resulting in a calculated dsDNA IR signature. For instance, the $NH_2$ bending motion and the carbonyl stretching frequency of 2'-deoxyadenosine-5'-monophosphate and 2'-deoxythymidine-5'-monophosphate shift from 1638 $cm^{-1}$ and 1700 $cm^{-1}$ to 1658 $cm^{-1}$ and 1674 $cm^{-1}$, respectively upon going from the individual nucleotides to the AT base pair due to the hydrogen bond between these two moieties (data not shown). Shifts in vibrational frequencies due to hydrogen bonds have been previously reported before in the well-known case of the gas phase water OH bending mode shifting from 1595 $cm^{-1}$ to 1638 $cm^{-1}$ in liquid water due to the formation of hydrogen bonds. [29 30-32]

### 4.4.2.4 Atomic Force Microscopy (AFM).

To confirm that DNA hybridization occurs on the gold surface in addition to ssDNA probe desorption, AFM was used to quantitate specific DNA hybridization on the surface by labeling the target ssDNA strand with a colloidal 10 nm gold nanoparticle. Figure 4.8 shows the AFM image of MCH/ssDNA monolayer upon hybridization with its complimentary (A) and non-complimentary (B) ssDNA target labeled with a 10 nm gold colloid.

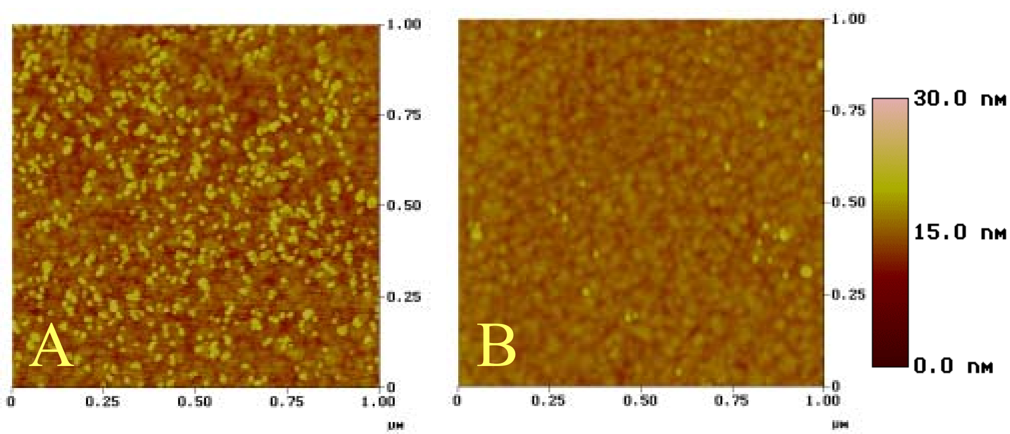


**Figure 4.8. AFM image of Gold substrate upon hybridization of ssDNA/MCH monolayer with its compliment target labeled with 10 nm gold colloid (A) and with a non-compliment (B) at 6 nM target concentration.**

The surface coverage of dsDNA through the hybridization between complimentary DNA strands was found to be $8x10^{10}$ particles/$cm^2$ by counting the number of gold nanoparticles present on the surface while only minimal non-specific binding to the surface was detected due to the number of gold nanoparticles found when the MCH/ssDNA modified surface was exposed to the non-complimentary ssDNA.

## 4.5 Discussion

This study was focused on characterizing DNA-modified gold substrates and optimizing the conditions for hybridization of DNA. However, probe ssDNA strand loss from the gold surface was found to compete with surface DNA hybridization. Therefore, the thermal desorption of the probe ssDNA and the formation of dsDNA on the surface through DNA hybridization was investigated.

At low coverages of ssDNA ($4 \times 10^{12}$ strands/$cm^2$) XPS shows an increase in the nitrogen (1s) signals for dsDNA relative to ssDNA on the gold surface indicative of DNA hybridization (data not shown). On the other hand, at high ssDNA coverages ($> 2x10^{13}$ strands/$cm^2$) both XPS and chronocoulometry show a loss of ssDNA from the surface even at 25 ºC. AFM and PM-IRRAS independently confirm that DNA hybridization also occurs at the surface at elevated temperatures.

In order to determine the surface coverage AFM, fluorescence and electrochemistry were utilized. Though electrochemical methods allow the determination of the DNA surface coverage ($\Gamma_0$=1.2(±1.1)$x10^{13}$ molecules/$cm^2$), there is a large sample-to-sample variation in chronocoulometry measurements that has prevented accurate measurement of the hybridization yield. Also loss of ssDNA probes strands from the gold surface and conformational changes in dsDNA upon hybridization reduces the signal in chronocoulometric measurements preventing its effective use in quantification of dsDNA on the surface. In practice, the observed differences in the chronocoulometry signal due to formation of dsDNA appear small under all conditions studied. This is confirmed to be due to a hybridization yield of less than 50% combined with strand loss.

Methods that involve labeling of the oligonucleotide (either using a gold nanoparticle or a fluorescein molecule) are consistent in showing greater surface density as the concentration of the ssDNA molecules with the label is increased; however, they give consistently lower estimates for the surface coverage than chronocoulometry. While chronocoulometry provides the best absolute values for surface coverage, the nanoparticle and fluorescent labeling methods provide separate methods to verify the relative coverage and hybridization yield under varying conditions of temperature and strand concentration. AFM shows there is definite hybridization and the surface coverage by gold nanoparticle count is $8 \times 10^{10}$ particles/cm$^2$. The surface coverage by colloidal labeling of target is consistently lower in comparison to chronocoulometry. This lower surface coverage is likely due to the size of the colloidal label on the target strand that covers multiple probe strands on the surface. Furthermore, the ionic atmosphere of the colloid repels neighboring colloids resulting in a greater separation distance than the nominal sphere diameter of the colloid.

The fluorescence measurements require the full displacement of the DNA labeled with the fluorescent tag on the surface since the gold surface quenches the fluorescence of fluorescently labeled oligonucleotides.[27] However experimental evidence shows that complete removal of the labeled DNA from the surface is not possible (as shown from the comparison to the electrochemical data) through the procedures implemented here, resulting in consistently low surface coverage measurements by fluorescence. Nonetheless, Figure 4.4 shows that the same trend is observed by fluorescence as by chronocoulometry. The ssDNA strand concentration decreases with increasing temperature. Thus, a variety of methods show strand loss of ssDNA at elevated temperature.

In addition to this strand loss, we find additional strand loss can occur during hybridization. The hybridization temperature is a complicating factor in DNA hybridization experiments on surfaces. To improve DNA hybridization yield, the temperature needs to be raised above room temperature. However, at higher temperatures increased hybridization yields compete with desorption of the thiolated dsDNA probe from the surface. Figures 4.2, 4.3 and 4.4 show that desorption occurs above room temperature and the hybridization yield measurements by chronocoulometry and XPS are complicated by the desorption process. PM-IRRAS confirmed formation of dsDNA on the gold surface combined with desorption of probes from surface at temperatures above 25 $^{o}$C.

The anomalous data at 65 $^{o}$C in both XPS and chronocoulometry measurements are reproducible and have no explanation at the present time. The structure of ssDNA on a gold surface is not known and it is possible that an annealing process (e.g. binding of the nucleobases rather than thiol to the gold surface) could actually permit a higher surface coverage (less ssDNA desorption) at 65 $^{o}$C as compared to the lower temperatures studied. At 85 $^{o}$C the strand loss due to the equilibrium with disulfide would compete with the annealing process and result in a significantly smaller surface coverage.

The mechanism of desorption is due to the equilibrium between alkane thiols on the surface and disulfides in solution, 2 RS → R-S-S-R. [13,33,34] Since both ssDNA and dsDNA are polyelectrolytes they have significant solubility in water and can drive this equilibrium even further towards the right. The use of multipoint binders can be used to overcome this inherent disadvantage of the alkane thiol-gold surface[35,36].

## 4.6 Conclusions

DNA modified planar gold substrates were characterized by XPS, chronocoulometry, PM-IRRAS, fluorescence and AFM. The surface coverage of ssDNA was found to be as high as ~2 x $10^{13}$ ssDNA molecules/$cm^2$ by chronocoulometry, although a consistent value of 4(±1) x $10^{12}$ ssDNA molecules/$cm^2$ was repeatedly observed in tens of studies. However the XPS N 1s peak area showed a decrease in the dsDNA samples hybridized at both 25 ºC and 45 ºC suggestive of ssDNA desorption at both temperatures. PM-IRRAS detected surface DNA hybridization at both of these temperatures by a dsDNA IR signature at ~1678 $cm^{-1}$. As verified by DFT calculations, this mode is the result of $N\text{-}H_{(2)}$ bending and C=O stretching motions in the DNA nucleotides involved in hydrogen bonding in the DNA base pairs. AFM also confirmed the formation of dsDNA on the gold surfaces by surface DNA hybridization through colloidal gold nanoparticle labeling of the target ssDNA.

Chronocoulometry and fluorescence showed that thermal desorption of the 5' $C_6$-SH modified ssDNA on gold surfaces begins at temperatures just above room temperature. The thermal desorption of ssDNA from these gold surfaces was found to increase linearly with increasing temperature with an anomalously low thermal desorption at 65 $^{o}$C. These studies clearly demonstrate the inherent problem in performing DNA hybridization on self-assembled monolayers. Although DNA hybridization is optimal at ~ 15 $^{o}$C below the melt temperature of the oligonucleotide, thermal desorption of alkane thiols is a competing process that can affect the hybridization yield even at 25$^{o}$C. These observations underlie the search in certain groups for more robust attachment using dithiols and trithiols as well as the approach of using polyadenosine. [35,36]

## Acknowledgements

Support and computational facilities were provided by the North Carolina Supercomputing Center. S.F. and D.F. gratefully acknowledge support by Applied Biosystems, Inc. D.F. gratefully acknowledges support by a grant from the Arnold and Mabel Beckman Foundation.

## References

(1) Southern, E. M.; Casegreen, S. C.; Elder, J. K.; Johnson, M.; Mir, K. U.; Wang, L.; Williams, J. C. *Nuc. Acids Res.* **1994**, *22*, 1368-1373.
(2) Pease, A. C.; Solas, D.; Sullivan, E. J.; Cronin, M. T.; Holmes, C. P.; Fodor, S. P. A. *P.N.A.S. USA* **1994**, *91*, 5022-5026.
(3) Odonnell, M. J.; Tang, K.; Koster, H.; Smith, C. L.; Cantor, C. R. *Anal. Chem.* **1997**, *69*, 2438-2443.
(4) Steel, A. B.; Herne, T. M.; Tarlov, M. J. *Anal. Chem.* **1998**, *70*, 4670-4677.
(5) Taton, T. A.; Mirkin, C. A.; Letsinger, R. L. *Science* **2000**, *289*, 1757-1760.
(6) Bai, X. P.; Li, Z. M.; Jockusch, S.; Turro, N. J.; Ju, J. Y. *P.N.A.S. USA* **2003**, *100*, 409-413.
(7) Armistead, P. M.; Thorp, H. H. *Anal. Chem.* **2001**, *73*, 558-564.

(8) Lowe, L. B.; Brewer, S. H.; Kramer, S.; Fuierer, R. R.; Qian, G. G.; Agbasi-Porter, C. O.; Moses, S.; Franzen, S.; Feldheim, D. L. *J. Am. Chem. Soc.* **2003**, *125*, 14258-14259.
(9) Herne, T. M.; Tarlov, M. J. *J. Am. Chem. Soc.* **1997**, *119*, 8916-8920.
(10) Steel, A. B.; Herne, T. M.; Tarlov, M. J. *Bioconj. Chem.* **1999**, *10*, 419-423.
(11) Thiel, A. J.; Frutos, A. G.; Jordan, C. E.; Corn, R. M.; Smith, L. M. *Anal. Chem.* **1997**, *69*, 4948-4956.
(12) Sauthier, M.; Carroll, R.; Gorman, C.; Franzen, S. *Langmuir* **2002**, *18*, 1825-1830.
(13) Biebuyck, H. A.; Bian, C. D.; Whitesides, G. M. *Langmuir* **1994**, *10*, 1825-1831.
(14) Fodor, S. P. A.; Read, J. L.; Pirrung, M. C.; Stryer, L.; Lu, A. T.; Solas, D. *Science* **1991**, *251*, 767-773.
(15) Lockhart, D. J.; Winzeler, E. A. *Nature* **2000**, *405*, 827-836.
(16) Bulyk, M. L.; Gentalen, E.; Lockhart, D. J.; Church, G. M. *Nature Biotech.* **1999**, *17*, 573-577.
(17) Chee, M.; Yang, R.; Hubbell, E.; Berno, A.; Huang, X. C.; Stern, D.; Winkler, J.; Lockhart, D. J.; Morris, M. S.; Fodor, S. P. A. *Science* **1996**, *274*, 610-614.
(18) Jordan, C. E.; Frutos, A. G.; Thiel, A. J.; Corn, R. M. *Anal. Chem.* **1997**, *69*, 4939-4947.
(19) Lee, H. J.; Goodrich, T. T.; Corn, R. M. *Anal. Chem.* **2001**, *73*, 5525-5531.
(20) Li, M.; Lee, H. J.; Condon, A. E.; Corn, R. M. *Langmuir* **2002**, *18*, 805-812.
(21) Nelson, B. P.; Grimsrud, T. E.; Liles, M. R.; Goodman, R. M.; Corn, R. M. *Anal. Chem.* **2001**, *73*, 1-7.
(22) Brockman, J. M.; Frutos, A. G.; Corn, R. M. *J. Am. Chem. Soc.* **1999**, *121*, 8044-8051.
(23) Esch, M. B.; Locascio, L. E.; Tarlov, M. J.; Durst, R. A. *Anal. Chem.* **2001**, *73*, 2952-2958.
(24) Brewer, S. H.; Anthireya, S. J.; Lappi, S. E.; Drapcho, D. L.; Franzen, S. *Langmuir* **2002**, *18*, 4460-4464.
(25) Delley, B. *J. Phys. Chem.* **1990**, *92*, 508-517.
(26) Perdew, J. P.; Chevary, J. A.; Vosko, S. H.; Jackson, K. A.; Pederson, M. R.; Singh, D. J.; Fiolhais, C. *Phys. Rev. B* **1992**, *46*, 6671-6687.
(27) Demers, L. M.; Mirkin, C. A.; Mucic, R. C.; Reynolds, R. A.; Letsinger, R. L.; Elghanian, R.; Viswanadham, G. *Anal. Chem.* **2000**, *72*, 5535-5541.
(28) Parikh, A.; Allara, D. *J. Chem. Phys.* **1992**, *96*, 927-944.
(29) Herzberg, G. *Infrared and Raman Spectra of polyatomic molecules*; D. Van Nostrand Company, Inc, 1945.
(30) Marechal, Y. *J. Phys. Chem.* **1993**, *97*, 2846-2850.
(31) Marechal, Y. *J. Mol. Struct.* **1994**, *322*, 105-111.
(32) Senior, W. A.; Thompson, W. K. *Nature* **1965**, *205*, 170.
(33) Lees, W. J.; Whitesides, G. M. *J. Org. Chem.* **1993**, *58*, 642-647.
(34) Houk, J.; Whitesides, G. M. *J. Am. Chem. Soc.* **1987**, *109*, 6825-6836.
(35) Garg, N.; Lee, T. *Langmuir* **1998**, *14*, 3815-3819.
(36) Tan, Y.; Li, Y.; Zhu, D. *Langmuir* **2002**, *18*, 3392-3395.

## *Tables*

**Table 4.1. XPS N 1s peak positions and areas.**

| DNA on Gold | Peak Position N 1s (eV) | Area of N 1s (Arb. units) |
|---|---|---|
| MCH/probe ssDNA | 400.2 | 22675 |
| MCH/ssDNA + target ssDNA | 400.3 (25 ºC)* | 18645 (25 ºC)* |
| | 400.2 (45 ºC)* | 13802 (45 ºC)* |

* Hybridization temperature.

**Table 4.2. Gaussian fits to the PM-IRRAS spectra of ssDNA and dsDNA on a gold surface.**

| | | ssDNA | dsDNA (25 ºC)* | dsDNA (45 ºC)* |
|---|---|---|---|---|
| Gaussian 1 | Amplitude | 0.0057 | 0.0132 | 0.0008 |
| | Position ($cm^{-1}$) | 1641.6 | 1649.1 | 1629.2 |
| | Width | 9.09211 | 11.83 | 5.56 |
| Gaussian 2 | Amplitude | 0.0048 | 0.0036 | 0.0055 |
| | Position ($cm^{-1}$) | 1654.6 | 1661.5 | 1644.8 |
| | Width | 6.37838 | 4.89 | 6.81 |
| Gaussian 3 | Amplitude | 0.0124 | 0.0129 | 0.0180 |
| | Position ($cm^{-1}$) | 1667.8 | 1673.9 | 1666.7 |
| | Width | 9.78693 | 6.93 | 9.52 |
| Gaussian 4 | Amplitude | 0.0259 | 0.0099 | 0.0034 |
| | Position ($cm^{-1}$) | 1689.8 | 1687.8 | 1678.1 |
| | Width | 11.9829 | 6.86 | 4.35 |
| Gaussian 5 | Amplitude | 0.0166 | 0.0285 | 0.0163 |
| | Position ($cm^{-1}$) | 1711.2 | 1704.9 | 1689.6 |
| | Width | 9.78743 | 12.24 | 7.39 |
| Gaussian 6 | Amplitude | 0.0077 | 0.0108 | 0.0136 |
| | Position ($cm^{-1}$) | 1722.9 | 1725.8 | 1705.4 |
| | Width | 6.95 | 8.06 | 7.58 |
| Gaussian 7 | Amplitude | 0.0050 | 0.0059 | 0.0212 |
| | Position ($cm^{-1}$) | 1734.0 | 1737.8 | 1724.4 |
| | Width | 5.02 | 6.02 | 11.09 |
| Gaussian 8 | Amplitude | 0.0022 | 0.0010 | 0.0017 |
| | Position ($cm^{-1}$) | 1743.8 | 1748.6 | 1743.8 |
| | Width | 4.41 | 3.76 | 4.00 |

* Hybridization temperature.

**Table 4.3 N 1s XPS peak positions and areas.**

| Temperature at which MCH/ssDNA adlayer was heated in 1XSSC (ºC) | Peak Position N 1s (eV) | N 1s Area (Arb. units) |
|---|---|---|
| 25 | 399.3 | 12037 |
| 45 | 399.4 | 11535 |
| 65 | 399.3 | 11942 |
| 85 | 399.4 | 10569 |

# CHAPTER 5

# Detection of DNA hybridization on Indium Tin Oxide Surfaces

## Abstract

Indium tin oxide (ITO) surfaces were modified with ssDNA by coupling oligonucleotides to a monolayer of 12-phosphonododecanoic acid (12-PDA) on ITO surfaces. This coupling involved the formation of an amide bond between the carboxylic acid moiety of 12-PDA to the amine group of a 5'-aminopropyl-labeled single strand of DNA. The self-assembled monolayer of 12-PDA and surface-attached oligonucleotides were characterized by X-ray photoelectron and reflectance FTIR spectroscopy. Detection of selective surface DNA hybridization was achieved by labeling the target ssDNA with gold nanoparticles. The presence of gold nanoparticles was probed using X-ray photoelectron spectroscopy, stripping voltammetry, atomic force microscopy, thermography, photoelectrochemistry (chronoamperometry) and cyclic voltammetry (CV). CV was used to successfully detect DNA hybridization for nanoparticle concentrations as low as 10 pM when using the gold nanoparticles bound to an ITO electrode as catalysts for the electrochemical oxidation of $FeCl_2$.


## 5.1 Introduction

The detection of surface DNA hybridization continues to be an important area of research for applications in detection of messenger RNA levels in cells and genomic analysis. Various surface attachment and detection strategies have been investigated to determine the optimal system for detecting surface DNA hybridization. Gold [1] and glass [2,3] substrates have been utilized in several of these systems due to the ability to form self-assembled monolayers on these surfaces with thiol or chloro- or alkoxysilane containing molecules, [4] respectively. These systems have shown the detection of selective DNA hybridization through a variety of detection techniques including fluorescence, [5-8] surface plasmon resonance (SPR), [9,10] electrochemistry, [11-13] FTIR spectroscopy, [14] X-ray photoelectron spectroscopy (XPS) [1] and through the labeling with nanoparticles. [15-17]

In this study, indium tin oxide (ITO) thin films were investigated to develop a surface DNA modification procedure to be used for the subsequent detection of DNA hybridization. The electronic and optical properties of ITO have spurred interest in the formation of adlayers on ITO [18-23] and technologies have been developed for the detection of DNA or PNA on ITO. [24-26] ITO offers unique properties that allow for various detection strategies. For instance, ITO thin films are transparent in the visible region and reflective in the infrared region. [27-32] ITO electrodes also have the desired ability to sustain relatively high potentials needed for many applications including direct or mediated oxidation of guanosine nucleotides [24] or metal stripping voltammetry using nanoparticle labels to name two. The detection strategies employed in this study involve the detection of gold-nanoparticle-labeled target single-stranded DNA (ssDNA). [33] The formation of self-assembled monolayers and the coupling of ssDNA to those monolayers on ITO thin films were confirmed by XPS, reflectance FTIR spectroscopy and chronocoulometry while the gold nanoparticle / target ssDNA conjugates were detected on the ITO surface by XPS, stripping voltammetry, atomic force microscopy (AFM), thermography, photoelectrochemistry (chronoamperometry) and cyclic voltammetry (CV).

## *5.2 Methods and Materials*

### 5.2.1 ssDNA modification of ITO.

The Scheme 1 outlines the strategy employed in the modification of indium tin oxide (ITO) (Delta Technologies, Ltd.) surfaces with ssDNA. The ITO thin films were comprised of 90% indium oxide and 10% tin oxide, had a nominal thickness of 1,500 Å and a sheet resistance of 8-12 Ω. Initially a monolayer of 12-phosphonododecanoic acid (12-PDA) (Xanthon, Inc.) (10mM in 50/50 DMSO/18 MΩ cm $H_2O$ for 16 hours) was formed on the ITO surface (cleaned 20 minutes with UV/$O_3$ (UVO-cleaner (UVO-60), model number 42, Jelight Company, Inc)). The carboxylic acid functional group of 12-PDA was activated by 1-ethyl-3-(3-dimethylaminopropyl)carbodiimide hydrochloride (EDC) (Sigma-Aldrich) and reacted with the primary amine of a 5' modified $H_2N$-$(CH_2)_3$ ssDNA (5'$H_2N$-$(CH_2)_3$ modified 5'-GTGAGCGGATAATCCTGGTT-3') (Applied Biosystems, Inc.) to form an amide bond between the 12-PDA and the 5' modified $H_2N$-$(CH_2)_3$ ssDNA. The coupling conditions were 1 μM 5' modified $H_2N$-$(CH_2)_3$ ssDNA and 200 mM EDC for 4 hours in a 0.1 M MES (2-(N-morpholino)ethane sulfonic acid) buffer at pH 5 with 0.25 M NaCl. The surface was then rinsed with 18 MΩ cm $H_2O$ (BARNSTEAD E-PURE) and dried with $N_2$ gas.

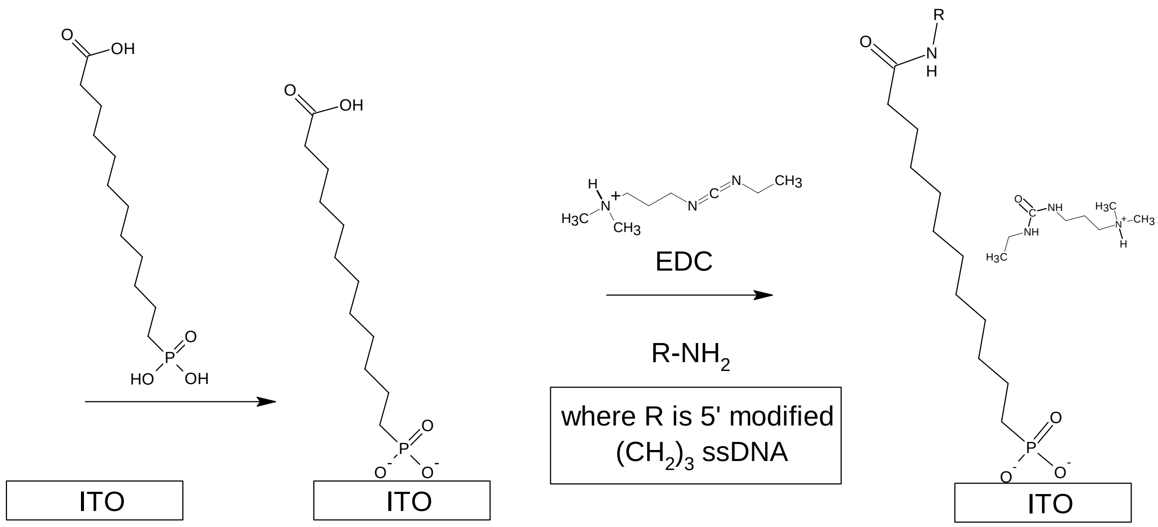


**Scheme 5.1. Modification of ITO with single stranded DNA through the formation of an amide bond between the carboxylic acid functional group of a monolayer of 12-phosphonododecanoic acid with the primary amine of 5' modified $H_2N(CH_2)_3$ ssDNA.**

### 5.2.2 Preparation of the Gold Nanoparticle / Oligonucleotide Conjugates.

The gold nanoparticle conjugates were synthesized by the attachment of 5' thiol modified ssDNA. The complementary ssDNA target strand used in the hybridization experiments was 5'-$HS(CH_2)_6$ modified 5'-AACCAGGATTATCCGCTCAC-3' while the non-complementary ssDNA target strand was 5'-$HS(CH_2)_6$ modified 5'-GTGAGCGGATAATCCTGGTT-3'. Gold nanoparticles (10 nm diameter) coated with bis(*p*-sulfonatophenyl)phenylphosphine dihydrate dipotassium salt (BSPP) were synthesized by a literature procedure. [34] Briefly, 10 nm citrate coated Au colloids (Ted Pellar) were stirred with an excess of BSPP at room temperature overnight. To slightly aggregate the nanoparticles 50 mg of NaCl was added progressively until the color of the colloidal suspension changed from burgundy to a slightly purplish color. The sample was centrifuged to pellet the particles and the supernatant was removed. Afterwards the pellet was re-suspended in a 250 mg/L solution of BSPP. Methanol was added drop wise until the color of the particles turned from a burgundy red to a purplish color again. The colloidal solution was centrifuged and the supernatant was discarded. The gold nanoparticles were finally re-dissolved in the BSPP solution and stored at 4 $^{o}$C.

For the preparation of the gold nanoparticle / ssDNA conjugates, a 1:100 ratio of gold nanoparticles to ssDNA was stirred at room temperature overnight. In order to remove non-reacted ssDNA, the solution was centrifuged at 14,000 rpm for 30 min and the precipitate was re-suspended into 1xSSC (saline sodium citrate) buffer. This procedure was performed twice and resulted in approximately 5 – 6 ssDNA strands per gold nanoparticle determined by fluorescence (data not shown). The final concentration conjugate solution had a final concentration of 3.7 nM gold nanoparticles as determined from the absorbance of the plasmon band of the gold nanoparticles using an extinction coefficient of $8.9 \times 10^{7}$ $M^{-1}cm^{-1}$.

### 5.2.3 DNA Hybridization Conditions.

The DNA hybridization was carried out either at 37 $^{o}$C for 19 hrs in a shaking incubator or by keeping the hybridization solution for 1 hour at 45 °C and then allowing the solution to gradually cool to room temperature overnight. The hybridization conditions were varied to study its effect on the efficiency of hybridization and the limit of detection. The concentrations of the gold nanoparticle / ssDNA conjugate solutions used in this study were in the range of 1 nM to 1 pM of the gold nanoparticle.

### 5.2.4 X-ray Photoelectron Spectroscopy (XPS).

XPS spectra were recorded on a Riber LAS 2000 Surface Analysis System equipped with a cylindrical mirror analyzer (CMA) and a MAC2 analyzer with Mg Kα X-rays (model CX 700 (Riber source) (hν = 1253.6 eV). The elemental scans had a resolution of

1.0 eV and were the result of 5 scans. XPS spectra were smoothed using a 9 point (second order) Savitzky-Golay algorithm, baseline corrected and the peaks were fitted using Gaussian line shapes.

### 5.2.5 Infrared Reflection Absorption Spectroscopy (IRRAS).

The reflectance FTIR spectra were recorded using a Spectra-Tech grazing angle reflectance attachment in a Nicolet Magna-IR 860 FTIR spectrometer. The angle of incidence used was 80 degrees. An infrared polarizer was used to obtain p- (vertically) polarized light. The spectra of the monolayers deposited on the ITO surfaces were obtained by taking a ratio of the single beam spectra of the deposited material on an ITO surface to one of a clean ITO surface. The rotational lines from gaseous water were subtracted from these spectra. The FTIR spectrometer was equipped with a liquid nitrogen cooled MCT/A detector and the spectra were recorded at a resolution of 2 $cm^{-1}$ with a spectral range of 900 - 4000 $cm^{-1}$. All IR spectra were the result of 256 scans and were recorded at room temperature.

### 5.2.6 Density Functional Theory (DFT) Calculations.

The geometry optimization and vibrational frequency calculations of the various nucleosides for comparison with IR spectra were carried using density functional theory (DFT) using DMol3 (Accelrys, Inc.). [35]as described elsewhere [14].

### 5.2.7 Electrochemistry.

The electrochemical measurements were performed on an EG & G Princeton Applied Research instrument (Potentiostat Model 273A). The electrochemical setup consisted of a three-electrode cell consisting of $Ag_{(s)}/AgCl$ as the reference electrode and a Pt wire as the counter electrode. The area of the working electrode was 0.28 $cm^2$.

Chronocoulometry was done in 10 mM Tris buffer (pH 7.1) in the presence and absence of 50 μM $[Ru(NH_3)_6]^{3+}$ after purging it thoroughly with argon gas for 10 min. The surface density of probe ssDNA can be calculated from the chronocoulometric measurements using the assumption that one $[Ru(NH_3)_6]^{3+}$ molecule binds to the anionic phosphodiester backbone of DNA for every three bases [12] The integrated Cottrell equation, which expresses charge Q as a function of time, can be used to calculate the surface excess term as shown in Eqn. 2:

$$Q = \frac{2nFAD_0^{1/2}C_0^*}{\pi^{1/2}}t^{1/2} + Q_{\mathrm{dl}} + nFA\Gamma_0 \qquad (5.1)$$

where n is the number of electrons per molecule for reduction, $F$ is the Faraday constant (C/equiv), $A$ the electrode area ($cm^2$), $D_0$ the diffusion coefficient ($cm^2$/s), $C_0^*$ bulk concentration (mol/$cm^2$), $Q_{dl}$ the capacitive charge (C) and $nFA\Gamma_0$ the charge from the reduction of $\Gamma_0$ (mol/$cm^2$) of adsorbed $[Ru(NH_3)_6]^{3+}$. The surface excess term $\Gamma_0$ denotes the amount of redox marker confined at the surface of the electrode. The difference between the chronocoulometric intercepts at time zero from the experiments performed under identical conditions with and without the redox marker yields the surface term. The surface density on the electrode surface can be calculated from this term using the relation in Eqn. 3:

$$\Gamma_{\mathrm{DNA}} = \Gamma_0 (z/m)(N_A) \qquad (5.2)$$

where $\Gamma_{DNA}$ is the surface coverage of DNA, m is the number of bases in the probe ssDNA, z is the charge of the redox molecule and $N_A$ is Avogadro's number.The photoelectrochemical measurements were performed in a custom electrochemical cell allowing for the direct illumination of the electrode surface. The electrolyte was 0.1 M potassium phosphate buffer (pH 7) with 0.05 M EDTA. The change in electrode potential was monitored with chronoamperometry. Therefore the potential was stepped to 0.7 V versus $Ag_{(s)}$/AgCl while the current was monitored as a function of time. Electrochemical oxidation (stripping) of the gold nanoparticles on the ITO surface was performed in 0.5 M KCl at a scan rate of 100 mV/s. The cyclic voltammograms (CV) of the oxidation of $FeCl_2$ (100 mM), catalyzed by the gold nanoparticles were performed at a scan rate of 100 mV/s.

### 5.2.8 Thermographic Measurements.

The modified ITO surfaces were illuminated with 532 nm light from a frequency doubled quasi-CW Nd:YAG laser (Coherent Antares 76-Nd:YAG laser) and the change in surface temperature was monitored by infrared (IR) thermography (Inframetrics 740). The laser beam was focused to approximately 1 mm diameter and the light intensity was adjusted to 1 W.

### 5.2.9 Atomic Force Microscopy (AFM).

The ITO surface modified with ssDNA and hybridized with 10 nm gold nanoparticle labeled complimentary target ssDNA was imaged by Digital Instruments Nanoscope IIIa Scanning Probe Microscope in tapping mode. The AFM images were 1$\mu m^2$ with a height scale of 50 nm.

## *5.3 Results and Discussion*

The focus of this study is the surface attachment of ssDNA probes and the detection of hybridization of DNA using nanoparticle labels on ITO surfaces hence ssDNA modified surfaces are discussed briefly.

### 5.3.1 Characterization of ssDNA modified ITO Surface

ITO substrates were modified with 12-phosphonododecanoic acid (12-PDA) linker molecules such that DNA probes could be attached to the linker to create a ssDNA adlayer. As described in Scheme 1 the phosphonate group binds to the ITO substrate while the carboxylic group is available for binding to the amine terminated DNA probe by EDC coupling. Whether a well ordered monolayer of 12-PDA is formed on ITO substrates or not is dependent on the type of ITO. Variation in intensity of signal was observed when XPS was employed to detect presence of DNA on ITO substrates and surface coverage by chronocoulometry was. The results from XPS, IR and chronocoulometry are discussed in detail in this section.

Figure panels 5.1A and 5.1B show the XPS spectra of In $3d_{5/2,3/2}$ (444.4, 452.0 eV) and Sn $3d_{5/2,3/2}$ (486.5, 494.9 eV), respectively, for bare ITO (solid), ITO modified with a monolayer of 12-phosphonododecanoic acid (short dash) and ITO modified with ssDNA coupled through a monolayer of 12-PDA (long dash).

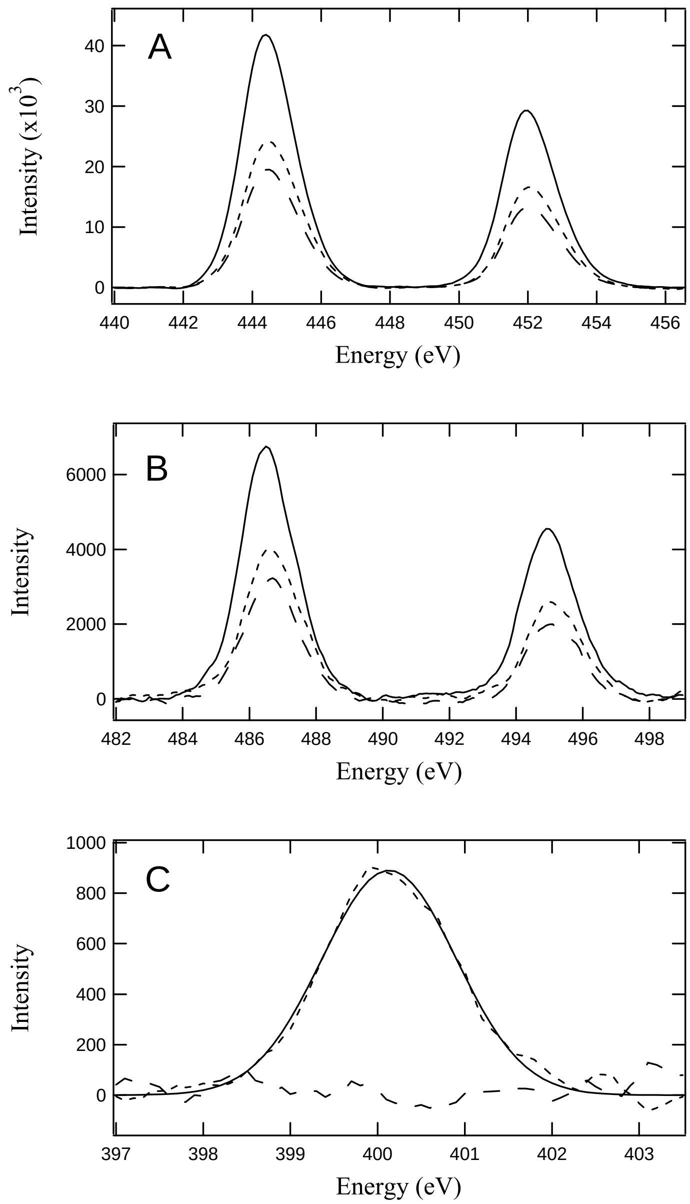


**Figure 5.1. XPS spectra of In 3d$_{5/2,3/2}$ (A) and Sn 3d$_{5/2,3/2}$ (B) for bare ITO (solid), ITO modified with a monolayer of 12-phosphonododecanoic acid (short dash) and ITO modified with ssDNA coupled through a monolayer of 12-phosphonododecanoic acid (long dash). C. XPS N 1s spectra of ITO modified with a monolayer of 12-phosphonododecanoic acid (long dash) and ITO modified with ssDNA coupled through a monolayer of 12-phosphonododecanoic acid (short dash) fitted to a Gaussian line shape (solid).**

These spectra show that the signals from both metals were obscured as the monolayer of 12-PDA was formed on the ITO surface relative to bare ITO. The intensities of indium and tin decreased further as ssDNA was chemically bound to the monolayer of 12-PDA using EDC-coupling. The decrease in XPS intensities with each step in the modification of the surface is consistent with surface modification first with 12-PDA and then with ssDNA. When N and P signals are detected, it indicates the presence of DNA adsorbed on substrates. Figure 5.1C shows N 1s intensity of ITO modified with a monolayer of 12-PDA (long dash), ITO modified with a monolayer of 12-PDA and reacted with EDC and ITO modified with ssDNA coupled through a monolayer of 12-PDA (short dash) fitted to a Gaussian line shape (solid). Though Nitrogen is not present in the 12-PDA modified surface, reaction with EDC introduces traces of Nitrogen in the substrate. A stronger N 1s signal is present in the ssDNA modified surface indicative of successful chemical attachment of ssDNA to the ITO substrate. An increase in the P intensity in the ITO substrate modified with ssDNA in comparison to the 12-PDA modified ITO substrate is observed (data not shown) confirming attachment of DNA probes to the ITO surface through 12-PDA linker.

Figure 5.2 A shows the reflectance FTIR spectra of ITO modified with a monolayer of 12-PDA (solid) coupled to ssDNA (short dashed). The FTIR spectra of the 12-PDA monolayer contains a vibrational mode at 1717 $cm^{-1}$ corresponding to the carbonyl stretch of the carboxylic acid functional group of 12-PDA. [14] However, when the surface is subsequently modified with ssDNA the maximum intensity shifts to 1706 $cm^{-1}$.

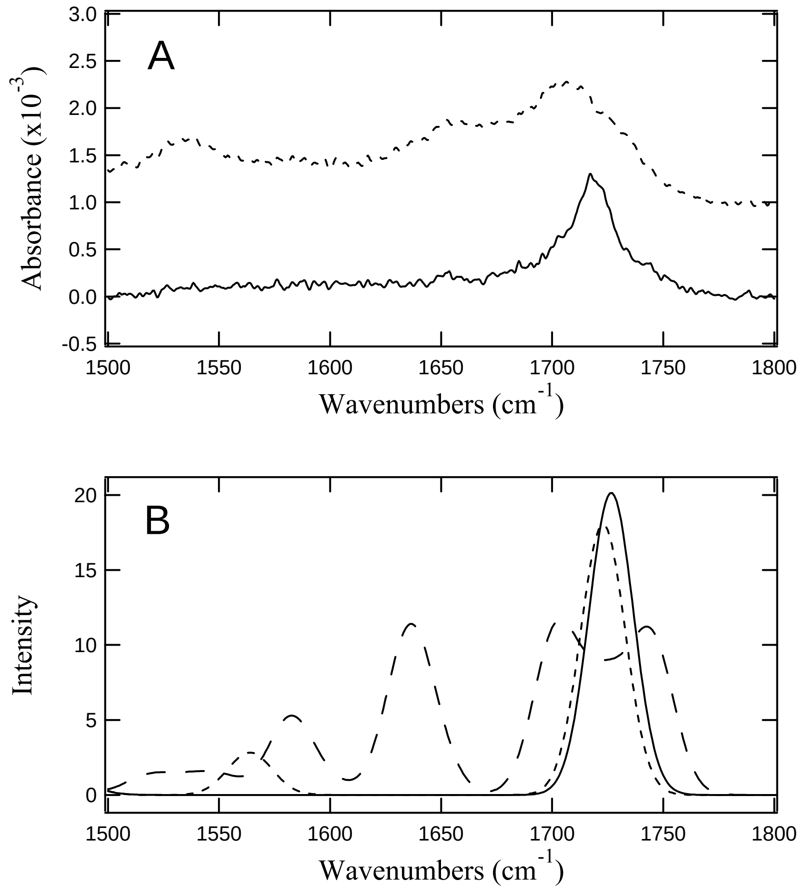


**Figure 5.2. A. Reflectance FTIR spectra of ITO modified with a monolayer of 12-phosphonododecanoic acid (solid) coupled to ssDNA (short dashed) recorded at an incident angle of 80 degrees with p-polarized radiation. B. Density functional theory (DFT) calculated IR spectra of 12-phosphonododecanoic acid (solid), 12-phosphonododecanamide (short dashed) and ssDNA (long dashed) calculated from a weighted average of the calculated IR spectra of the individual nucleosides fit to a Gaussian width of 10 cm$^{-1}$.**

This band is broader due to the presence of DNA and contains multiple vibrational modes in the 1500 – 1800 cm$^{-1}$ region due to $NH_2$ bending and carbonyl stretching modes from the nucleobases in the DNA (with a possible contribution from the N-H bending of the amide bond to 12-PDA). [14] Density functional theory (DFT) calculations were used to model the vibrational spectra. Figure 5.2B shows the DFT calculated IR spectra of 12-phosphonododecanoic acid (solid), 12-phosphonododecanamide (short dashed) and ssDNA (long dashed) calculated from a weighted average of the calculated IR spectra of the individual nucleosides fit to a Gaussian width of (10 $cm^{-1}$). DFT methods calculated the carbonyl stretching frequency of 12-PDA to be 1727 $cm^{-1}$ with a decrease in energy to 1723 $cm^{-1}$ as an amide bond was formed with $NH_3$ as a model system. This shift to lower energy is in qualitative agreement with the experimental results and supports the assignment of the carbonyl stretching vibration and is downshift due to hydrogen bonding. The DFT calculated spectra of the nucleosides (a model for ssDNA) show several modes throughout this region (1500 – 1800 $cm^{-1}$) that are due primarily to $NH_2$ bending and carbonyl stretching motions of the nucleobases, in agreement with experiment.

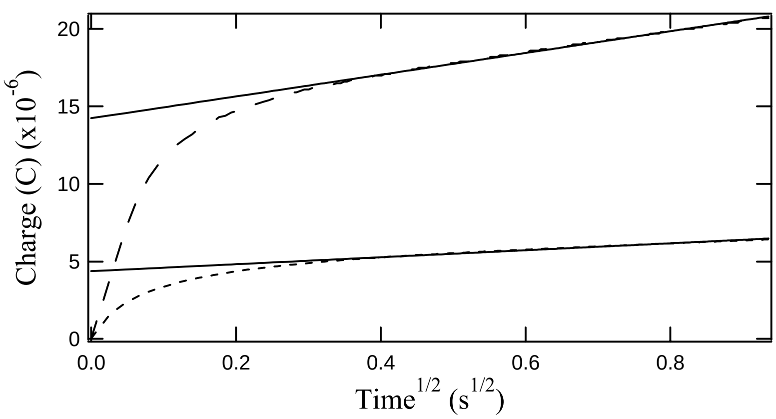


**Figure 5.3. Chronocoulometry of a ssDNA modified ITO surface with (long dash) or without (short dash) $[Ru(NH_3)_6]^{3+}$ in the electrochemical cell.**

The chronocoulometric (CC) response of the indium tin oxide (ITO) substrate modified with probe ssDNA on the surface is seen in Figure 5.3 showing the ITO sample modified with ssDNA in Tris buffer (dotted line) and in the presence of $[Ru(NH_3)_6]^{3+}$ (dashed line) extrapolated (solid line) to time zero. $[Ru(NH_3)_6]^{3+}$ binds to the anionic phosphate backbone of ssDNA on the surface in a ratio of 1:3 and therefore the surface coverage of

DNA can be determined as described previously. [12] The surface coverage of ssDNA on the ITO surface was found to be 2.2(±0.3)x$10^{13}$ molecules/$cm^2$ as calculated from chronocoulometry. This value is approximately an order of magnitude higher than self-assembled monolayers of thiol modified ssDNA and 6-mercapto-1-hexanol on gold surfaces reported under similar conditions. [12] Assuming a diameter of 1 nm for ssDNA, an atomically flat surface and hexagonal close packing the maximum surface coverage would be 7.4x$10^{13}$ molecules/$cm^2$.

### 5.3.2 Characterization of dsDNA modified ITO Surface

Figure 5.4 shows three methods for monitoring dsDNA on ITO surfaces using 10 nm gold-colloid-labeled target strands hybridized to surface attached probe strands. The hybridization was carried out in a solution of 1XSSC with 1 nM of the gold nanoparticle / ssDNA conjugate. The solution was heated to 45 °C for one hour and then allowed to cool overnight.

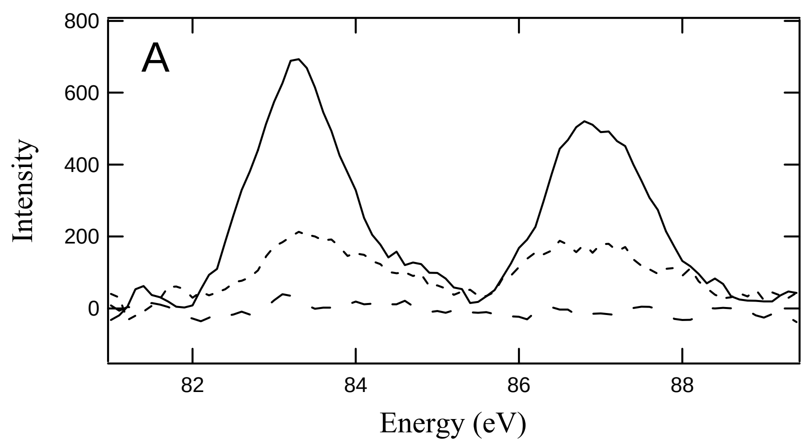

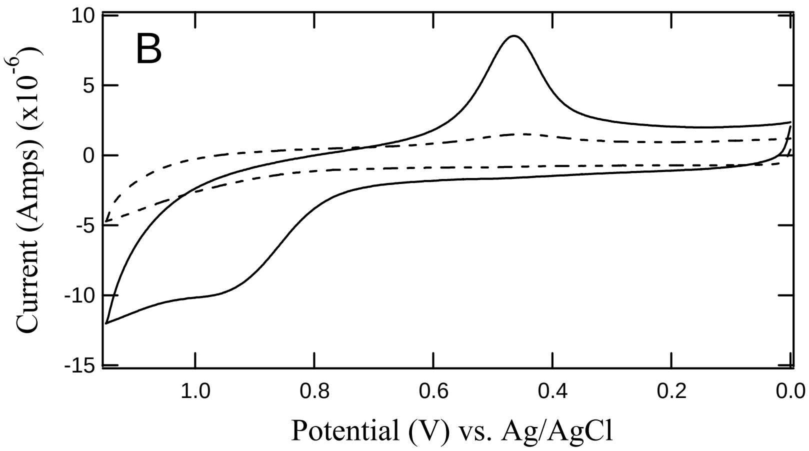


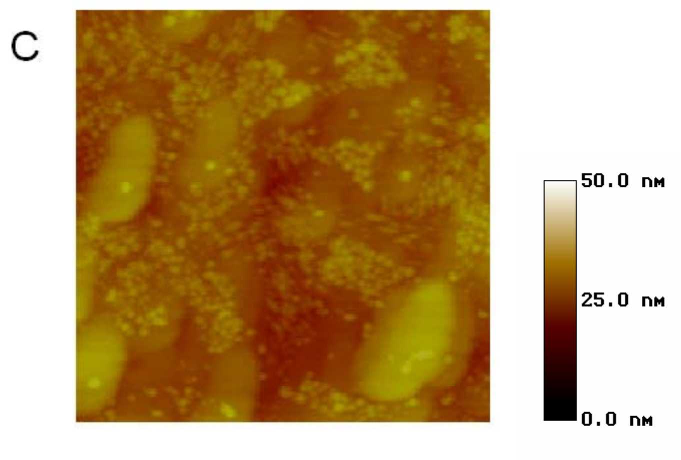


**Figure 5.4 (A) XPS spectra of Au 4$f_{7/2,5/2}$ are shown. (B) stripping voltammograms (in a 0.5 M KCl solution) of ITO modified with ssDNA (long dash - - - - -) exposed to the complementary (solid ——) or non-complementary (short dash ········) ssDNA labeled with 10 nm gold nanoparticles (1 nM) (C) Tapping mode AFM image (1μm$^2$ with a height scale of 50 nm) of ITO modified with ssDNA exposed to the complementary ssDNA labeled with 10 nm gold nanoparticles (1 nM).**

Figure 5.4A shows XPS spectra of Au 4$f_{7/2,5/2}$ (83.3, 87.0 eV) that demonstrate the presence of gold nanoparticle labels by a comparison of ITO modified with ssDNA coupled through a monolayer of 12-PDA (long dash) exposed to the complementary (solid) or non-complementary (short dash) ssDNA labeled with a 10 nm gold nanoparticle (1nM). Figure 5.4B shows the stripping voltammograms in a 0.5 M KCl solution of ITO modified with ssDNA coupled through a monolayer of 12-PDA exposed to the complementary (solid) or non-complementary (short dash) ssDNA labeled with a 10 nm gold nanoparticle (1nM). The stripping voltammogram shows an oxidative (864 mV) and reductive (465 mV) peak of gold on the surface. The stripping voltammograms showed in Figure 1B illustrate that non-specific binding of the non-complementary ssDNA to the ssDNA modified ITO surface based on the integrated area of the reductive peak of the gold was at most ~ 13 % for the 1 nM solution of Au nanoparticles used in these experiments. In fact, if the analysis were based on the oxidative wave alone one would predict significantly less non-specific binding. The corresponding AFM image ($1\mu m^2$ image with a 50 nm height scale) captured in tapping mode for the hybridization of the complementary ssDNA / gold nanoparticle conjugate to the ssDNA modified ITO surface is shown in Figure 5.4C. This image allows the number of gold nanoparticles to be counted in the $1\mu m^2$ area studied here. Based on the surface coverage of probe ssDNA on the ITO surface and the surface coverage of the gold nanoparticle / target ssDNA conjugates (assuming that each nanoparticle represents one surface DNA hybridization event), a surface DNA hybridization efficiency of 0.4±0.1 % can be estimated for this system.

The presence of gold nanoparticles attached to the DNA modified ITO surface through DNA hybridization was also detected by thermography, photoelectrochemistry and stripping voltammetry. For these experiments, the hybridization was carried out for 19 hours at 37 °C in a shaking incubator. The thermographic and photoelectrical experiments are based on laser induced temperature jumps where the plasmon band of the gold nanoparticles bound to the DNA modified ITO surface through DNA hybridization is excited by 532 nm laser radiation. The temperature increase was either monitored on a dry surface using a thermographic camera or in solution using a home-built electrochemical cell that allowed the sample to be irradiated while monitoring the resulting current from the temperature increase.[33] The presence of the gold nanoparticles was also confirmed by stripping voltammetry where the oxidation and reduction of the gold nanoparticles is detected (data not shown).

After irradiating the hybridized sample for 30 seconds with 532 nm radiation (100 W/cm$^2$), the gold nanoparticles attached to the ITO substrate through DNA hybridization (1 nM gold nanoparticle / ssDNA conjugate) yielded a temperature increase of 3.9 °C over background (ssDNA modified ITO).

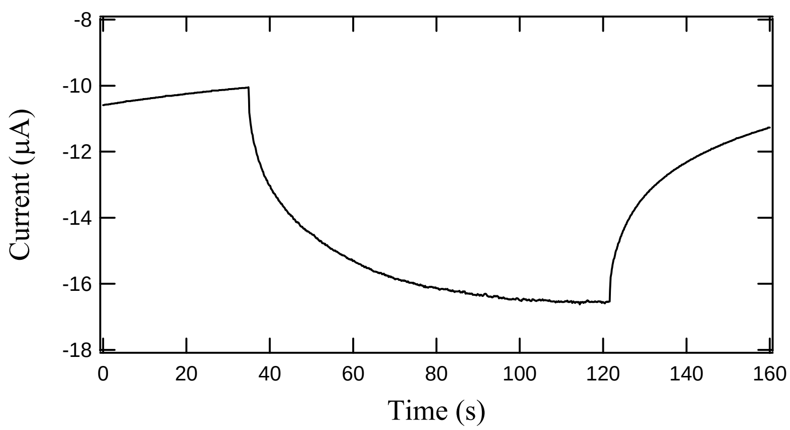


**Figure 5.5. Anodic current versus time for an ITO electrode modified with ssDNA and hybridized with the complimentary ssDNA gold-nanoparticle conjugate (1 nM). The measurement was done in 0.1 M potassium phosphate buffer with 0.05 M EDTA. At 30 s the sample was illuminated with 532 nm laser light with a power density of approximately 100 W/cm$^2$. After 90 s the laser light was switched off. The potential was held at 0.7 V versus a Ag(s)/AgCl reference electrode which was not fixed isothermally.**

The change in current due to this temperature increase was monitored with chronoamperometry where the potential was stepped to 0.7 V versus $Ag_{(s)}$/AgCl and the current was monitored over time (Figure 5.5). When the sample was irradiated with 532 nm light, the current deceased rapidly at first and then slowly leveled off over a period of 120 seconds. At this point the laser was switched off and it was observed that the current returned to its initial value. The fast components of the temperature change in this experiment are typical for laser induced temperature jump experiments. [36-39]

DNA hybridization on ITO surfaces was also detected by the oxidation of a specific redox species catalyzed by gold nanoparticles. The identity of the redox species is crucial because the electron transfer kinetics of this species must be slow on bare ITO but fast in the presence of gold nanoparticles. The change in electron transfer rate can easily be detected using cyclic voltammetry. The best redox species for this type of electrochemical detection strategy was determined to be $FeCl_2$ by comparison of a number of sacrificial donors such as triethanolamine and ethylene diamine tetraacetic acid.

The presence of $FeCl_2$ in solution generated oxidation currents that are much larger than those recorded by electrochemical stripping. The limit of detection of gold nanoparticles was determined to be 10 pM, which is lower than the limit of detection obtained by stripping experiments. The results of this technique are shown in Figure 5.6A where a range of concentrations of target gold nanoparticle / ssDNA conjugates was used to hybridize to ssDNA modified ITO surfaces.

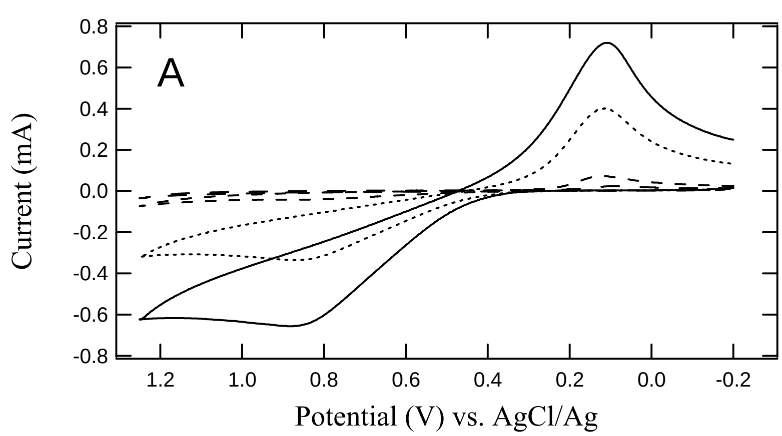

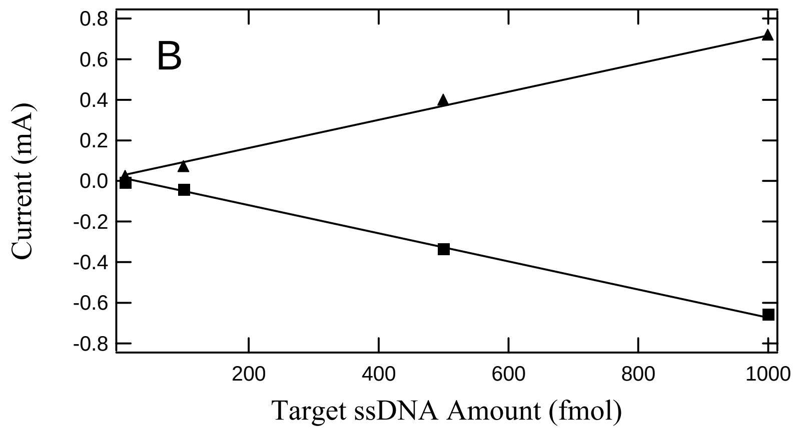


**Figure 5.6. A. Electrochemical response for 100 mM $FeCl_2$ (scan rate 100 mV/s) as a function of the amount of target ssDNA / gold nanoparticle conjugate in the hybridization solution. The four target concentrations were 1 nM, 500 pM, 100 pM and 10 pM of the gold nanoparticles (modified with the target ssDNA). The hybridization was allowed to proceed for 1 hour at 45°C and the solution was then gradually cooled to room temperature overnight. B. Electrochemical response as a function of the amount of the gold nanoparticle / target ssDNA in the hybridization solution at 887 mV (squares) for the oxidation current and 109 mV (triangles) for the reduction current fit globally to a straight line (solid).**

The concentrations of the gold nanoparticle / ssDNA conjugate solutions used in these experiments were 1 nM, 500 pM, 100 pM and 10 pM. Each of these solutions were hybridized to the ssDNA modified ITO surfaces by maintaining the solution at 45 °C for one hour and then allowing it to cool to room temperature overnight. The presence of the gold nanoparticle-ssDNA conjugates were then detected electrochemically. The currents measured at the maximum of the oxidation (887 mV) and reductive peak (109 mV) recorded by CV were found to increase linearly with the target concentration in solution (Figure 5.6B).

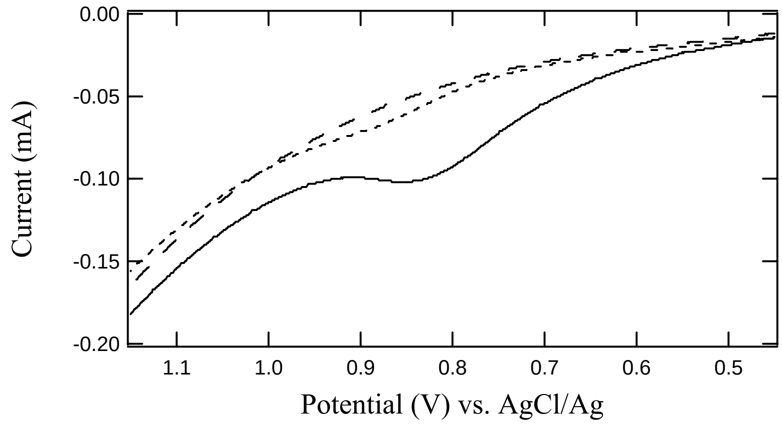


**Figure 5.7. Electrochemical response for 100 mM $FeCl_2$ (scan rate 100 mV/s) as a function of the amount of target ssDNA in the hybridization solution with improved hybridization conditions. The three target amounts were 100 pM, 10 pM and 1 pM of the gold nanoparticles (10 nm diameter) modified with the target ssDNA. The hybridization was allowed to proceed at 37°C for nineteen hours in a shaking incubator.**

Figure 5.7 shows the electrochemical results for the detection of gold nanoparticles attached to the ITO surface through DNA hybridization using $FeCl_2$ as the redox species in solution. Three gold nanoparticle / ssDNA target concentrations were used: 100, 10 and 1 pM. Figure 5.7 shows that it was possible to detect gold nanoparticles modified with ssDNA targets bound to the ITO substrate for concentrations as low as 10 pM. For this system, the hybridization efficiency was found to increase when hybridization was performed at 37 °C for 19 hours in a shaking incubator.

## *5.4 Conclusion*

Indium tin oxide (ITO) thin films were successfully modified with single stranded DNA. This modification was achieved by coupling the amine group of 5'-$H_2N(CH_2)_3$-labeled ssDNA probes to the carboxylic acid moiety of a monolayer of 12-phosphonodododecanoic acid on the ITO surface by EDC coupling to create an amide linkage. The resulting surface was characterized by X-ray photoelectron and reflectance FTIR spectroscopy to confirm the presence of the ssDNA probe oliognucleotides on the surface. DNA hybridization to ssDNA modified ITO surfaces was detected by labeling ssDNA targets with 10 nm gold nanoparticles. Therefore the detection of gold nanoparticles on the ITO surface confirmed selective DNA hybridization. The gold nanoparticles were detected by XPS, stripping voltammetry, AFM, thermography and photoelectrochemistry (chronoamperometry) for a 1 nM gold nanoparticle / target ssDNA concentration in the hybridization solution. However target concentrations as low as 10 pM gold nanoparticles modified with target ssDNA were detected through the electrochemical oxidation of $FeCl_2$ catalyzed by the gold nanoparticles bound to the ITO surface via DNA hybridization. At target ssDNA concentrations typically used in biological assays, the amount of non-specific binding found in these studies would be nearly undetectable. The hybridization efficiency is low but consistent with results published previously that reported when nanoparticle labels and the surface density of probes is high hybridization the efficiency is comparatively low.[17] Also the measured hybridization efficiency is based on the surface coverage of ssDNA on ITO surface measured by chronocoulometry which, estimated the higher limit of surface coverage yielding the lower limit for hybridization efficiency.

## *Acknowledgements*

Selina Moses, Marc Sauthier, and Lisa Lowe were supported by Applied Biosystems, Inc. Scott H. Brewer was supported by NIH Biotechnology Training Grant T32-GM08776. Support and computational facilities were provided by the North Carolina State

University High Performance Computing Resource. The authors would like to thank Dr. Kimberly Briggman at NIST for her help in the acquisition of the reflectance FTIR spectra.

## *References*

(1) Herne, T. M.; Tarlov, M. J. J. Am. Chem. Soc. 1997, 119, 8916-8920.
(2) Taton, T. A.; Mirkin, C. A.; Letsinger, R. L. Science 2000, 289, 1757-1760.
(3) Chrisey, L. A.; Lee, G. U.; Oferrall, C. E. 1996, 24, 3031-3039.
(4) Ulman, A. Chemical Reviews 1996, 96, 1533-1554.
(5) Lockhart, D. J.; Winzeler, E. A. Nature 2000, 405, 827-836.
(6) Chee, M.; Yang, R.; Hubbell, E.; Berno, A.; Huang, X. C.; Stern, D.; Winkler, J.; Lockhart, D. J.; Morris, M. S.; Fodor, S. P. A. Science 1996, 274, 610-614.
(7) Fodor, S. P. A.; Read, J. L.; Pirrung, M. C.; Stryer, L.; Lu, A. T.; Solas, D. Science 1991, 251, 767-773.
(8) Bulyk, M. L.; Gentalen, E.; Lockhart, D. J.; Church, G. M. Nat. Biotechnol. 1999, 17, 573-577.
(9) He, L.; Musick, M. D.; Nicewarner, S. R.; Salinas, F. G.; Benkovic, S. J.; Natan, M. J.; Keating, C. D. J. Am. Chem. Soc. 2000, 122, 9071-9077.
(10) Brockman, J. M.; Frutos, A. G.; Corn, R. M. J. Am. Chem. Soc. 1999, 121, 8044-8051.
(11) Esch, M. B.; Locascio, L. E.; Tarlov, M. J.; Durst, R. A. Anal. Chem. 2001, 73, 2952-2958.
(12) Steel, A. B.; Herne, T. M.; Tarlov, M. J. Anal. Chem. 1998, 70, 4670-4677.
(13) Steel, A. B.; Herne, T. M.; Tarlov, M. J. Bioconjugate Chem. 1999, 10, 419-423.
(14) Brewer, S. H.; Anthireya, S. J.; Lappi, S. E.; Drapcho, D. L.; Franzen, S. Langmuir 2002, 18, 4460-4464.
(15) Cao, Y. W.; Jin, R.; Mirkin, C. A. J. Am. Chem. Soc. 2001, 123, 7961-7962.
(16) Demers, L. M.; Mirkin, C. A.; Mucic, R. C.; Reynolds, R. A.; Letsinger, R. L.; Elghanian, R.; Viswanadham, G. Anal. Chem. 2000, 72, 5535-5541.
(17) Sauthier, M.; Carroll, R.; Gorman, C.; Franzen, S. Langmuir 2002, 18, 1825-1830.
(18) Brewer, S. H.; Brown, D. A.; Franzen, S. Langmuir 2002, 18, 6857-6865.
(19) Gardner, T.; Frisbie, C.; Wrighton, M. The Journal of the American Chemical Society 1995, 117, 6927-6933.
(20) Yan, C.; Zharnikov, M.; Golzhauser, A.; Grunze, M. Langmuir 2000, 16, 6208-6215.
(21) VanderKam, S.; Gawalt, E.; Schwartz, J.; Bocarsly, A. Langmuir 1999, 15, 6598-6600.
(22) Oh, S.; Yun, Y.; Kim, D.; Han, S. Langmuir 1999, 15, 4690-4692.

(23) Markovich, I.; Mandler, D. Journal of Electroanalytical Chemistry 2001, 500, 453-460.
(24) Popovich, N. D.; Yen, B. K.; Wong, S. Langmuir 2003, 19, 1324-1329.
(25) Armistead, P.; Thorp, H. Analytical Chemistry 2000, 72, 3764-3770.
(26) Armistead, P.; Thorp, H. Analytical Chemistry 2001, 73, 558-564.
(27) Ambrosini, A.; Duarte, A.; Poeppelmeier, K. R.; Lane, M.; Kannewurf, C. R.; Mason, T. O. J. Solid State Chem. 2000, 153, 41-47.
(28) Brewer, S. H.; Franzen, S. J. Alloy. Compd. 2002, 338, 73-79.
(29) Brewer, S. H.; Franzen, S. Journal of Physical Chemistry B 2002, 106, 12986-12992.
(30) Hamberg, I.; Hjortsberg, A.; Granqvist, C. Applied Physics Letters 1982, 40, 362-364.
(31) Hamberg, I.; Granqvist, C. G.; Berggren, K. F.; Sernelius, B. E.; Engstrom, L. Phys. Rev. B 1984, 30, 3240-3249.
(32) Hamberg, I.; Granqvist, C. G. J. Appl. Phys. 1986, 60, R123-R159.
(33) Lowe, L. B.; Brewer, S. H.; Kramer, S.; Fuierer, R. R.; Qian, G. G.; Agbasi-Porter, C. O.; Moses, S.; Franzen, S.; Feldheim, D. L. 2003, 125, 14258-14259.
(34) Loweth, C. J.; Caldwell, W. B.; Peng, X. G.; Alivisatos, A. P.; Schultz, P. G. 1999, 38, 1808-1812.
(35) Delley, B. J. Phys. Chem. 1990, 92, 508-517.
(36) Smalley, J. F.; Krishnan, C. V.; Goldman, M.; Feldberg, S. W.; Ruzic, I. 1988, 248, 255-282.
(37) Smalley, J. F.; Geng, L.; Chen, A.; Feldberg, S. W.; Lewis, N. S.; Cali, G. 2003, 549, 13-24.
(38) Smalley, J. F.; Chalfant, K.; Feldberg, S. W.; Nahir, T. M.; Bowden, E. F. 1999, 103, 1676-1685.
(39) Smalley, J. F.; Geng, L.; Feldberg, S. W.; Rogers, L. C.; Leddy, J. 1993, 356, 181-200.

# CHAPTER 6

# Detection of Biomolecules on metal-oxide substrates

## *6.1 Detection of DNA on Indium tin oxide (ITO) substrates by photoelectrochemistry*

### 6.1.1 Photoelectrochemistry – a sensitive detection tool for biomolecules

Continuous research is being done to discover sensitive and inexpensive methods to detect and quantify biological substances immobilized on surfaces. To detect highly specific biological reactions like DNA and RNA hybridization, small protein-ligand systems and antigen- antibody assays, conventional methods based on fluorescent labeling, radioisotope labeling and chemiluminescent (CL) or electrochemiluminescent (ECL) labeling have been explored. Compared to all other techniques CL and ECL have the highest sensitivity due to the low background signal associated with the methods.[1] The reduction in background is achieved by using two separate forms of signal for excitation and detection. To combine the advantages of low cost associated with electronic detection used in electrochemistry and sensitivity as high as ECL photoelectrochemistry is being used in microarray analysis.

The focus of the analytical phase of the research is to create a light addressable array to detect biomolecular events on metal-oxide substrates using photoelectrochemistry. Our goal is to test whether target DNA labeled with $TiO_2$ nanoparticles functionalized with a Ru dye complex upon hybridization to surface bound probe DNA or RNA can be detected by photoelectrochemical analysis. The experimental conditions are discussed in detail in this chapter.

### 6.1.2 Chemiluminescence

Luminescence is emission of visible or near UV radiation when electrons in excited orbitals decay to the ground state. The source of light is the potential energy of electronic transitions within the atoms or the molecules. One of the ways electronically excited states can be generated is by a chemical reaction leading to chemiluminescence.

CL provides a mean to carry out clinical assays with high sensitivity over a wide range of concentration. It does not require an expensive apparatus hence can be used in routine immunoassays. In immunoassays the antibodies are typically labeled with an additional substance such that, upon the addition of other reactants, such as an enzyme, CL occurs. The luminescence intensity is dependent on the concentration of a particular substance in the reaction. To obtain a calibration curve various known concentrations must be tested using a standard CL technique relating concentrations of a specific substance (for example, estradiol) to emission intensity of the reaction. Once a standard curve is obtained, the standard CL test may be performed on unknown substance quantities to obtain the concentration of the substance present in the sample based on the luminescent intensity. A highly sensitive photomultiplier tube is typically used in measuring the luminescence of immunoassays as the quantum yield in these reactions is typically very low. The photomulitiplier device provides a current output (typically microamperes) proportional to the number of photons hitting it from the CL reaction.

Electrochemiluminescence (ECL) is a form of chemiluminescence in which the light emitting CL reaction is activated with the use of electric current flow. The advantage is that ECL provides an opportunity for controlling the time and position of the light emitting reaction until the desired molecules attached to the CL agents are confined to a certain location thereby increasing the detector sensitivity and the signal to noise ratio. Similar control over light emission can be attained with alternative methods, such as fluorescence; however, the instrumentation is likely to be more sophisticated and expensive.[2] ECL using $Ru(bpy)_3^{2+}$ attached to DNA provides a sensitive method of detection. [3]The $Ru(bpy)_3^{2+}$ labels on DNA are oxidized to $Ru(bpy)_3^{3+}$, and ECL is generated by using a sacrificial reductant, often tripropylamine (TPA). ECL depends on generation of photoexcited $[Ru(bpy)_3^{2+}]^*$ in a process involving reaction of a radical form of the reductant with electrochemically generated $Ru(bpy)_3^{3+}$ .Alternatively, $Ru(bpy)_3^{+}$ is formed by reduction of $Ru(bpy)_3^{2+}$ by the radical, followed by reaction of RuI and RuIII species to give $[Ru(bpy)_3^{2+}]^*$. Decay of $[Ru(bpy)_3^{2+}]^*$ to the ground state with luminescent emission at 610 nm is measured in the detection step.[4] The detection limit reported is as low as 10 oligonucleotide molecules. But ECL has its own disadvantages-the labeling procedure is complex and renders some sites inactive on the oligonucleotides

The photoelectrochemistry of $[Ru(bipy)_3]^{2+}$on gold substrates has been recently attempted. In 1997 Yamada et al.[5] demonstrated photocurrent from $[Ru(bipy)_3]^{2+}$ attached to a gold substrate through a thiol linker. A later study by Koide et al.[6] focused on the effect of spacer chain length between $[Ru(bipy)_3]^{2+}$ and the thiol. Feldheim et al. modified Tris-2,2'-bipyridyl ruthenium (II) by attachment of a thiol to one of the pyridine ligand via an alkane chain. This thiolated $[Ru(bipy)_3]^{2+}$ and the target oligo can bind to a gold nanoparticle and can be used for DNA array on gold substrate. The minimum detection limit obtained from this system was 0.5 nM[7]. The two possible reasons for low photocurrent could be due to inefficient charge injection by $[Ru(bipy)_3]^{2+}$ into the gold nanoparticle and the background on Au electrodes caused by a photothermal effect. The photothermal effect is seen when gold is irradiated with visible light causing excitation of the conduction electrons in a surface plasmon. The absorbed energy is dissipated as heat into the surroundings. [8] In studies where photoelectrochemical detection has been carried out using gold as substrate, there is a temperature jump causing a change in double layer capacitance, which causes current to flow. Hence a gold substrate is not ideal for detection of hybridization by photoelectrochemistry with gold colloids as labels. There are also other disadvantages like desorption of probes from gold surface, which that limit the utility of gold electrodes in this type of DNA array technology. [9] Despite the promising preliminary results, a number of barriers have presented themselves vis-à-vis lowering the DNA detection limit to the femtomolar regime. First, the dye molecule used in the experiment was $[Ru(bpy)_2(bpy\text{-}C_8H_{16}SH)]^{2+}$. The carbon chain between the dye and the gold particle slows the electron injection rate and thus lowers the current collected. Secondly, while gold is useful material because it is easy to modify chemically via thiol chemistry, its continuum of states facilitates the back electron transfer of the photoinjected electron. Moreover, thiol monolayers on gold surfaces are not chemically robust. That is, under the modest increases in temperature required to hybridize DNA, some surface-bound ssDNA probe strands desorb. Thus, it is proposed that DNA detection limits can be lowered substantially with the synthesis of new dyes, and the use of new semiconductor nanoparticle labels and surfaces.

### 6.1.3 Photoelectrochemistry: Inspiration from Semiconductor-Nanoparticle Solar Cells

Photoelectrochemical cells usually consist of an electrolyte, semiconductor electrode and a suitable counter electrode. The cell operates to convert light into electricity, with no net change to the electrolyte solution or electrode. The light employed to carry out photoelectrochemical reaction at the semiconductor electrode must have energy greater than the band gap. In wide band gap semiconductors like $TiO_2$ solar energy cannot be utilized effectively as 95% of the total energy lies below 3 eV. Hence dye sensitization of semiconductors is a better approach to be able to use a wider range of wavelengths.

Grätzel in 1991 reported a low-cost, high efficiency solar cell based on dye sensitized colloidal $TiO_2$ films. Although solar energy conversion by photoelectrochemical cells have been studied widely [10,11] these dye-sensitized cells are different than conventional semiconductor devices in that they use the sensitizer to separate the phenomenon of light absorption from charge carrier transport.

Dye sensitization of semiconductors like $TiO_2$ enhances the response of the large gap semiconductors to visible light and increases charge separation distance following photoexcitation.

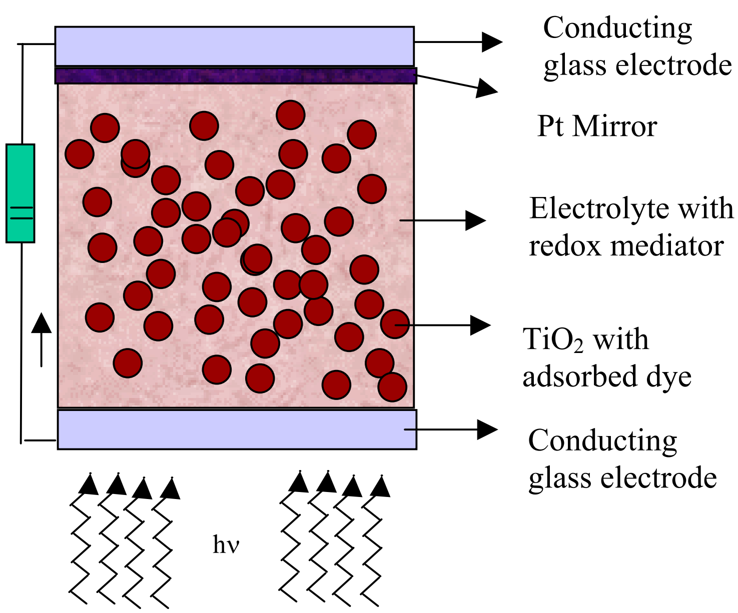


**Figure 6.1.A Dye sensitized Semiconductor Photoelectrochemical Cell.**

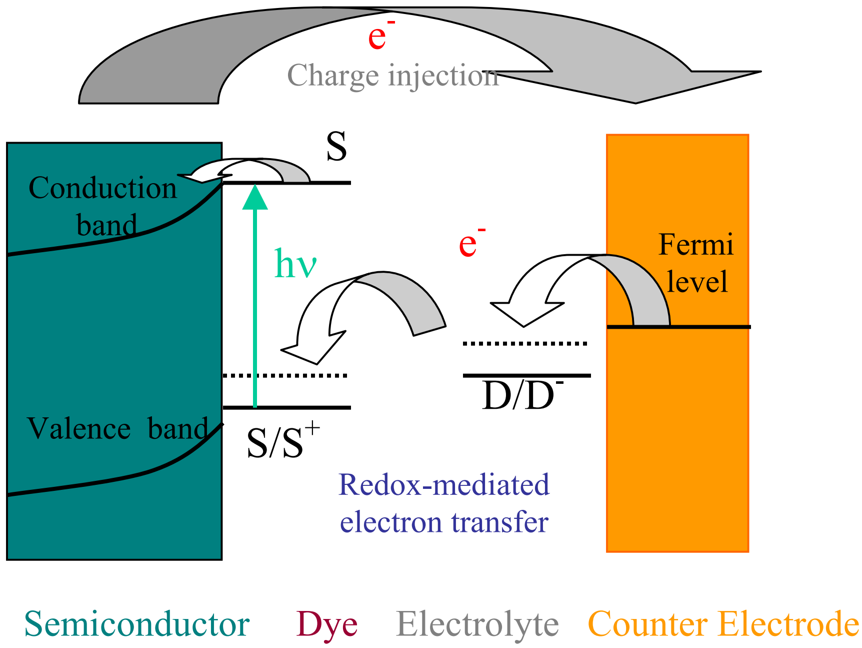


**Figure 6.1.B Pathway of electron flow in a Dye sensitized Semiconductor Photoelectrochemical Cell.**

The generally accepted model for dye sensitization of wide band gap semiconductors is shown in the scheme above, Figure 6.1.B [12] In this model, an excited dye injects an electron into the semiconductor conduction band from a normal distribution of donor levels and becomes oxidized. The electron is swept to the semiconductor bulk by the surface electric field and flows through an external cell to perform useful work. In absence of a suitable donor species in the electrolyte solution the photoprocess would cease when all the dye molecules are consumed. But in the presence of a sacrificial electron donor in the electrolyte solution the dye molecule is reduced regenerating another cycle.

The efficiency of dye-sensitized photoelectrochemical cells in energy conversion has been low because of the poor light harvesting and low conversion yields from solar energy to electricity. The light harvesting is low on a smooth surface where a monomolecular layer of sensitizer absorbs less than 1% of the incident light. Use of multilayers of dye did not improve the harvest efficiency. Matsumara et al. [13]and Alonso et al.[14] used sintered ZnO electrodes to increase the efficiency of sensitization by rose bengal and related dyes. By increasing the roughness of semiconductor surface it is possible to adsorb a larger number of dye molecules directly on the surface in close proximity to the redox electrolyte solution. The conversion yields for these systems were very low ~ 1% and the dyes were unstable. Hence, use of semiconductor films made of sintered $TiO_2$ nanoparticles sensitized with a polypyridyl Ru dye by Grätzel et al showed improved efficiency and higher stability. Though various Ru dye molecules have been studied, the sacrificial electron donor system used for Grätzel cells is always $I^-/I_2$ since the $E^o$ for the conduction band (CB) and valence band (VB) is –0.54 V (less negative than the of the dye of interest) and 2.7 V respectively.

### 6.1.4 Transfer of electron through DNA

It is important to understand the process of transfer of electrons and holes through DNA molecule to be able to use it as building blocks for molecular devices. It was proposed half a century ago that DNA can conduct electric charge. [17]. It is important to understand the conducting properties of DNA not just for academic purposes but also for understanding the diseases it leads to due to DNA damage. Study of distance dependence on rate of transfer of charge has been carried out and is expressed as β value. Due to the fact that the overlap of the wavefunctions of the donor and acceptor decay exponentially the distance dependence of charge transfer can also be expressed as an exponential $k = \exp\{-\beta R\}FCWD$ where FCWD is the Frank-Condon weighted density of states. Two conflicting theories have formulated recently by researchers studying the distance dependence on charge transfer. The first report that DNA acts as a molecular wire by conducting electrons via the $\pi$ orbitals along its backbone as there is no distance dependence.[18] In contrast Giese etal [19] in 1998 and others indicate a strong distance dependence suggesting that DNA is wide band-gap semiconductor. A new mechanism proposed by Giese et al. and other researchers predicts the mechanism of charge transfer in DNA based on distance and sequence dependence. Ionization of DNA by photolysis or chemi-ionization results in formation of a positive "hole". The positive hole is then transmitted to a Guanine moiety on the DNA. This intramolecular "hopping" of electron to a G base arises from the fact that the different base radicals have different reduction potential and Guanine radical has the lowest reduction potential. [20] It is accepted that charges are transported over long distances by multistep hopping reaction where positive charges move between guanines as shown in Figure 6.2. In cases where the guanine sites are distant there is efficient charge transfer seen which is not adequately explained in the "G hopping" mechanism. A study conducted by Bernd Giese *et a.l* [21] showed that the rate of charge transfer between two G decreases with increasing separation only if the G's are separated by no more than three base pairs. If more bridging base pairs are present then the transfer rate exhibit weak distance dependence. This is attributed to the fact that at shorter distances coherent superexchange charge transfer (tunnelling) occurs and as the distance increases a thermally induced hopping of charges between adenine bases (A-hopping) is observed.

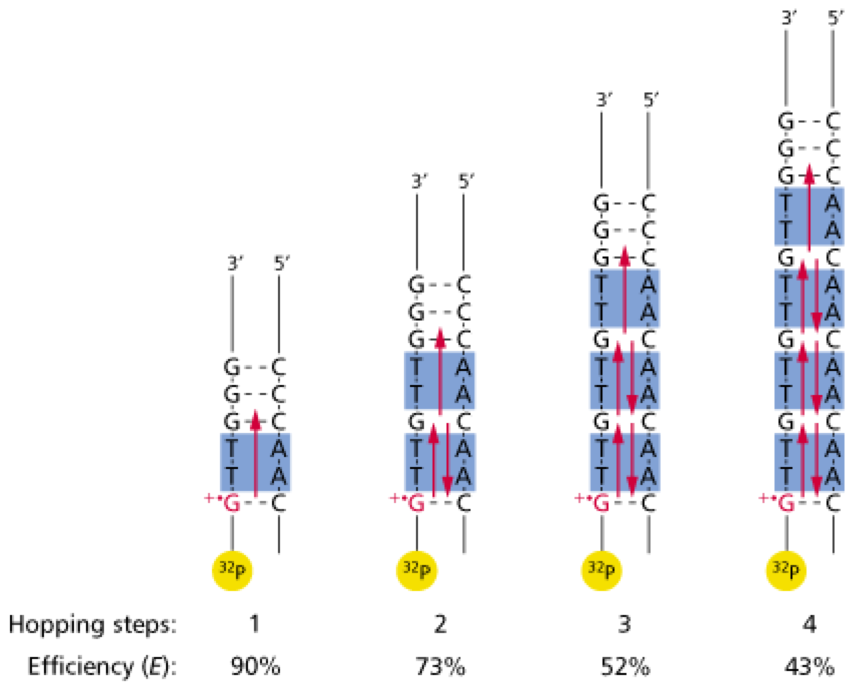


**Figure 6.2 Electron hopping in DNA**
http://www.chemsoc.org/chembytes/ezine/2000/giese_jul00.htm

The focus of the current research is to develop a DNA array that consists of ITO substrate with ssDNA probes, functionalize $TiO_2$ nanoparticles with light-absorbing dye molecule and a linker that can bind to the ssDNA probe. In the sandwich assay format the target oligo hybridizes to the probe on the ITO surface and on the nanoparticles surface bringing the dye molecule together with the nanoparticle in close proximity to the ITO surface.  When the laser excites the dye molecule, it injects an electron into the electrode creating a signal, and the electrons are replenished by the sacrificial donor present in the electrolyte. Metal oxide substrates like indium tin oxide (ITO) open a whole new area of DNA array technology by providing a novel method to increase the sensitivity of the measurement.  Replacing the gold by ITO electrodes and using metal oxide nanoparticles like $TiO_2$ with a wide band gap can eliminate the photothermal effect that gives rise to the background current that was observed in the gold nanoparticle system described in previous chapters. Also the efficiency of charge injection from dye molecule to the metal-oxide nanoparticles will be enhanced. Sensitization of nanocrystalline titanium dioxide to visible light with dye molecules has been done by Grätzel et al. [22] The ruthenium polypyridyl complexes on attachment to a high surface area $TiO_2$ electrode can effectively convert solar energy into electricity. [23]

## 6.2 Research Design

### 6.2.1 Synthesis of nanocrystalline $TiO_2$.

$TiO_2$ is one of the most important inorganic products in the chemical industry, due to its chemical stability, low toxicity and low cost. $TiO_2$ has a very high refractive index, higher than any other white pigment. Among the many applications of $TiO_2$ the most important ones are photoelectrochemical cells to convert solar energy into electricity, photocatalysis and electrochemical gas sensors. Surface modifications and functionalization of these nanoparticles is an important area of investigation.

Nanocrystalline titanium dioxide was synthesized by a hydrothermal technique – applying elevated temperature and pressure to aqueous solutions [24]. 10.0 ml Analytical grade $TiCl_4$ was added dropwise into 15.7 ml of concentrated HCl to form $H_2TiCl_6$. Into a mixture of 25ml of $H_2TiCl_6$ and 75 ml of distilled water an excess of $NH_3$(25%) aqueous was added with vigorous stirring to form white amorphous $TiO_2.nH_2O$ precipitate. The precipitate was filtered and washed several times and were placed in an autoclave at 353K for ~ 16hrs. The resulting solution of $TiO_2$ nanoparticles was dispersed in two distinct phases, a white solid phase composed of nanoparticles at the bottom and a clear aqueous phase supernatant. The UV-Vis and TEM indicates that there are smaller $TiO_2$ nanoparticles present in the supernatant. This solution was filtered and the washed atleast 5 times to remove traces of Cl. The white powder was then dried at room temperature and stored in airtight vials. A small fraction of this $TiO_2$ sample was used for Powder X-ray Diffraction analysis which revealed a crystalline Anatase phase with crystal size ~ 100nm as seen in Figure 6.3

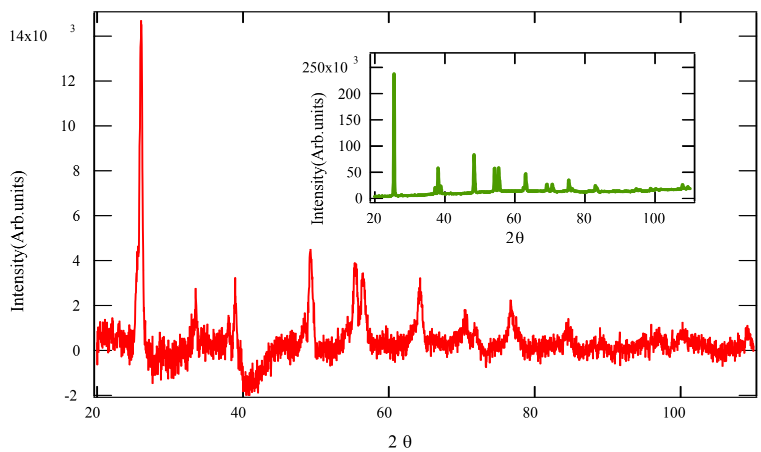


**Figure 6.3. X-ray diffraction pattern of nanocrystalline $TiO_2$.**

The UV-visible spectrum of $TiO_2$ nanoparticles in the supernatant solution is seen in Figure 6.4.

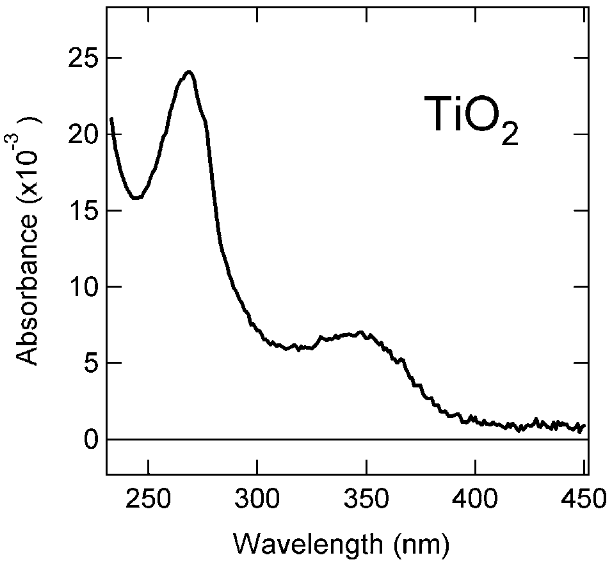


**Figure 6.4 UV-Visible spectrum of aqueous $TiO_2$.**

Three different polymorphs of $TiO_2$ exist as shown in Figure 6.5. Rutile is the thermodynamically stable polymorph under atmospheric pressure while anatase is metastable at temperatures below 700 °C. Brookite is a high-pressure polymorph of $TiO_2$.[25]

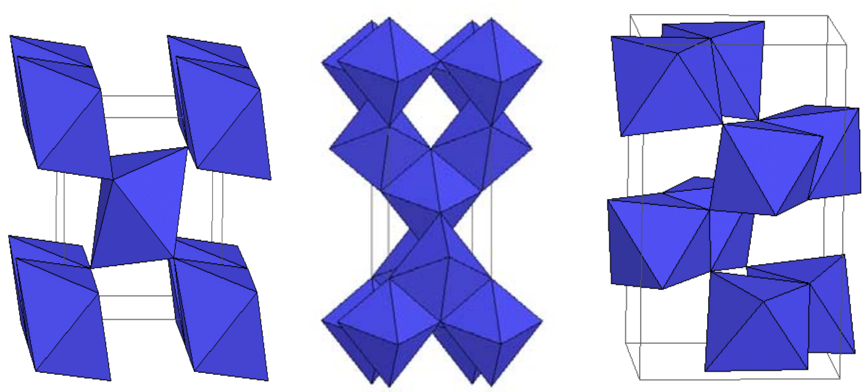

**Figure 6.5. Crystal structure of Rutile, Anatase and Brookite $TiO_2$**

The metal nanoparticles have a higher photothermal current in comparison to the metal oxide nanoparticles. The strategy that can be used to functionalize the $TiO_2$

nanoparticles for use as labels to detect biomolecules and DNA hybridization by photoelectrochemistry is described in detail.

### 6.2.2 Synthesis of the Ruthenium polypyridyl compound

Cis-[4,4'-$(COOH)_2$–2,2'-bipyridine]$_2$Ru$(Cl^-)_2$ (hereafter abbreviated as [4,4'-(LL)]$_2$Ru$(Cl)_2$ ) is one of the many Ru polypyridyl complxes used in dye sensitized photoelectrochemical cells to efficiently convert solar energy into electricity. [26]For such bidentate polypyridine ligands intense MLCT absorption bands are observed from 400-600 nm, while absorption at longer wavelengths is negligible. The other important redox property is a positive redox potential to ensure rapid donor oxidation and slow recombination of the conduction band electrons with the oxidized dye molecule.

0.19 mmol of $RuCl_3.3H_2O$ and 0.38 mmol of 4,4'- (LL) were dissolved in 10 ml DMF and refluxed under Argon for 8 h. The resulting solution was concentrated under vacuum and cooled. The [4,4'-(LL)]$_2$Ru$(Cl)_2$ complex was then precipitated by adding ether. The spectroscopic property of this complex is seen in the UV-Vis spectrum of the [4,4'-(LL)]$_2$Ru$(Cl)_2$ in water in Figure 6.6.

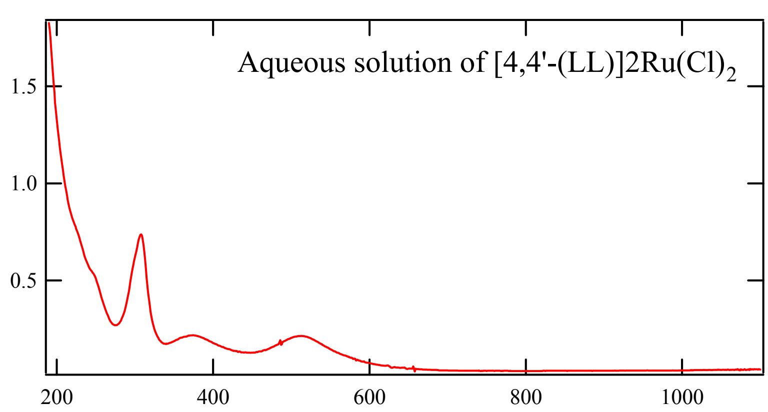


**Figure 6.6 UV-Visible spectrum of [4,4'-(LL)]$_2$Ru$(Cl)_2$ in water**

The hydroxyl groups on the surface of $TiO_2$ contribute to their acidic or basic properties. The surface chemistry of $TiO_2$ occurs by the reaction of the surface hydroxyl groups with the carboxylic acid groups to form ester linkage.[26] When the semiconductor particles are in nanometer range a large fraction of the surface atoms are coordinated with -OH groups and solvent molecules. A 4 nm particle of $TiO_2$ has 40% of the Ti atoms located on the surface of the particle. Since the particles have a large curvature a major fraction of these atoms become 'corner dislocation' having upto 4 bonds saturated with –OH groups.

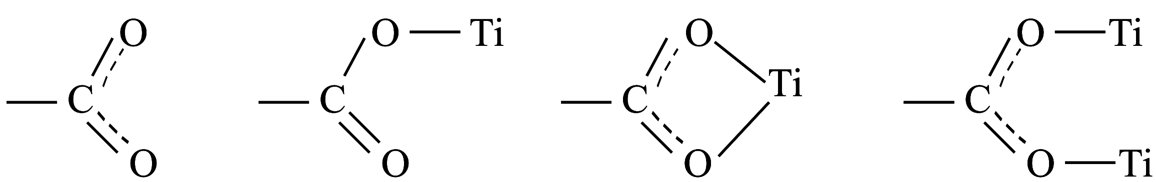

A B C D

**Figure 6.7 Reaction scheme of surface hydroxyl groups of $TiO_2$ with carboxylic acid**

### 6.2.3 Surface attachment of DNA to ITO.

Scheme 1 shows the formation of a monolayer of 12-phosphonododecanoic acid (10mM in 50/50 DMSO/18 MΩ cm $H_2O$ for 16 hours) on ITO and then the activation of the carboxylic acid of this molecule by EDC and the subsequent attack of a primary amine on this activated carboxylic acid to form an amide bond. When the primary amine is 5' modified $C_3NH_2$ DNA the later two steps in Scheme 6.1 are combined into one step with 1μM 5' modified $C_3NH_2$ DNA and 200mM EDC for 4 hours in 0.1 MES (2-(N-morpholino) ethane sulfonic acid) buffer at pH 5 with 0.25M NaCl. Once the amide bond is formed, ethanolamine (1M for 1 hour) scavenges the remaining activated carboxylic acid groups prior to DNA hybridization.[27,28,29,30,31]

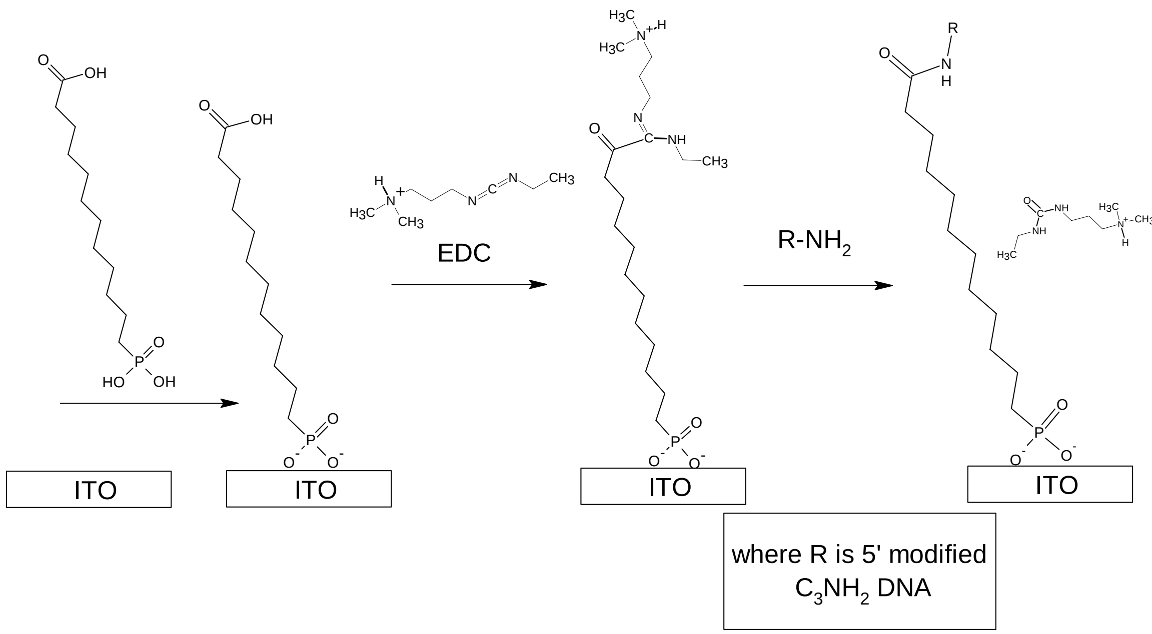


**Scheme 6.1. Formation of an amide bond by the activation of the carboxylic acid on a monolayer of 12-phosphonododecanoic acid on ITO by EDC (1-ethyl-3-(3-dimethylaminopropyl)carbodiimide hydrochloride) with 5' modified C3NH2 DNA.**

## 6.2.4 Scheme for creating DNA microarray

### 6.2.4.1 Functionalization of $TiO_2$ nanoparticles.

The $TiO_2$ nanocrystals that were synthesized were functionalized by direct attachment of $[4,4'\text{-(LL)}]_2Ru(Cl)_2$ or a mixture of streptavidin and $[4,4'\text{-(LL)}]_2Ru(Cl)_2$. The advantage of this direct attachment and the electrostatic binding of anionic carboxylate group on the molecule is that Ru metal will be placed very close to the $TiO_2$ nanoparticle facilitating effcient charge transfer. The second advantage is that they prevent the negatively charged phosphodiester backbone of DNA from adhering electrostatically to the $TiO_2$ nanoparticle surface.

### 6.2.4.1.1 Condensation of $TiO_2$ nanoparticles with (LL)]$_2$Ru(Cl)$_2$

The proposed method of functionalization of $TiO_2$ is carried out by directly attaching the [4,4'-(LL)]$_2$Ru(Cl)$_2$ to $TiO_2$ nanoparticles. This is achieved by making a 10mM aqueous solution of [4,4'-(LL)]$_2$Ru(Cl)$_2$ . 50 ul of this [4,4'-(LL)]$_2$Ru(Cl)$_2$ is reacted with 500 ul of supernatant $TiO_2$ solution and reacted for 15 min. The unbound fraction of [4,4'-(LL)]$_2$Ru(Cl)$_2$ is then separated by a centrifugation at 14000 RPM with a 30,000 cutoff microcon. Several washing steps were carried out to ensure all unbound [4,4'-(LL)]$_2$Ru(Cl)$_2$ is separated from $TiO_2$ functionalized with [4,4'-(LL)]$_2$Ru(Cl)$_2$

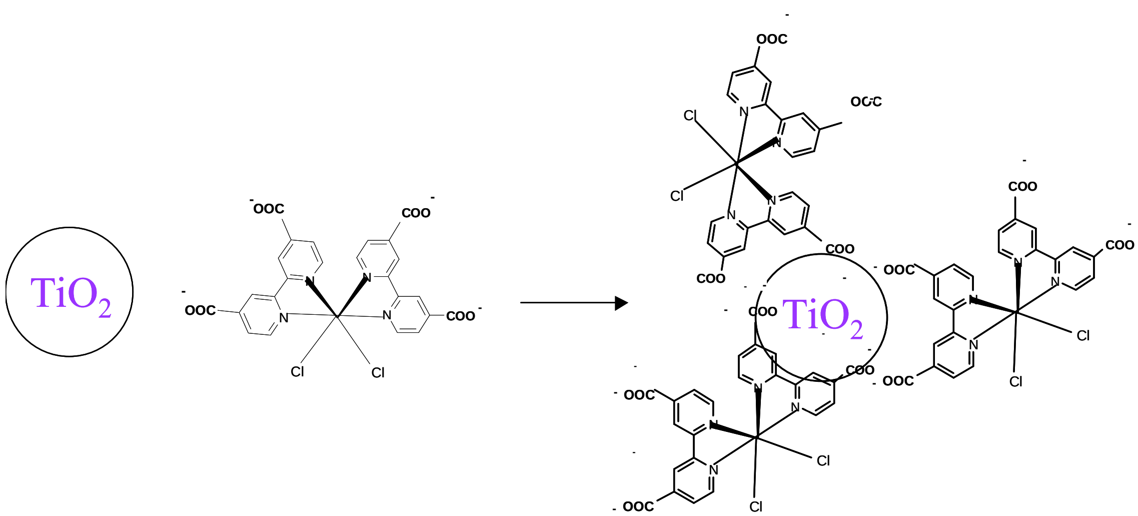


**Scheme 6.2 Functionalization of $TiO_2$ nanoparticles with [4,4'-(LL)]$_2$Ru(Cl)$_2$**

As mentioned earlier the supernatant solution contains $TiO_2$ nanoparticles which form aggregates as seen in TEM image, Figure 6.8 A. Functionalization of $TiO_2$ nanoparticles present in the supernatant liquid with the [4,4'-(LL)]$_2$Ru(Cl)$_2$ was carried out as described above. According to TEM studies the nanoparticles fused together upon reaction with $[4,4'\text{-}(LL)]_2Ru(Cl)_2$ forming half a micron size particles as seen in Figure 6.8B.

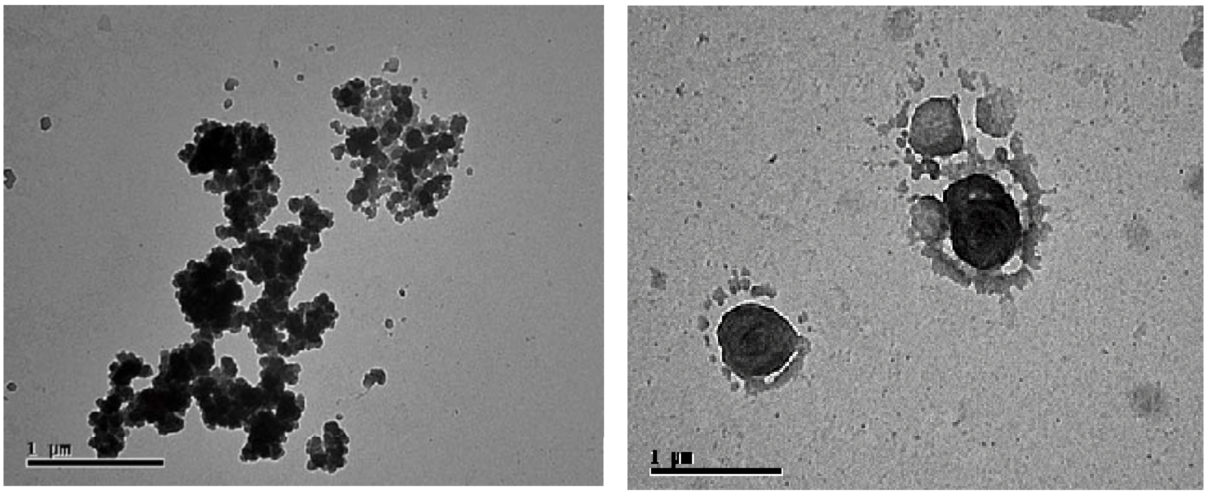


**Figure 6.8 TEM images of A. $TiO_2$ nanoparticles in the supernatant suspension. B. $TiO_2$ racted with $[4,4'\text{-}(LL)]_2Ru(Cl)_2$.**

### 6.2.4.1.2 Functionalization of $TiO_2$ nanoparticles with Streptavidin

To address the issue of size and stability of functionalized $TiO_2$ nanoparticles surface modifier streptavidin was explored. To be able to employ a surface modification strategy that can synthesise monodisperse , stable and optimally sized nanoparticles, which can be captured directly in a direct or sandwich DNA assay, Scheme 6.3 was used. The aliquots of $TiO_2$ nanoparticle solution is prepared by weighing 5 mg of dried $TiO_2$ powder and dissolving it in 500 ul deionized water.

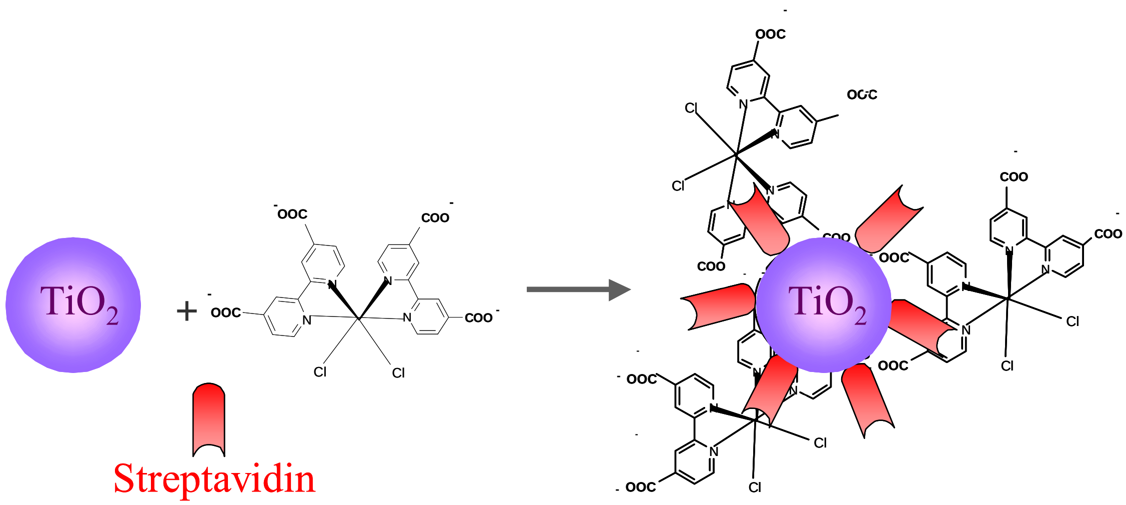


**Scheme 6.3 Functionalization of $TiO_2$ nanoparticles by Streptavidin and $[4,4'\text{-}(LL)]_2Ru(Cl)_2$**

From the TEM image in Figure 6.9 it can be noted that the $TiO_2$ nanoparticles without any surface modification are not monodisperse. Also the $TiO_2$ nanoparticles that were functionalized with only $[4,4'\text{-}(LL)]_2Ru(Cl)_2$ formed many aggregates as seen in the TEM

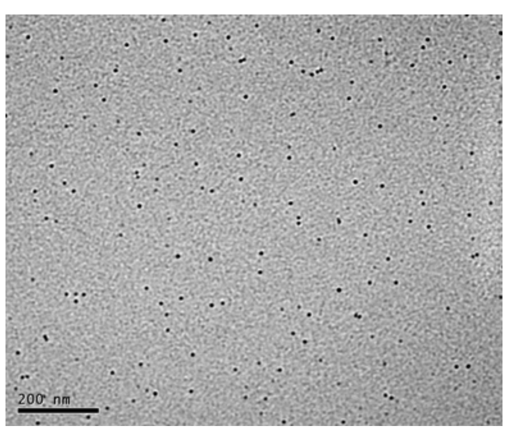


**Figure 6.9 TEM image of $TiO_2$ nanoparticles suspended in water.**

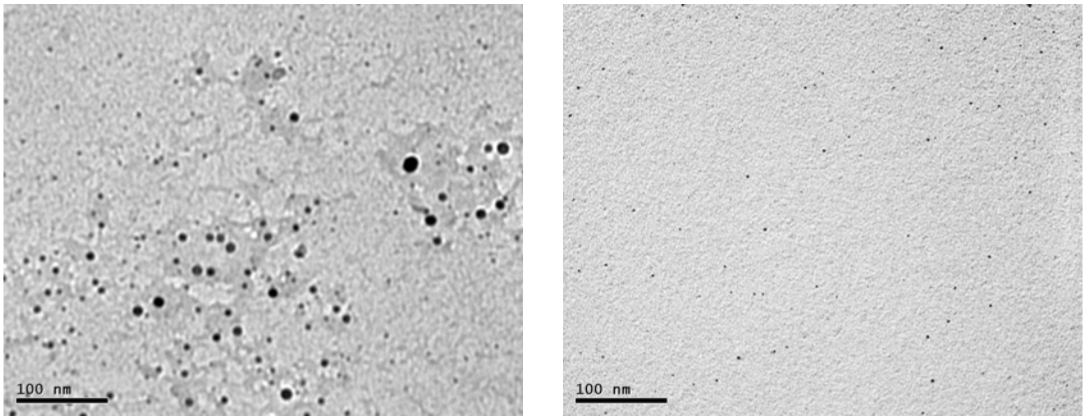


**Figure 6.10 A. $TiO_2$ functionalized with $[4,4'\text{-}(LL)]_2Ru(Cl)_2$ B. $TiO_2$ with Streptavidin**

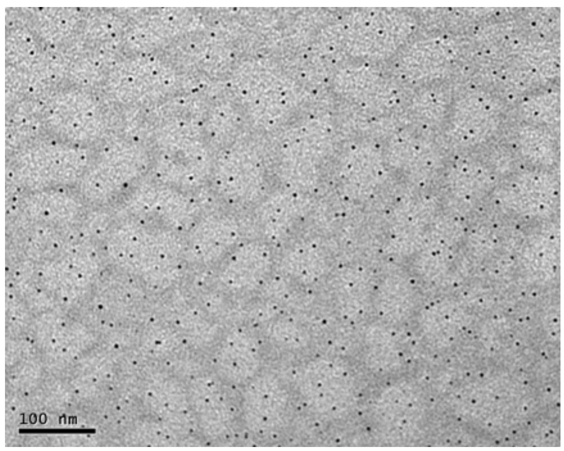


**C. $TiO_2$ functionalized with Streptavidin and $[4,4'\text{-}(LL)]_2Ru(Cl)_2$**

image in Figure 6.10 A. But when colloidal solution of $TiO_2$ was incubated at room temperature with 100 ul streptavidin (1.4 mg/ml) and 100 ul of 1 mM $[4,4'\text{-}(LL)]_2Ru(Cl)_2$ for 30 min and then the excess was separated by centrifuging in a microcon (30 KDa MWC) at 14,000 RPM for 10 min it resulted in monodisperse and small $TiO_2$ nanoparticles as seen in Figure 6.10c. The UV-Vis spectra of this step by step process are shown in Figure 6.11. These nanoparticles were then used as labels for photoelectrochemical detection of DNA hybridization

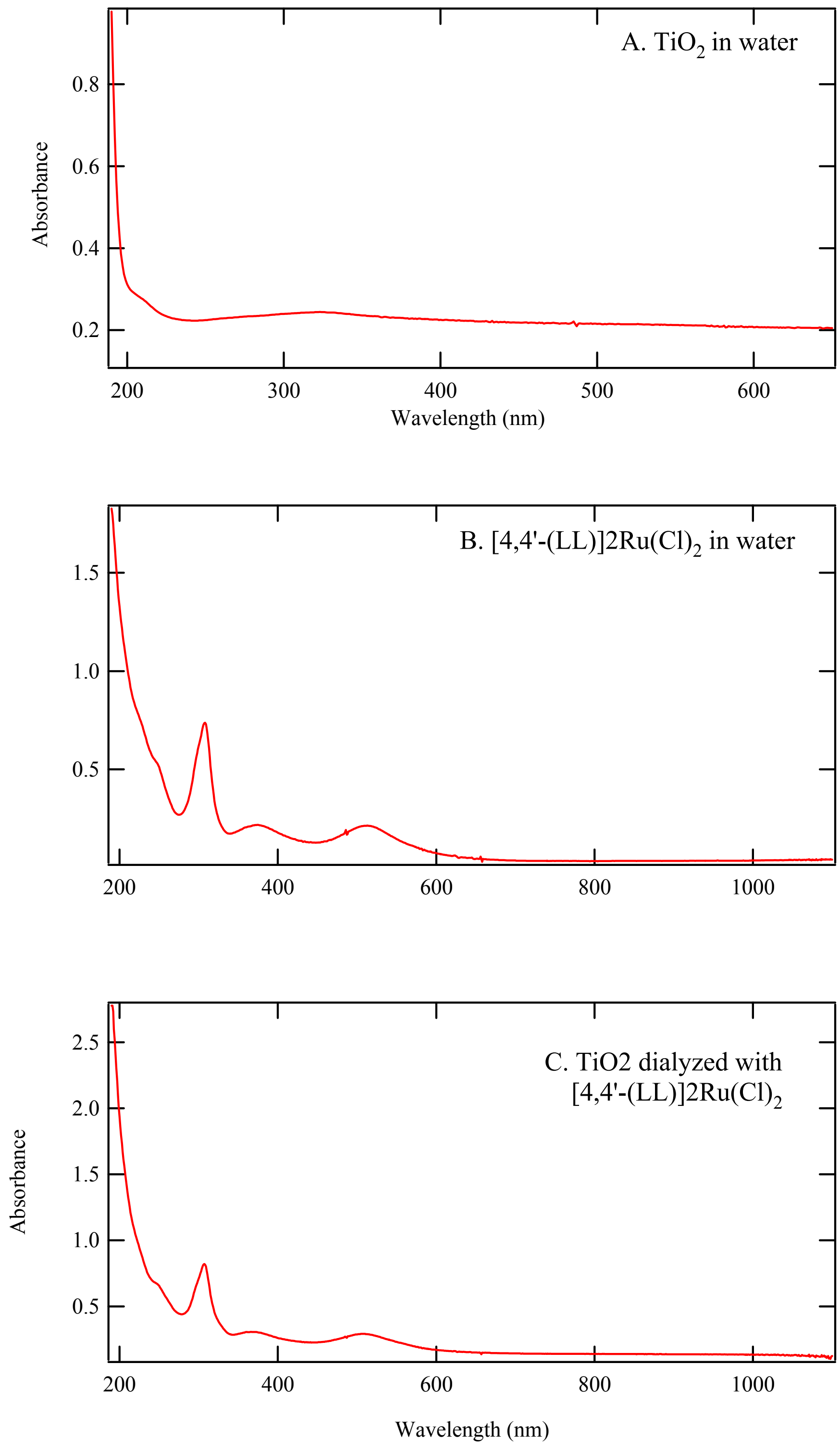
A. $TiO_2$ in water
Absorbance
0.2
0.4
0.6
0.8
200
300
400
500
600
Wavelength (nm)
B. [4,4'-(LL)]2Ru$(Cl)_2$ in water
0.5
1.0
1.5
200
400
600
800
1000
C. TiO2 dialyzed with
[4,4'-(LL)]2Ru$(Cl)_2$
Absorbance
0.5
1.0
1.5
2.0
2.5
200
400
600
800
1000
Wavelength (nm)

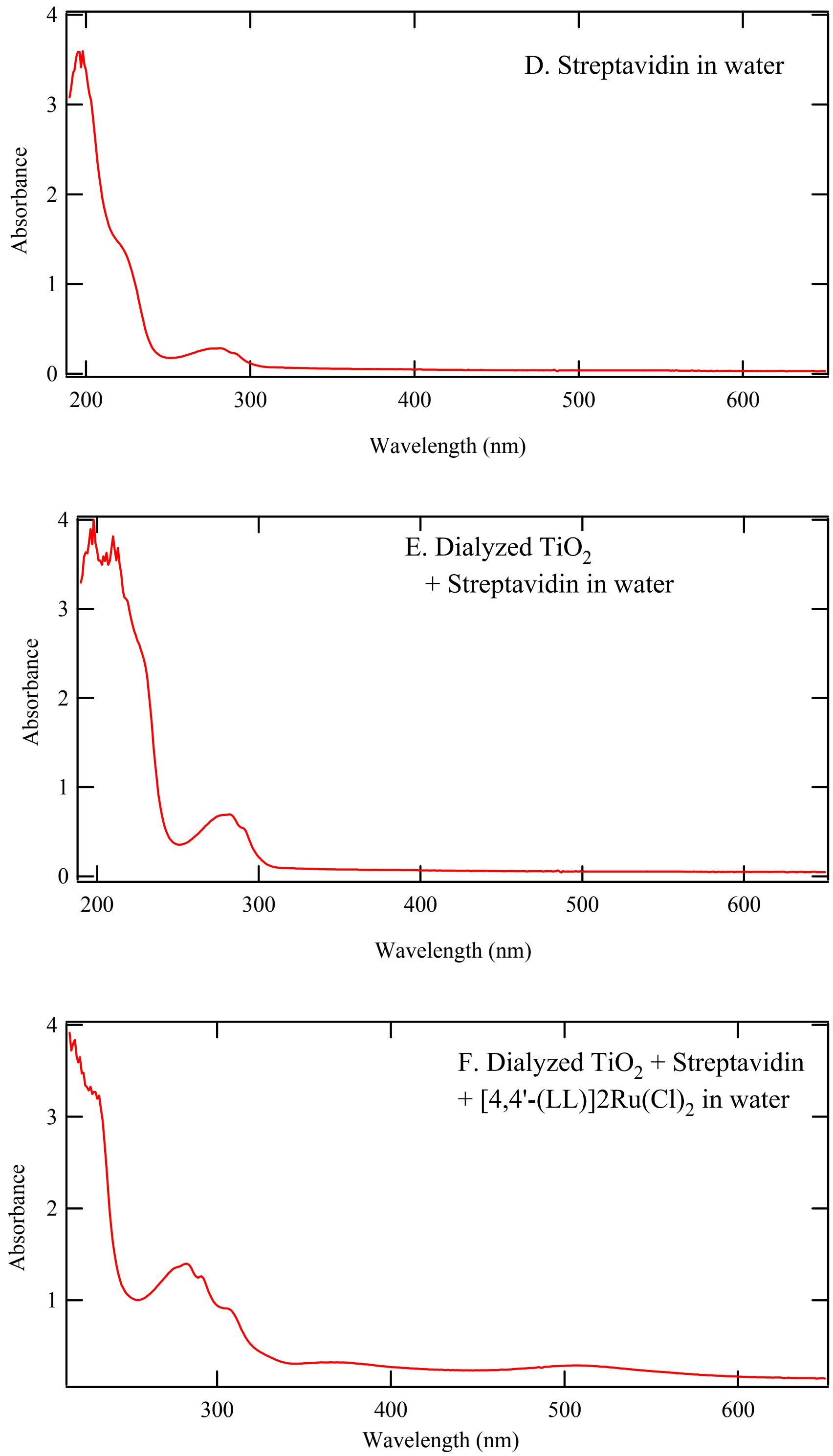


**Figure 6.11 UV-Vis spectra of strepatavidin and $[4,4'\text{-}(LL)]_2Ru(Cl)_2$ stabilized $TiO_2$ nanoparticles**

The $TiO_2$ particles functionalized with Streptavidin and $[4,4'\text{-}(LL)]_2Ru(Cl)_2$ though monodisperse, tend to aggregate when in contact with ITO surface. Repeated experiments to get an estimate of surface coverage of $TiO_2$ particles on ITO surface by AFM and SEM were unsuccessful. The SEM image of $TiO_2$ particles is shown in Figure 6.13.

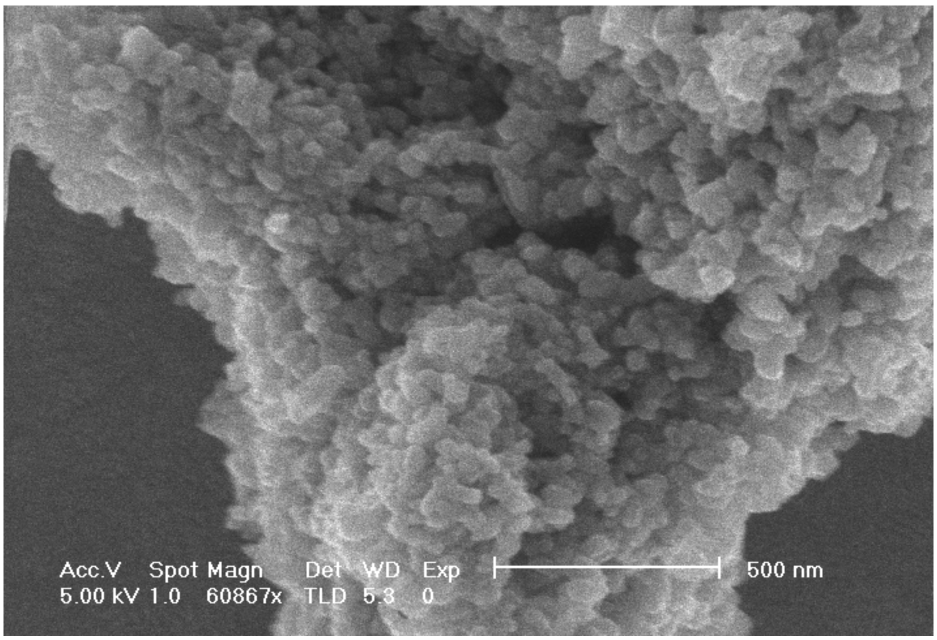


**Figure 6.12 SEM image of $TiO_2$ nanoparticles**

### 6.2.4.2 The Microarray Design

With all the components for creating a biosensor using the well known biotin-streptavidin interaction worked out, the final step is creating the DNA microarray and detecting the hybridization photoelectrochemically.

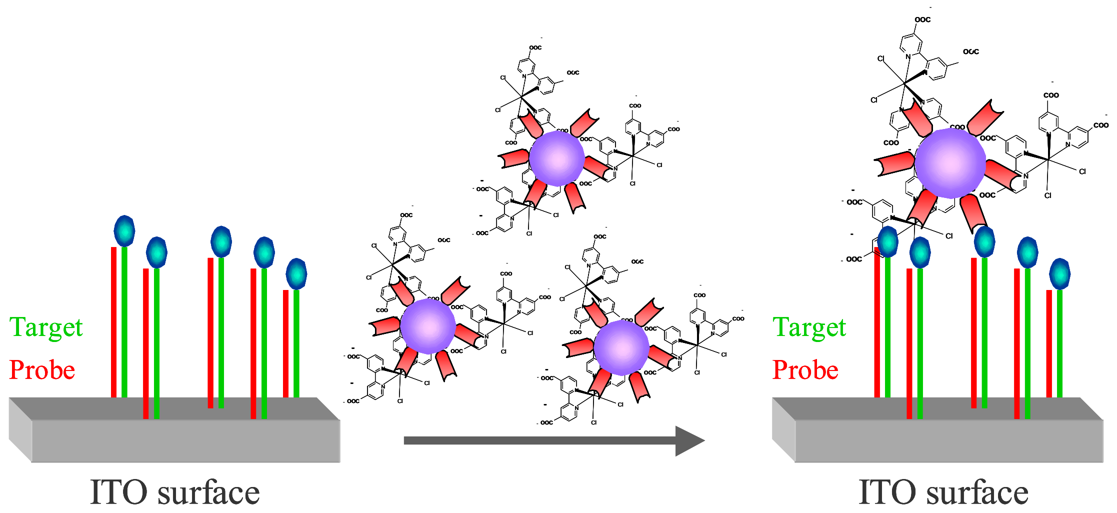


**Scheme 6.4 ITO substrate modified with ssDNA hybdridzed to a biotin labeled compliment and exposed to Streptavidin and [4,4'-(LL)]$_2$Ru(Cl)$_2$ coated by TiO$_2$ nanoparticles.**

Streptavidin is a tetrameric protein isolated from *Streptomyces avidinii*, and can bind to biotin, a vitamin ligand. The binding affinity is very high (Kd ~ $10^{-15}$ M for unlabelled biotin and streptavidin) and the protein is very stable at normally denaturing conditions like pH, temperature etc. High affinity in combination to binding capacity, reproducibility and chemical resistance makes it an ideal system in biosensor technology for immobilizing DNA.[32]

1cm$^2$ ITO substrates were cleaned using ozonolysis and modied with 12-PDA. EDC coupling reaction bound the amine terminated probe DNA to the –COOH group of the 12-PDA on the ITO surface. Subsequently the ITO substrate modified with probe DNA and hybridized with a compliment target with a 5' –Biotin label was exposed to the solution containing TiO$_2$ nanoparticles functionalized with [4,4'-(LL)]$_2$Ru(Cl)$_2$ and streptavidin for 2-3 hours. Photoelectrochemistry and XPS were employed to detect the hybridization event.

### 6.2.4.3 Experimental Setup Photoelectrochemistry (PEC)

The $TiO_2$ nanoparticles functionalized and stabilized with streptavidin and Ru complex was prepared as mentioned in section 6.2.4.1.2. The probe on ITO surface upon hybridization with the labeled target makes a conjugate such that $[Ru(bpy)_3]^{2+}$ will be present in the duplex system. The light source used to excite the $[Ru(bpy)_3]^{2+}$ molecule was a Ti:Sapphire laser with a doubling crystal which lases from 360 nm - 500 nm. The power of the blue light was 15 mW. The optical and working window has an area of 0.38 $cm^2$. The reference electrode used for the measurements was an Ag/AgCl while Pt served as the counter electrode for all the photoelectrochemical experiments. The electrolyte was 0.1M aqueous potassium phosphate (pH 7.2) and sacrificial electron donors EDTA, TPA, TEA and sodium oxalate were used to probe a variety of redox potentials. The voltage was stepped up from 0 to a higher potential ranging from 0.5 V-0.7 V. The photoelectrochemical cell was connected to an EG&G Princeton Applied Research Potentiostat Model 273A Instrument as shown in Figure 6.13.

The important factors in designing a dye sensitized photoelecrochemical system are, the dye, the sacrificial donor and the potential at which experiments will be carried out. In a photoelectrochemical measurement the ITO substrate modified with DNA will be held at a constant potential and the current monitored. Feldheim *et al.* [8] have reported a presence of current when the sample is not being illuminated by the light source. This is referred to as dark current. The sacrificial donor affects the dark current to some degree. If the oxidation potential of the electron donor is less than the potential used for PEC experiment, the electron donor at the electrode surface will undergo an oxidation causing an anodic current. At concentration 50 mM, EDTA dark current reduces within the first second when gold is the working electrode.

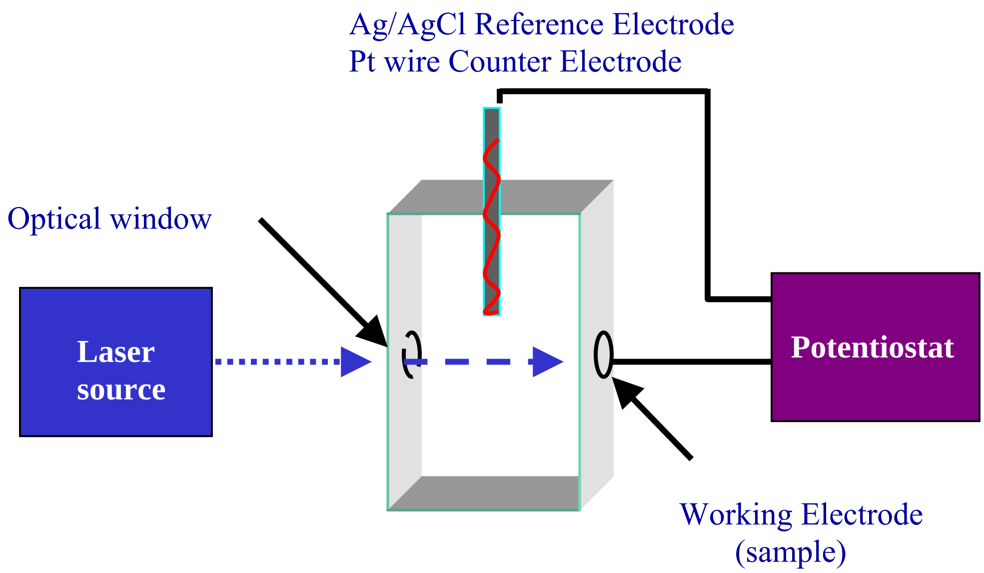


**Figure 6.13. Experimental setup for Photoelectrochemistry.**

The main objective of the experiments would be to increase the photocurrent efficiency. Lower photocurrent efficiency observed in the previous studies on is partly due to less efficient electron transfer to the $TiO_2$ surface. The factors like light harvesting efficiency, electron collection efficiency were studied in detail to increase the sensitivity of photoelectrochemical detection system.

XPS and photoelectrochemical analyses were performed on ITO substrates modified with an amine terminated DNA, exposed to its biotinylated compliment target and then exposed to a solution of $TiO_2$ nanoparticles functionalized with streptavidin and $[4,4'\text{-(LL)}]_2Ru(Cl)_2$. XPS results showed that the streptavidin-biotin interaction was not taking place since presence of Ru and Ti was not detected. When photoelectrochemistry was applied to the same set of samples the photocurrent enhancement was not detected either. Hence a systematic study was carried out to determine the factors like the distance of semiconductor particles from electrode surface, effect of linker molecule in electron kinetics and the need of an electron mediator that were important to obtain a photocurrent.

### 6.2.4.3.1 Effect of sacrificial donor on photocurrent

To enhance the electrochemical signal chemical and biological modifications are used. Enzymes can be used for many applications in biological systems to amplify the signal [33] but they are bulky and unstable. To chemically enhance the signal a sacrificial electron donor is used in addition to the electrolyte solution. On adding the sacrificial electron donor, the signal is still from the photoelectrochemical label but it is regenerative and amplified. Scheme 6.5 shows the reaction sequence. The sensitizer molecule [4,4'-(LL)]$_2$Ru(Cl)$_2$ photoexcited and injects its electron into the conduction band of the semiconductor nanoparticle. The [4,4'-(LL)]$_2$Ru(Cl)$_2$ molecule is regenerated or reduced to its original redox state by an electrolyte in solution that diffuses to the gold counter electrode. If the sacrificial donor gets directly oxidized at the electrode surface it can give rise to a large background signal.

1. Label oxidation: $\text{Label} \longrightarrow \text{Label}_{(ox)}$
2. Label Regeneration: $\text{Label}_{ox} + e^{-}\ \text{donor} \longrightarrow \text{Label}_{red}$
3. Label Re-oxidation: $\text{Label}_{red} \longrightarrow \text{Label}_{ox}$

**Scheme 6.5 Reaction mechanism of chemically amplified electrochemical detection.**

Hence its important to study and find an electron donor that can amplify the signal and minimize the background current. In the applications of the Graetzel cell, the conversion efficiency of solar energy is the key factor and the sacrificial donor used for those applications is the $I^-/I_2$ system. $I^-/I_2$ is a very strong reagent and damages the gaskets in the electrochemical cell, hence was not a desirable sacrificial donor. Various sacrificial donors like Tripropyl amine (TPA), triethylamine (TEA), sodium oxalate and EDTA were tried. As replacements for the triiodide/iodide redox pair. While TPA exhibited a high background current.(data not shown). EDTA, TEA and Sodium oxalate exhibited a low background current in the potential of interest and the background current for EDTA increases at potentials above 1 V as shown in Figure 6.14. The redox potentials of EDTA, TEA, $I^-/I_2$ and sodium oxalate are given in Table 6.1.

| Sacrificial Donor | $E_{Ag/AgCl}$ (V) |
|---|---|
| **EDTA** | 0.75 |
| TEA | 0. 90 |
| $NaI/I_2$ | 0.54 |
| Sodium oxalate | 1.1 |

**Table 6.1 Redox potentials of sacrificial electron donor used for PEC studies**

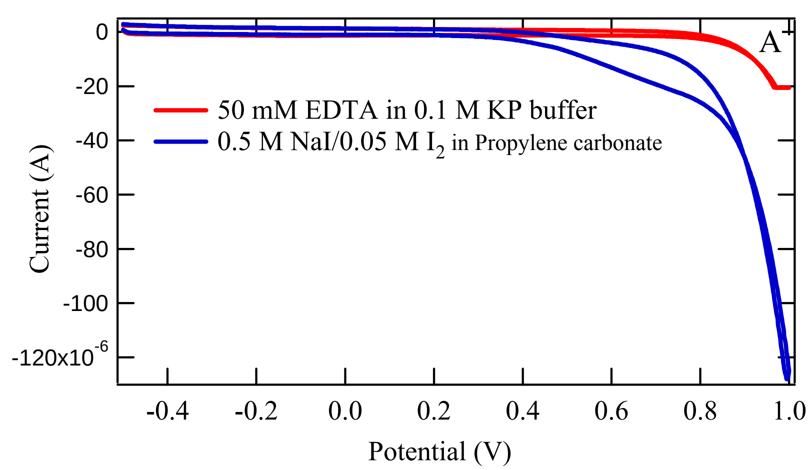

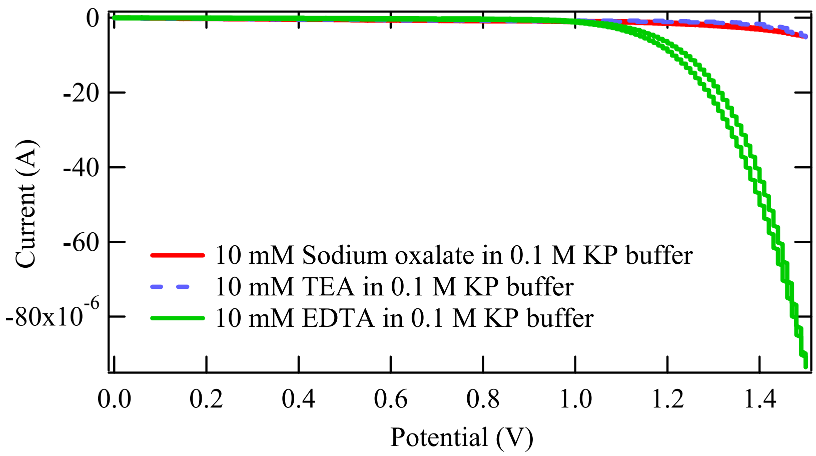


**Figure 6.14 Cyclic voltamograms of (A)electron donors I/I2 and EDTA (B) Sodium oxalate, TEA and EDTA in supporting electrolyte Sodium or Potassium Phospahte Buffer on bare ITO substrate.**

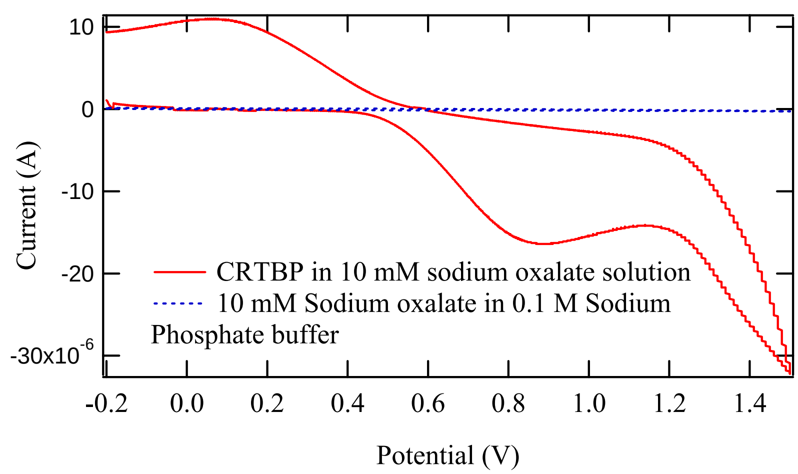


**Figure 6.15 Cyclic voltamogram of 1 M [4,4'-(LL)]$_2$Ru(Cl)$_2$ in sodium oxalate at pH 5.5 on bare ITO electrode.**

To understand the kinetics of electron transfer and distance dependence of the analyte, the basic Graetzel cell was studied. A paste of $TiO_2$ particles in Triton X was made. It was uniformly mixed in a mortar and pestel and applied onto an ITO substrate leaving two edges uncoated for electrical conductivity. This substrate was then baked in an oven at for 1 hr and then stored in a dessicator for further use.

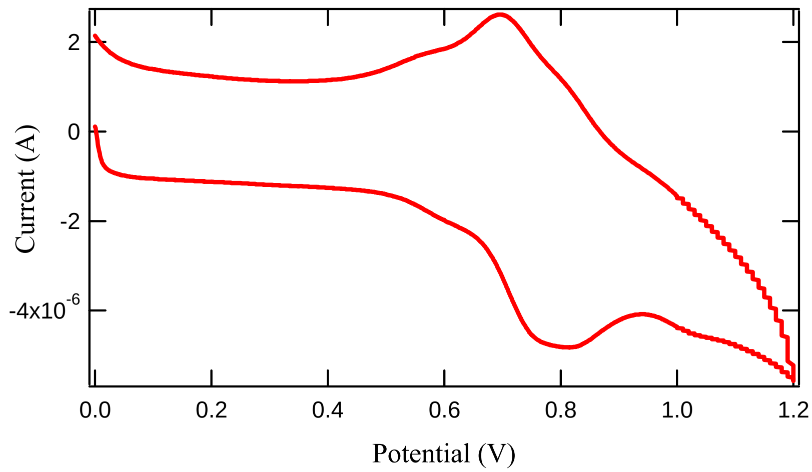

**Figure 6.16 Cyclic voltamogram of 1uM [4,4'-(LL)]$_2$Ru(Cl)$_2$ adsorbed on $TiO_2$ particles sintered onto an ITO substrate**

.

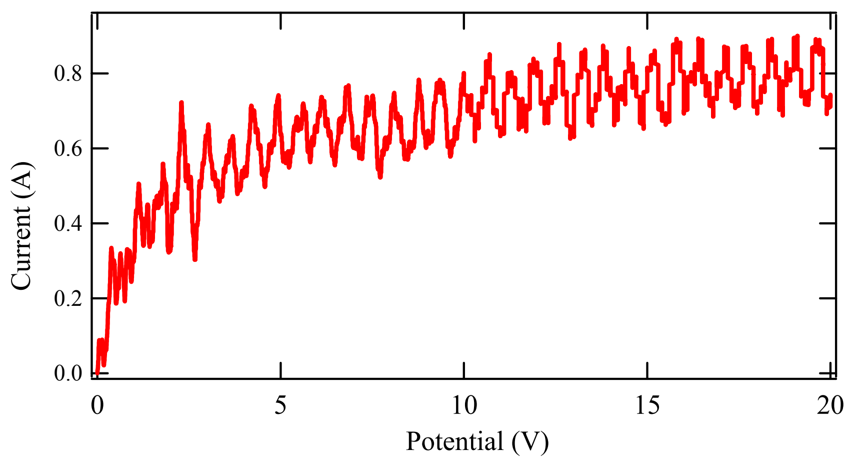


**Figure 6.17 Photocurrent from 1uM [4,4'-(LL)]$_2$Ru(Cl)$_2$ adsorbed on $TiO_2$ particles sintered onto an ITO substrate. The electron donor is an Iodine system in propylene carbonate.**

As mentioned earlier in this section, the Iodine-triiodide system was a strong oxidant and destroyed the gaskets in the electrochemical cell hence was not used for further experiments.

### 6.2.4.3.2 Effect of voltage on photocurrent

The voltage to which the potential is stepped up in a photoelectrochemical experiment affects the measured photocurrent. Hence, photocurrent as a function of applied voltages ranging from 500 mv to 1 V were recorded for $TiO_2$ functionalized with [4,4'-(LL)]$_2$Ru(Cl)$_2$ on deposited on ITO substrate.. Sacrificial donor is 50 mM EDTA in 0.1 M KP buffer.as shown in Figure 6.18. The light was chopped manually at a frequency of 0.2 Hz. The other experimental conditions were as mentioned before. 0.1M aqueous potassium phosphate (pH 7.2) was the electrolyte and 50 mM EDTA was the sacrificial electron donor. An expected exponential increase in the photocurrent with increase in applied voltage reported by Feldheim etal [7] is not observed in Figure 6.18.

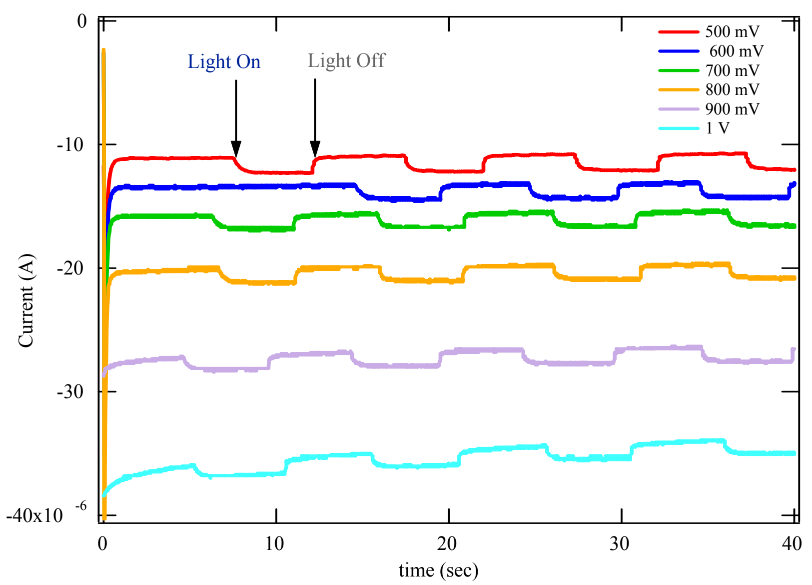


**Figure 6.18 Photocurrent from $TiO_2$ functionalized with [4,4'-(LL)]$_2$Ru(Cl)$_2$ on ITO substrate at different applied potentials. Sacrificial donor is 50 mM EDTA in 0.1 M KP buffer.**

To study the effect of increase in photocurrent with increase in concentration of the photoactive species i.e $TiO_2$ nanoparticles functionalized with [4,4'-(LL)]$_2$Ru(Cl)$_2$, slides with three different concentration of the [4,4'-(LL)]$_2$Ru(Cl)$_2$ functionalized $TiO_2$

nanoparticles were prepared. The photoelectrochemistry was performed as reported

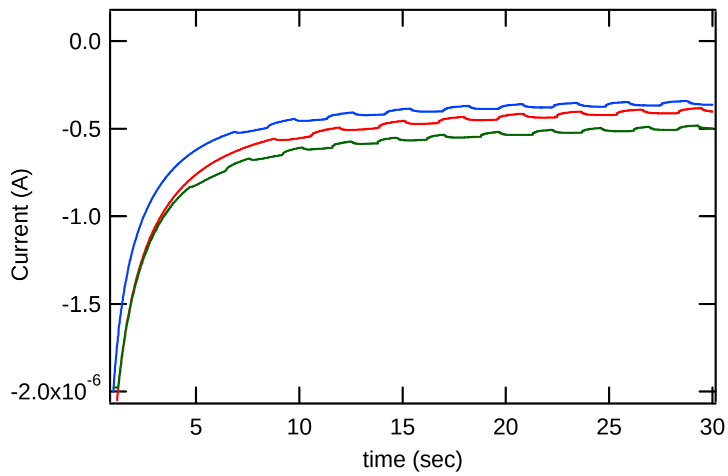


**Figure 6.19 $TiO_2$ functionalized with [4,4'-(LL)]$_2$Ru(Cl)$_2$ on ITO substrate at different concentrations. The green curve corresponds to the lowest concentration and the blue curve corresponds to the highest concentration of functionalized nanoparticles.**

in the earlier section.

The power from the laser was 15 mW and the electrolyte used was 0.1M aqueous potassium phosphate (pH 7.2) with 50 mM EDTA as the sacrificial electron donor. The potential was stepped up from 0 to 0.5 V and held constant at 0.5 V vs Ag/AgCl while the photocurrent as a function of time was observed. The photocurrent did not increase with increase in concentration $TiO_2$ nanoparticles labeled with [4,4'-(LL)]$_2$Ru(Cl)$_2$. Though ITO background did not give rise to any photocurrent the photocurrent from all three samples were 10 nA.

### 6.2.4.3.3 Effect of electron mediator on Photocurrent

To enhance the photoelectrochemical signal for biomolecule detection enzymes are used as labels. As one enzyme molecule is capable of catalyzing thousands of substrates, there is inherent amplification. The large size of the enzymes and its instability limits its usage. Use of a sacrificial donor in the electrolyte solution for a photoelectrochemical process causes amplification of the signal, as the photoredox label - $[4,4'\text{-}(LL)]_2Ru(Cl)_2$ gets oxidized at the semiconductor surface, it gets reduced by the electron donor in the electrolyte. The regenerated label participates in the photoelectrochemical cycle again. As one electron is cycled over and the photoelectrochemical reaction continues, it can be referred to as signal amplification since more than one electron is extracted from the same label. Zheng etal[34] studied optimal combination of analyte and sacrificial electron donor for phoelectrochemical detection. Sodium oxalate was tested as an electron donor to amplify the signal of Ru-bipy on ITO substrate. Cyclic voltametry of 5 uM $[4,4'\text{-}(LL)]_2Ru(Cl)_2$ in the presence and absence of 10 mM sodium oxalate in 0.1 M sodium phosphate buffer was studied. The current in the presence of oxalate was approximately 50 times that of $[4,4'\text{-}(LL)]_2Ru(Cl)_2$ alone. [26] This large increase in anodic current was from the reaction between oxidized Ru-bipy and oxalate. Hence, sodium oxalate was used as the sacrificial donor to increase the photocurrent. In the cyclic voltamogram (Figure 6.15) a large anodic current is seen from the reaction of oxidized $[4,4'\text{-}(LL)]_2Ru(Cl)_2$ and oxalate in the electrolyte. Nevertheless, when a photoelectrochemical measurement was performed on an ITO substrate coated with dye sensitized $TiO_2$ in the presence of sodium oxalate the photocurrent did not increase as shown in Figure 6.20. The measured photocurrent is 11 nA in the presence and absence of EDTA. When 10 μM Ruthenium hexamine was introduced in the electrolyte solution containing the sacrificial donor sodium oxalate or EDTA to act as an electron mediator, there was no increase in photocurrent.

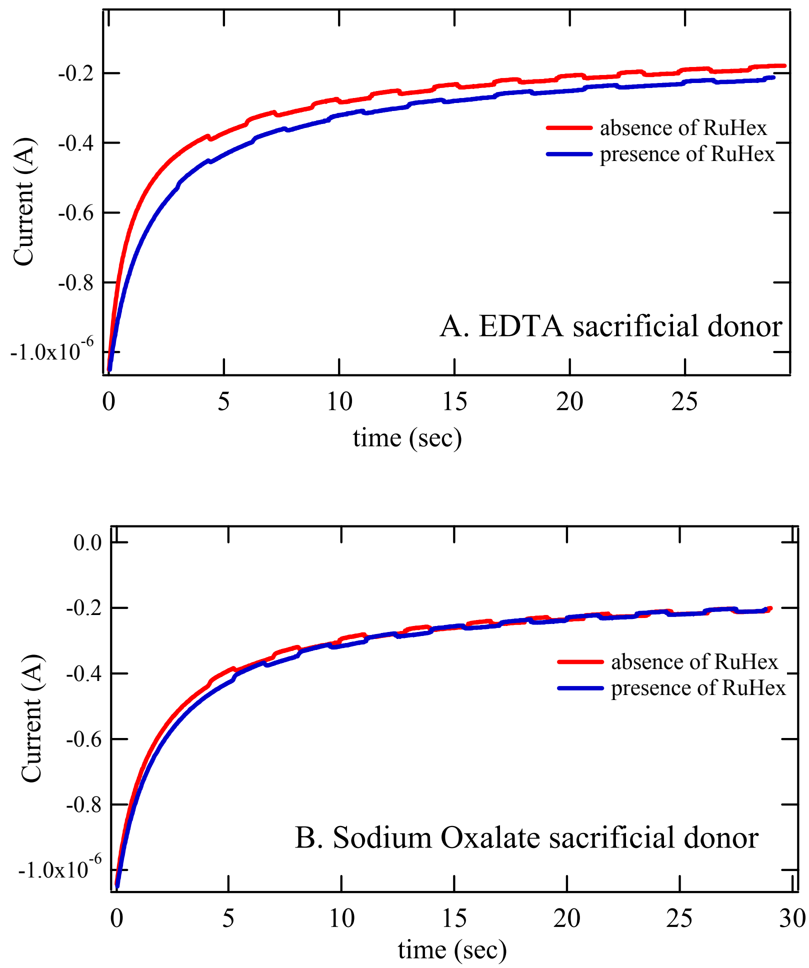


**Figure 6.20. $TiO_2$ functionalized with $[4,4'\text{-(LL)}]_2Ru(Cl)_2$ on ITO substrate. A. Sacrificial donor 10 mM EDTA in 0.1 M KP buffer at pH 7.5 B. Sacrificial donor 10 mM Sodium oxalate in 0.1 M KP buffer at pH 5.5**

Willner *e tal*. reported photocurrent from Au and CdS nanoparticles arrays integrated with photosensitizer on ITO substrates.[30,35,36] An interesting photoelectrochemical study on photosensitizer molecular cross-linked Au-nanoparticle arrays assembled on ITO substrates was reported recently. One of the cross-linker molecules is Ru(II)-tris-(2,2'-bipyridine)-cyclobis(paraquat-p-phenylene) catenane (R). The electrode functionalized with R was used in photoelectrochemical experiments with a graphite counter electrode and 0.1 M $Na_2EDTA$ in 0.1 M phosphate buffer, pH 7.2. The photocurrent increased with increase in thickness of the cross-linked Au layer. When photocurrent was measured as a function of bias potentials, the current increases when the applied potential ia greater than –0.6 V at which the bipyridinium sites are reduced, and the photoinduced electron transfer in the photosensitizer-electron acceptor dyad is prohibited blocking the photocurrent. Applied voltage is one of the important factors determining the photocurrent efficiency.

Recently Grätzel etal synthesized a stable and efficient Ruthenium complex called K-19. [15] The cathodic and anodic peaks for K-19 in DMF appear at 0.95 V vs normal hydrogen electrode (NHE). The redox potential of K-19 is 0.41 V higher than that of $I^-/I_2$ vs NHE [16] providing ample driving force for efficient dye regeneration resulting in a net charge separation. The excited state redox potential, $\phi^0(S^+/S^*)$ of K-19 is calculated to be –0.75 V vs NHE which is more negative than that of the conduction band edge of $TiO_2$ providing thermodynamic driving force for electron injection.[15]. Since the redox potential of the dye used $[4,4'\text{-(LL)}]_2Ru(Cl)_2$ is 0.79 V, $NaI/I_2$ is the only sacrificial donor with redox potential lower than that of $[4,4'\text{-(LL)}]_2Ru(Cl)_2$ for dye regeneration. Since $NaI/I_2$ is not easy to work with and it dissolves the sealants used in the electrochemical cell other sacrificial donors with low redox potentials have to be explored which can be used with the same dye molecule $[4,4'\text{-(LL)}]_2Ru(Cl)_2$ or a new dye molecule needs to be synthesized which would have a more positive redox potential than the well studied sacrificial donor like EDTA which is biocompatible.

## *6.2 Quartz Crystal Microbalance (QCM) – a tool for detection light addressable biological sensor*

### 6.2.1 General Introduction to QCM

Quartz Crystal Microbalance (QCM) is a sensitive device to detect mass changes at the QCM electrode surface. Sauerbrey [37] in 1951 related the mass change per unit area at the QCM crystal surface to the observed change in oscillation frequency of the crystal as shown in equation 6.1

$$\Delta f = -C_f \cdot \Delta m \qquad 6.1$$

where

$\Delta f$ = the observed frequency change in Hz

$\Delta m$ = the change in mass per unit area in g/cm2,

$C_f$ = the sensitivity factor for the crystal

As Sauerbrey equation relies on $C_f$, the fundamental property of the QCM crystal, theoretically QCM mass sensor does not require calibration. This equation holds true only for uniform and rigid thin films. Though initial application for QCM was a gas-phase mass detector, recently QCM's have been used in contact with fluids for applications in electrochemistry and microrheology. Due to the piezoelectric properties of the quartz, a voltage applied across the electrodes leads to a shear deformation of the quartz crystal. The fundamental frequency of a quartz crystal resonator is dependant upon its own material properties and the properties of the associated metal electrodes. The fundamental frequency shift may occur due to contributions from: (1) the mass loading on the electrode surfaces, (2) the properties (i.e., density and viscosity) of the fluid in contact with the wafer, in addition to (3) the temperature and pressure of the crystal environment. The absolute temperature limit for the QCM measurements is the Curie point of quartz (573 °C); the point at which the piezoelectric properties disappear.

In the present study QCM is employed as a sensor to simultaneous measure frequency change on as a function mass and temperature. Laser induced temperature jumps (LITJ's) from very Au nanoparticles on the surface of ITO have been reported by Feldheim etal. This temperature jump that occurs when laser (532 nm) is shone on Au coated ITO substrate in combination with QCM to detect change in frequency as a function of mass is an inexpensive device.in comparison to the IR camera's used currently to monitor change in surface temperature for LITJ's. Direct measurement of temperature increase, mass change and other mechanical changes could be used to derive kinetic and thermodynamic information. QCM/LITJ's can be used to measurement of sensitive biological systems since the analyte can be detected with three measurable parameters.

## *6.2 Methods and Instrumentation*

QCM measurements were performed on a QCM 200 digital controller and QCM 25 crystal oscillator using indium tin oxide (ITO) crystals (5 MHz, AT-cut) from Stanford Research Systems (SRS). The diameter of the ITO crystal was 1 inch.

The crystals were cleaned with ethanol and dried in a stream of Nitrogen gas before the Au nanoparticle solution of required concentration was evaporated on it. The crystal was mounted on the holder and a modified flow cell adapter built in house secured the crystal in the holder. The inlet and outlet ports allowed solvent exchange through a thermostat controlling the temperature and a thermocouple wire was sealed inside the cell to monitor temperature change.

**Figure 6.21 Temperature controlled QCM setup**

## *6.3 Results and Discussion*

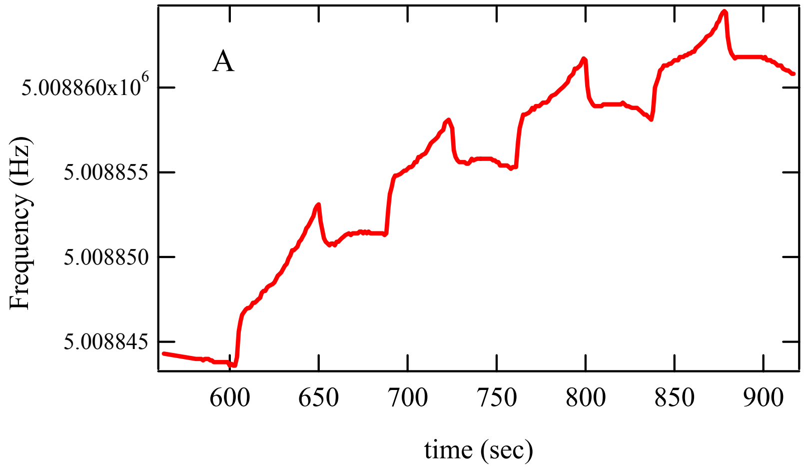

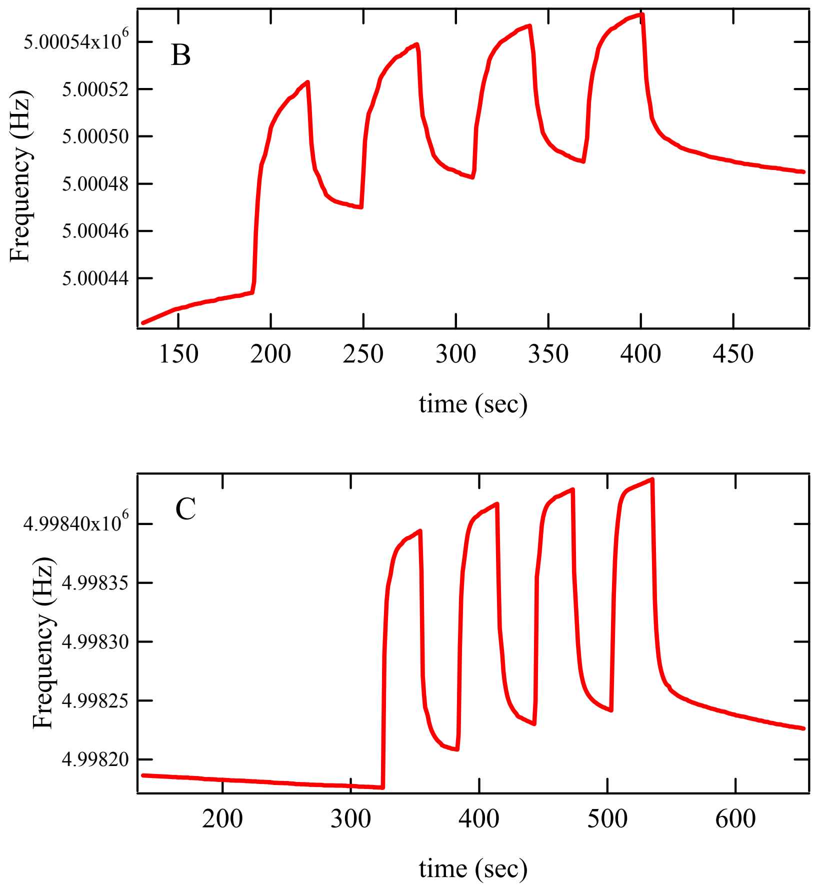


**Figure 6.22 Frequency as a function of time on a ITO crystal**

The change in frequency of the QCM crystal evaporated with citrate stabilized Au nanoparticles at various concentrations are shown in Figure 6.22 (only three examples). The sample was irradiated with a 532 nm wavelength light. The frequency of the QCM crystal increased when the Au nanoparticles were heated. The change in frequency as a function of concentration of the Au nanoparticles shows a linear trend.

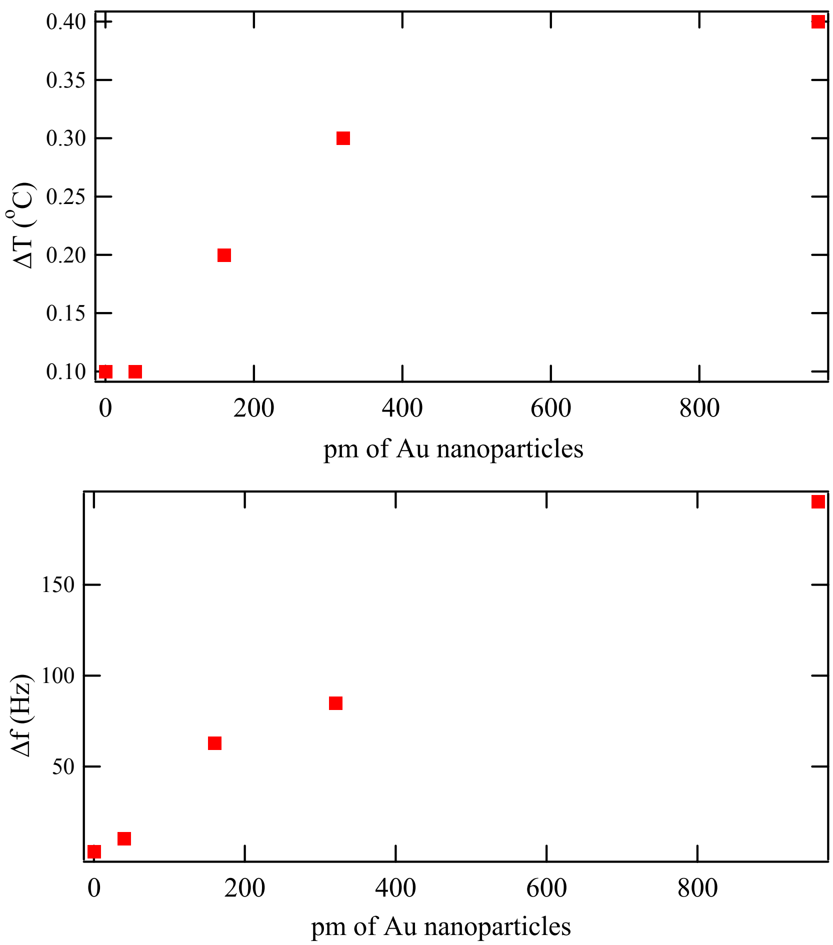


**Figure 6.23 Change in temperature (A) and frequency (B) as a function of concentration of Au nanoparticles on the ITO crystal**

The Laser induced temperature jump ΔT also increases with increase in concentration of the Au nanoparticles deposited on the surface of the ITO crystal. Since the temperature jump could arise from the QCM crystal itself, ITO coated crystal was used as a blank to be subtracted from the Laser induced temperature jump from the Au nanoparticle coated ITO crystal electrode.

This experiment was carried out as a proof of principle to estimate the sensitivity of the heating effect of nanoparticles and detection limit. As picomoles of nanoparticles were detected by QCM/LITJ's it definitely has potential to be used as a biosensor for detecting DNA hybridization by colloidal labeling and also detecting viruses and antibody binding on surfaces.

## Acknowledgements

We thank Dr. Paul A. Maggard , NCSU for the fruitful discussions regarding Titanium dioxide nanoparticle synthesis.

## References

1. Dong Dong, D.Z., Fu-Quan Wang, Xi-Qiang Yang, Na Wang, Yuan-Guang Li, Liang-Hong Guo, Jing Cheng, *Quantitative Photoelectrochemical Detection of Biological Affinity Reaction: Biotin-Avidin Interaction.* Anal. Chem., 2004. **76**: p. 499-501.
2. Campbell, A.K., *Chemiluminescence: Principles & Applications in Biology & Medicine*. 1988, Chichester (England): Ellis Harwood Ltd.
3. Xiao-Hong Xu, H.C.Y., Thomas E. Mallouk, Allen J. Bard, *Immobilization of DNA on an Aluminum(III) Alkanebisphosphonate Thin Film with electrogenerated Chemiluminescent Detection.* J. Am. Chem. Soc, 1994. **116**: p. 8386.
4. Lynn Dennany, R.J.F., James F. Rusling, *Simultaneous Direct Electrochemiluminescence and Catalytic Voltammetry Detection of DNA in Ultrathin Films.* J. Am. Chem. Soc, 2003. **125**(17): p. 5213.
5. Yamada, S.K., Y.; Matsuo, Y., J. Electroanal. Chem., 1997. **426**: p. 23-26.
6. Koide, Y.T., N.;Akiyama, Y.; Yamada, S., Thin solid Films, 1999. **350**: p. 223-227.
7. Lowe, L.B., *Synthesis and characterization of a dye sensitizing molecule for photoelectrochemical DNA hybridization detection*, in *Chemistry*. 2002, North Carolina State University: Raleigh.
8. Lowe, L.B.B., S. H.; Kramer, S.; Fuierer, R. R.; Qian, G.; Agbasi-Porter, C. O.; Moses, S.; Franzen, S.; Feldheim, D. L., J. Am. Chem. Soc.(Communication), 2003. **125**(47): p. 14258-14259.
9. Moses, S., et al., *Characterization of single- and double-stranded DNA on gold surfaces.* Langmuir, 2004. **20**(25): p. 11134-11140.
10. Brian, O., Gratzel, M., Nature, 1991. **353**: p. 737.
11. Honda, K., Fujishima, A., Nature, 1972. **238**: p. 37.
12. Gerischer, H., Photochem. Photobiol., 1972. **16**: p. 243.
13. Matsumura, M., Nomura, Y., Tsubomura, H., Bull. Chem. Soc. Japan, 1977. **50**: p. 2533.
14. Alonso, N., Beley, V. M., Chartier, P., Ern, V., Rev. Phys. Appl., 1981. **16**(5).

15. Wang, P., Klein, C., Humphry-Baker, R., Zakeeruddin, S. M., Gratzel, M., *A High Molar Extinction Coefficient Sensitizer for Stable Dye-Sensitized Solar Cells.* J. Am. Chem. Soc, 2005. **127**(3): p. 808.
16. Bard, A.J., Faulkner, L. R., *Electrochemical methods: Fundamentals and Applications*. 2 ed. 2001: Wiley.
17. Spivey, D.D.E.a.D.I., Faraday Soc. Trans., 1962. **58**: p. 411.
18. Barton, S.O.K.a.J.K., Chem. Biol., 1998. **5**: p. 413.
19. E. Meggers, M.E.M.-B.a.B.G., J. Am. Chem. Soc, 1998. **120**: p. 12950.
20. Steenken, S.J., S. V., J. Am. Chem. Soc. (Communication), 1997. **119**(3): p. 617-618.
21. Glese, B., Amaudrut, J., Kohler, A.-K., Spormann, M., and Wessely, S., Nature, 2001. **412**: p. 318-320.
22. Hagfeldt, A.G., M., Chem. Rev., 1995. **95**: p. 49.
23. Argazzi, R.B., C. A.; Heimer, T. A.; Castellano, F. N.; Meyer, G., J. Inorg. Chem., 1994. **33**: p. 5741.
24. Kolen'ko, Y.V.B., A.A.; Churagulov, B. R.; Oleynikov, N. N., Mater. Lett., 2003. **57**: p. 1124.
25. Baraton, M.-I., *Synthesis, Functionalization and Surface Treatment of Nanoparticles*. 2003: American Scientific Publishers.
26. Robert Argazzi, C.A.B., Todd A. Heimer, Felix N. Castellano, Gerald J. Meyer, Inorg. Chem., 1994. **33**(25): p. 5741-5749.
27. Frey, B.L.C., R. M., Analytical Chemistry, 1996. **68**: p. 3187-3193.
28. Kerman, K.O., D.; Kara, P.; Meric, B.; Gooding, J. J.; Ozsoz, M., Analytica Chimica Acta, 2002. **462**: p. 39-47.
29. Burgener, M.S., M.; Candrian, U., Bioconjugate Chemistry, 2000. **11**: p. 749-754.
30. Huang, E.Z., F. M.; Deng, L., Langmuir, 2000. **16**: p. 3272-3280.
31. Hermanson, G.T., *Bioconjugate Techniques*. 1996: Academic Press: San Diego.
32. Su, X.W., Y.-J.; Robelek, R.; Knoll, W., Langmuir, 2005. **21**(1): p. 348-353.
33. T. de Lumley-Woodyear, C., C. N., Freeman, E., Freeman, A., Georglou, G., Heller, A., Anal. Chem., 1999. **71**: p. 535.
34. Dong Zheng, N.W., Fu-Quan Wang, Dong Dong, Yuan-Guang Li, Xi-Qiang Yang, Liang-Hong Guo, Jing Cheng, *Sensitive chemically amplified electrochemical detection of ruthenium tris-(2,2'-bipyridine) on tin- doped indium oxide electrode.* Analytica Chimica Acta, 2004. **508**: p. 225.
35. Sheeney-Haj-Ichia, L., Cheglakov, Z.; Willner, I., *Electroswitchable Photoelectrochemistry by Cu2+-Polyacrylic Acid/CdS-Nanoparticle Assemblies.* J. Phys. Chem. B. ; (Communication), 2004. **108**(1): p. 11.
36. Lahav, M.H.-S., V.; Wasserman, J.; Katz, E.; Willner, I.; Durr, H.; Hu, Y.-Z.; Bossmann, S. H., *Photoelectrochemistry with Integrated photosensitizer-Electron Acceptor and Au-nanoparticle Arrays.* J. Am. Chem. Soc, 2000. **122**(46): p. 11480.
37. Sauerbrey, G., Z. Phys, 1959. **155**: p. 206.

# CHAPTER 7

## Reassembly and Detection of virus particles on ITO substrate

## *7.1 General Introduction to plant and animal viruses*

According to the definition of Lwoff and Tounier in 1966, "Virus is an agent which possesses only one type of nucleic acid, has an acellular organization, is unable to provide its own energy and parasites host cell by utilizing its protein synthesis machinery." [1]

Many viruses, such as animal RNA viruses and viruses that infect bacteria, or bacteriophages, have become useful laboratory tools in genetic studies and in work on the cellular metabolic control of gene expression. Because viruses can sometimes carry extra genetic material into host cells, they have been used to experimentally transfer genetic material, specifying a particular enzyme, into nuclei of mammalian host cells that lacked the ability to synthesize that enzyme. The ability of viruses to transfer genetic material has also been extensively studied in bacteria-mediated gene transfers that are medically interesting because of the possibility that, in the future, enzyme-specifying genes might be transferred into humans with hereditary enzyme-deficient diseases. Virus interference is a phenomenon in which host cells, while infected by one virus, are protected against infection by other viruses; the technique has been used experimentally as a form of temporary immunization. Interferon, a vast number of proteins produced by virus-infected cells that inhibit viral replication within the cell, has been studied with a view toward preventing or controlling virus-caused diseases. Viruses continue to be investigated because they are held to be possible causative agents of some human cancers, and because under certain conditions the body's immune response to virus infection may cause tissue damage and develop into an autoimmune disease.

Nanotechnology in combination with viruses can be a powerful drug delivery tool. Hence encapsulation of red clover necrotic mosaic virus (RCNMV) around metallic and metal-oxide nanoparticles were attempted.

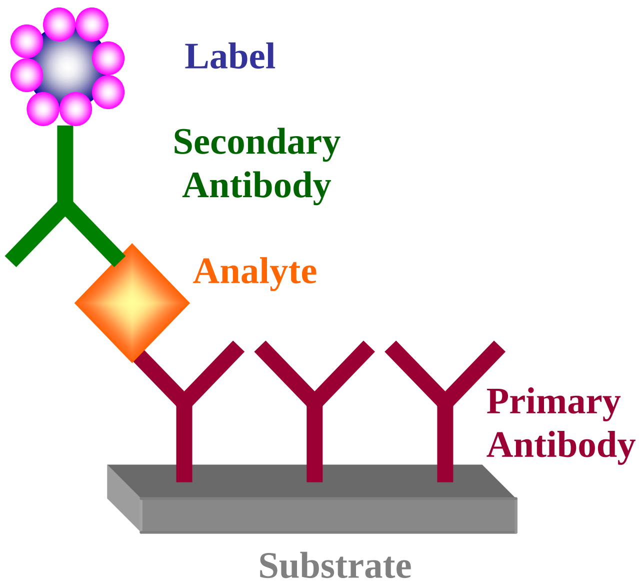


**Figure 7.1 Bioarray for detection of viruses on substrates by photoelectrochemistry**

Photoelectrochemistry is a great technique to detect DNA assays as described in the previous chapter but can also be used to detect viruses and proteins in an antibody sandwich assay format as shown in Figure 7.1.

The antibody sandwich assay can be an enzyme-linked sorbent immunoassay (ELISA) or other immunoassays such as fluorescent immunoassay (FIA) and radioimmunoassay (RIA). In a typical antibody sandwich assay an antibody is attached to the substrate and it binds the target (analyte). A second antibody binds to a second epitope of the analyte (virus) and the location of the bound antibody is read out using the color change of linked enzyme (ELISA), fluorescent emission (FIA) or radioactivity (RIA) represented by the blue circle which is an appropriate label. We propose assembly of viral cage using a Ru sensitized $TiO_2$ nanoparticle as a nucleating agent and a label for photoelectrochemical detection of RCNMV and for HIV-1particles from Gag protein.

### 7.1.1 Properties of Plant Viruses

To understand viruses better it is important to understand the structure of virus particles. Electron microscopy, optical diffraction and X-ray crystallographic procedures provide important architectural information about viruses. In 1962, Caspar et al. coined the term virion to name the mature virus. Capsid denotes the closed shell of the virus and capsomeres are the clusters of subunits of virus. In a membrane-bound virus, the inner nucleoprotein core is called nucleocapsid. Crick and Watson in 1956 hypothesised that the basic structural requirement for a small virus was the provision of a shell of protein to protect its RNA. This assumption was based on the known facts that viral RNA was mostly encapsulated by a protein coat and naked RNA was infectious. They suggested that a large protein coat can be made efficiently by the virus by producing large number of identical small protein molecules rather than a few large ones. When the same bonding arrangement is used repeatedly in the particle, the small protein molecules would aggregate around the RNA in a regular manner. The subunits are normally rods or spheres.

### 7.1.2 Symmetry of Plant Viruses

From crystallographic considerations, the protein shell of a small spherical virus can be constructed from the identical protein subunits arranged with cubic symmetry, for which case the number of subunits would be a multiple of 12.

Crick and Watson in 1956[2] pointed out that the cubic symmetry most likely would lead to an isometric virus particle. The three types of cubic symmetry are tetrahedral(2:3). Octahedral (4:3:2), and icosahedral(5:3:2). An icosahedron has 5-fold, 3-fold and 2-fold rotational symmetry. In the case of viral assembly the three types of cubic symmetry would imply 12, 24, or 60 identical subunits arranged on a sphere. In 1962 Klug and Caspar [3] suggested that most of the viruses have shells made up of subunits arranged with icosahedral symmetry. The basic icosahedron can be sub-triangulated according to the equation

$$T = P \cdot f^2 \qquad (7.1)$$

where T is called the Tiangulation number.

P in the above equation is the number of subdivisions of each side of an equilateral triangle when the face of the triangle is subdivided by lines joining equally spaced divisions on each side. $f^2$ is the number of smaller triangles formed.

## 7.2 Viral encapsulation using $TiO_2$ nanoparticles

### 7.2.1 General Morphology of Red Clover Necrotic Mosaic Virus (RCNMV)

RCNMV is a plant virus of the genus *Dianthovirus*. The three definitive species of Dianthus are: CRSV (carnation ring spot virus), RCNMV and sweet clover necrotic mosaic virus (SCNMV). The genus name Dianthus is derived from the generic name for carnation, dianthus.

RCNMV is a soil-borne virus, very stable and is easily purified hence used in studies of virus properties and replication together with the other dianthoviruses. The size of native wild-type RCNMV particle is 33 nm and is isometric. RCNMV consists of 180 identical capsid protein subunits arranged in T=3 icosahedral symmetry. Its genome is made up of two positive-sense single stranded RNAs. RNA1 encodes a functionally unknown 27-kDa protein and an 88-kDa protein while RNA2 is monocistronic. RNA which encodes a 35k-Da movement protein essential for virus movement in plant. The symmetrical structure of many viruses is because they have identical subunits to create genetic economy, which interact with each other in a similar fashion. The interactions in small viruses are very strong making it symmetrically rigid. Icosahedral is the most efficient symmetry to make a closed shell. [2]

### 7.2.2 Materials and methods

Purified RCNMV was obtained from Dr. Steven Lommel's Research Group at NCSU. It is stored in aliquots in Glycine-NaOH buffer at pH 10 at 4°C. Slide-A-Lyzer® Dialysis Cassette was a convenient means for buffer exchange. 100 ul of the RCNMV coat protein at pH 10 and 50 ul of 10 nM BSPP (10 nm) or 50 ul of $TiO_2$ solution were mixed together. The reassembly properties were investigated by dialyzing the mixed solution overnight against a membrane of 10,000 MWCO in 500 ml dialysis buffer made of 50 mM Tris at pH 6.75.

### 7.2.3 Transmission Electron Microscope (TEM)

10 ul of the pure virion was deposited on a Formvar-coated copper grid and stained with 2% uranyl acetate and the excess liquid was blotted and the grid was allowed to dry. The reassembled virions on the grids were examined by Philips CM-12 TEM (accelerating voltage was 100 kV) at the University of North Carolina Dental School Research Electron Microscopy Center at varying magnifications.

### 7.2.4 Reassembly properties

Reassembly of RCNMV requires RNA. But reassembly of virions has also been observed in absence of Origin of assembly / RNA when colloidal metal or metal-oxide nanoparticles are used as nucleating agents (Unpublished results).

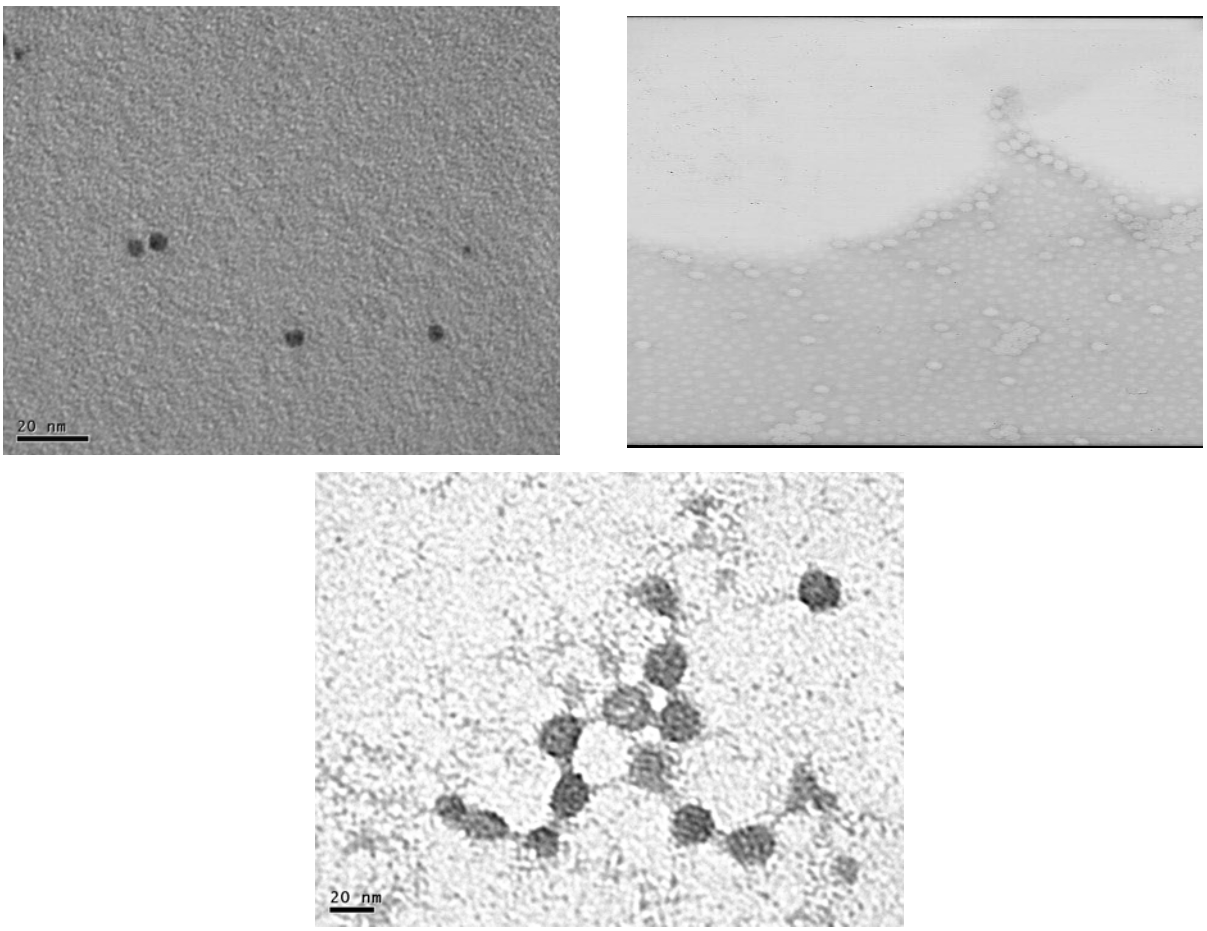


**Figure 7.2 a. TEM images of $TiO_2$ nanoparticles and b. RCNMV assembled $TiO_2$ nanoparticles**

The resulting reassembled virus particles are generally smaller than its wild type counterpart. The symmetry of such reassembled particles are T=1 instead T=3 which are 33±2 nm in size. In the present study aqueous $TiO_2$ nanoparticles were used as nucleating agent Figure 7.2 A is the TEM image of plain $TiO_2$ nanoparticles and Figure 7.2 B is the virus in absence of any nanoparticles and 7.3 C reassembled RCNMV with $TiO_2$ as nucleating agent. The size of $TiO_2$ is 5-6 nm as seen in Figure 7.3 A. and also the native RCNMV exhibits a size range of 35 nm. But as the virion reassembles around the $TiO_2$ nanoparticle, the size increases to around 17 nm. Since the encapsulation was successful in solution the next step was attempts to capture these encapsulated virions onto a solid substrate.

To be able to detect viruses on ITO surface antibodies were immobilized on the surface of ITO by EDC reaction. The ITO surface was first modified with 12-PDA as described in the previous chapters and deposited in 150 pM antibody solution in MES buffer at pH 9 with 200 mM EDC overnight. The pH range used for EDC coupling reaction is generally 5.5. For this reaction a high pH (pH~9) solution was used to deprotonate all the lysines on the antibody making them a better nucleophile to attack the COOH group in the EDC coupling reaction. The assembled RCNMV virus was then applied to the Ab modified surface and the reaction was allowed to proceed for 15 min. The surface was then analyzed by XPS. The presence of 1s Nitrogen peak would signify presence of Ab on the surface and an increase in intensity for the substrate that was exposed to RCNMV virus would prove that RCNMV binds to the Ig. But the results were not very clear. Hence, it was proposed to use nanoparticles as nucleating agents in the assembly of the coat protein that could be detected with relative ease by XPS and Photoelectrochemistry.

10 nm BSPP coated gold colloid, and magnetic $CoFeO_3$ nanoparticles were used to assemble the coat protein around it. The same procedure as mentioned above was utilized to bind Ab on ITO substrates. The modified substrates were then exposed to

RCNMV solution reassembled in presence of $CoFeO_3$ particles or 10 nm gold colloid (dialyzed at pH 6.75 in Tris buffer). The XPS results(data not shown) did not show any intensity for Au, Co or Fe denoting absence of binding of assembled particles of RCNMV on the Ig modified ITO surface.

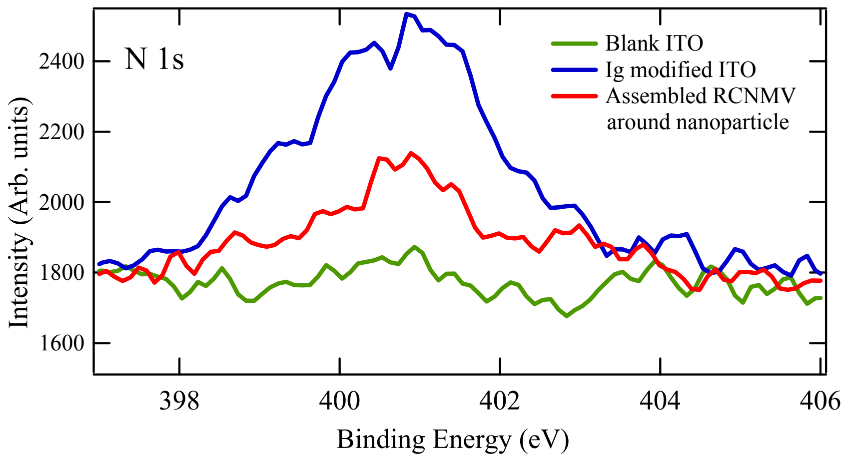


**Figure 7.3 XPS of N 1s of plain ITO, ITO modified with PDA and EDC coupled to RCNMV Antibody and ITO modified with PDA, EDC coupled to RCNMV Antibody and reacted with assembled virus**

## 7.2.5 Conclusions

The viral assembly properties have to be studied thoroughly to understand their assembly on surface. The viral behavior on the surface is different from the assembly properties in solution. A lot of research has been carried out in reassembly of virus particles in solution. Mark Young etal [4] have used cowpea chlorotic mottle virus (CCMV) to grow tungstate crystals inside the inner cavity of the virus particle [5]. Franzen etal have successfully encapsulated Au and magnetic $CoFeO_3$ nanoparticles in to RCNMV(unpublished results).in solution. On surface virus particles did not form as expected. The virus binds to the Ig attached to the ITO surface by EDC coupling but the conformation may not be favourable for RCNMV to form reassembled particles and also partcles reassembled with nanoparticles inside are not stable when reacted to anti-Ig modified ITO substrate.

## *7.3 Introduction to Retroviruses*

The retroviruses have many applications in biotechnology for delivering genes to target cells at high efficiency in a manner that allows for long-term, stable expression of introduced genetic elements.

Skalka and Goff in 1993 used reverse transcriptase (from avian and murine retroviruses) to generate cDNA copies of RNA for cloning and sequencing. The other applications are virus-mediated gene transfers - enzyme-specifying genes might be transferred into humans, cell marking, promising delivery vehicles for human Gene therapy and genetic and acquired diseases - addition of genes to correct disorders.

Human immunodeficiency virus (HIV), the virus associated with AIDS, is a retrovirus that appears to have mutated into a number of strains that attack the immune system and produce viral-induced immunosuppression. HIV, the virus associated with AIDS, is a retrovirus (RETROVIRUS: a class of enveloped viruses that have their genetic material in the form of RNA and use reverse transcriptase to translate their RNA into DNA. The retrovirus family includes oncoviruses (e.g., HTLV-1) and lentiviruses (e.g., HIV-1, HIV-2) that appear to have mutated into a number of strains that attack the immune system and produce viral-induced immunosuppression.

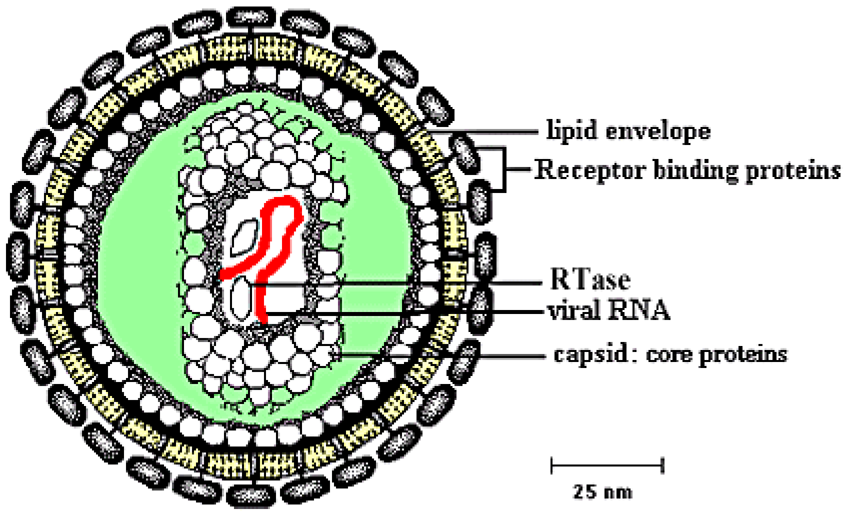


http://www.accessexcellence.org

**Figure7.4 Diagram of a Retrovirus**

Retroviruses are infectious particles consisting of an **RNA genome,** which is packaged in a protein **capsid** and surrounded by a **lipid envelope**. This lipid envelope contains polypeptide chains including **receptor binding proteins** which link to the membrane receptors of the host cell, initiating the process of infection. There are three known retrovirus categories :

- *Oncovirinae* cause sarcomas and leukaemias (e.g., Rous Sarcoma Virus).. They contain an *onc* gene which makes them oncogenic.
- *Lentivirinae* cause slow progressive degenerative disorders (e.g., HIV)
- *Spumavirinae* with no known pathogenic effects.

All four identified human retroviruses (HTLV 1&2, HIV 1&2) attack CD4 cells.

Another feature common to all retroviruses is a lipid envelope surrounding their capsid. It is essential for their function. This explains why retroviruses can be killed by just washing hands.

Retroviruses contain RNA as the hereditary material in place of the more common DNA. In addition to RNA, retrovirus particles also contain the enzyme reverse transcriptase (or **RTase)**, which causes synthesis of a complementary DNA molecule (cDNA) using virus RNA as a template. When a retrovirus infects a cell, it injects its RNA into the cytoplasm of that cell along with the reverse transcriptase enzyme. The cDNA produced from the RNA template contains the virally derived genetic instructions and allows infection of the host cell to proceed.

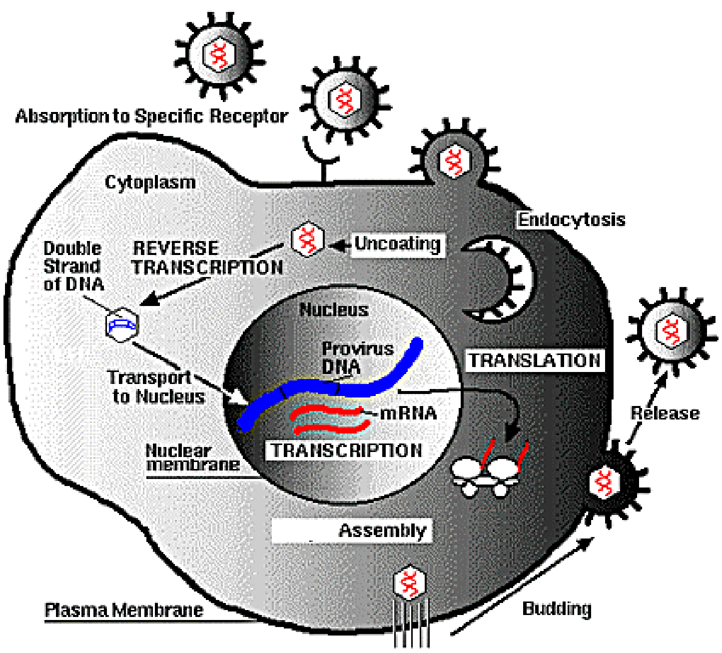


**Figure 7.5 Infection cycle of retrovirus**

Retroviruses contain viral RNA and several copies of reverse transcriptase (DNA polymerase). After infecting a cell, the reverse transcriptase is used to make the initial copies of viral DNA from viral RNA. Once a DNA strand has been synthesized, a complementary viral DNA strand is made. These double strand copies of viral DNA are inserted into the host-cell chromosome and host-cell RNA polymerase is used to make virus-related RNA. These RNA strands serve as templates for making new copies of the viral chromosomal RNA and serve as mRNA. mRNA is translated into viral proteins that are used to make the virus envelope. New viral particles are assembled, bud from the plasma membrane, and are released. An example of this process is illustrated in the replication of the retrovirus, HIV.

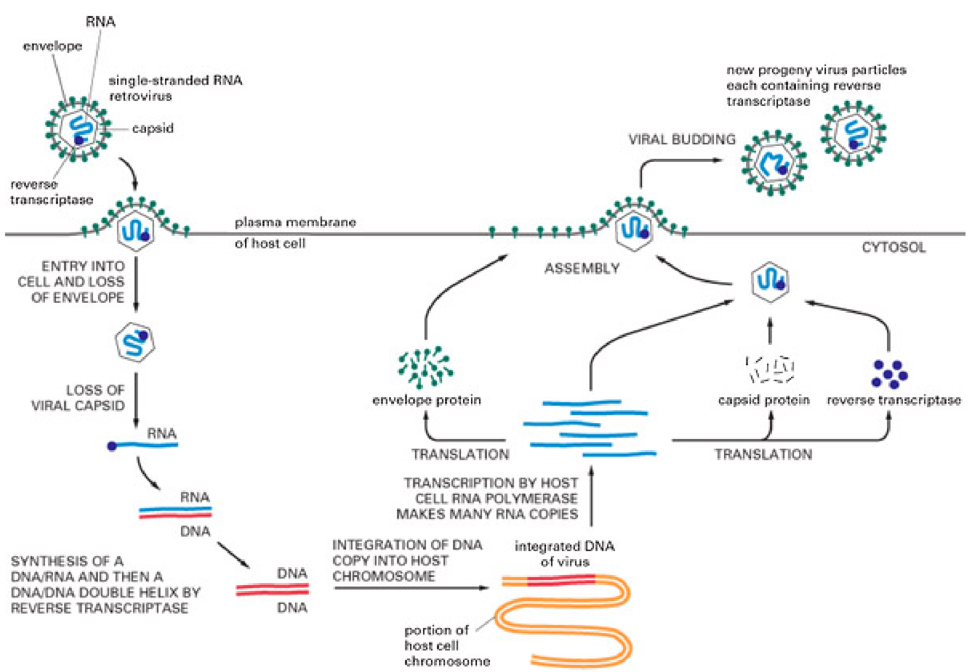


http://www.accessexcellence.org

**Figure 7.6 Replication and budding of retroviruses**

The typical retrovirus genome consists of a single-stranded RNA of about 8500 nucleotides. The enzyme reverse transcriptase is a multifunctional enzyme that first makes a DNA copy of the viral RNA molecule. It then acts as a nuclease to remove the RNA, and then makes a second DNA strand, generating a double-stranded DNA copy of the RNA genome. The integration of this DNA into the host chromosome, catalyzed by a viral protein called integrase, is required for the synthesis of new viral RNA molecules by the host cell RNA polymerase. Retroviruses are examples of enveloped viruses, in which the protein shell is further enclosed by an outer lipid bilayer membrane. The envelope contains proteins that enable the virus to bind to cells, and that aid its entry into a cell. As indicated, the lipid membrane is acquired when the virus is released from the cell by a process of budding from the plasma membrane, taking some of the plasma membrane with it. The budding process is reversed when the virus reinfects a cell.

The retrovirus genome contains at least three genes:

- *gag* codes for core and structural proteins of the virus.
- *pol* codes for reverse transcriptase, protease and integrase.
- *env* codes for the virus hull proteins.

Gag protein is the most important structural component in retrovirus particle and is sufficient for assembly of the retrovirus particles in mammalian cells. After the virion is realeased, Gag is cleaved by the viral protease(PR) into the Gag derived proteins of the mature particles. The cleaved products include proteins, matrix(MA), capsid (CA) and nucleocapsid (NC) and the sequences present in these domains are all required for particles assembly.

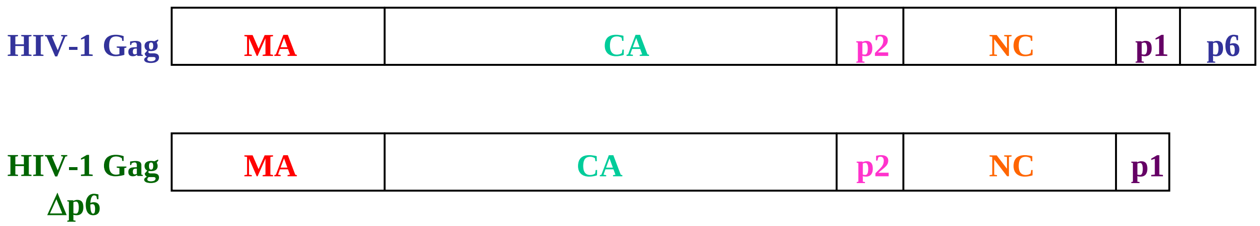


**Figure 7.7 Coding and Non coding proteins in retroviruses**

The functions of these domains differ during the assembly process and in a mature virus and are listed in Table 7.1 below:

| | **Functions during assembly** | **Functions in mature protein** |
|---|---|---|
| MA | transport of Gag from within cell to plasma membrane | Protein interactions |
| CA | guides the arrangement of Gag molecules during assembly | Forms shell around the viral core |
| NC | packages the viral genome and promotes Gag-Gag interactions | Protects the viral genome |

**Table 7.1 Funcions of coding proteins**

Alan *et al.* studied the steps in reassembly of the virus particles from Gag. Assembly process starts with accumulation of Gag protein into electron-dense patches below the plasma membrane. The patches then enlarge and project outward to form a spherical particle, which pinch off and released. The fresh particles have immature morphology with a donut shape appearance. After the budding PR is activated and the peripheral material condense into a cone-shaped core at the center of HIV particle representing a mature virus particle. They reported in vitro assembly properties of HIV Gag and a Gag mutant with missing p6 domain. Both HIV-1 Gag and Gag Dp6 protein formed sheets when incubated without nucleic acid. On addition of RNA the Gag Dp6 formed particles that are spherical but smaller in diameter (30 nm). In contrast Gag at RT formed heterogenous, elongated structures in presence of RNA while at 4 $^{o}$C both assembled into uniform, small particles.

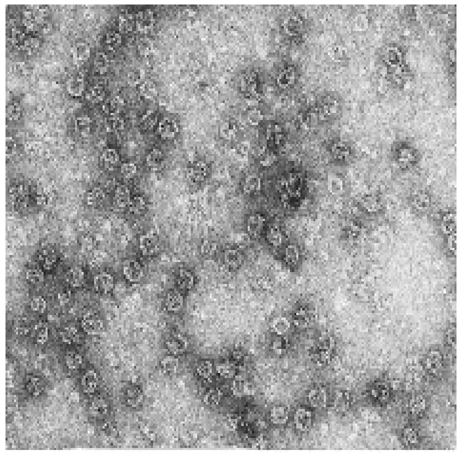

**Figure 7.8 TEM image of reassembled HIV Gag protein**

Based on the above reassembly properties of HIV Gag protein we proposed the reassembly of HIV virus particles from Gag with 10 nm gold nanoparticles as nucleating agents. 10 nm BSPP stabilized gold colloid solution and purified Gag protein received from NIC were used for the reassembly experiment.

### 7.3.1 Materials and Methods

The dp6 HIV Gag protein was a generous gift from Dr. Alan Rein from NIC. It was purified by Siddhartha A.K. Datta and sent as five aliquots (90 ul each) with concentration 5.2 mg/ml. The composition of the buffer was 20 mM Tris-Hcl pH 7.4 / 0.5 M NaCl / 10 mM DTT / 3 mM TCEP / 1mM PMSF and the proteins were flash frozen on dry-ice/methanol. The protein was stored at –80$^{o}$C and to use was quick thawed in a water bath at room temperature. The protein aliquot was then centrifuged at 10,000g for 10 min. Protein in storage buffer was diluted to 1mg/ml and 0.1 M NaCl by adding 20 mM Tris(pH 8.0) and 10 mM DTT Gold-DNA bioconjugate solution of 1nM concentration was made as described in Chapter 4 such that the ratio of gold to DNA was 1:400. 64.6 ul of 1 nM 10 nm gold-bioconjugate solution and 323 uL of Gag protein were reacted in 20 mM Tris buffer (pH 8) and 157 uL of 10 mM DTT. The reaction mixture was incubated for 2 h. The reaction product was analysed by DLS and TEM.

### 7.3.2 Dynamic Light Scattering( DLS)

DLS was used to determine the size of the Gag by Malvern Zetasizer 1000HS and analyzed in the CONTIN mode. The intensity as a function of size in nm gives a size distribution of the molecules of interest. The samples for DLS were prepared by diluting the samples of DNA stabilized Au solution, the Gag protein and the incubated solution in appropriate buffers and analyzed.

### 7.3.2 Transmission Electron Microscope (TEM)

10 ul of the sample was deposited on a Formvar-coated copper grid and stained with 2% uranyl acetate and the excess liquid was blotted and the grid was allowed to dry. The reassembled virions on the grids were examined by Philips CM-12 TEM (accelerating voltage was 100 kV) at the UNC Dental School Research Electron Microscopy Center at varying magnifications.

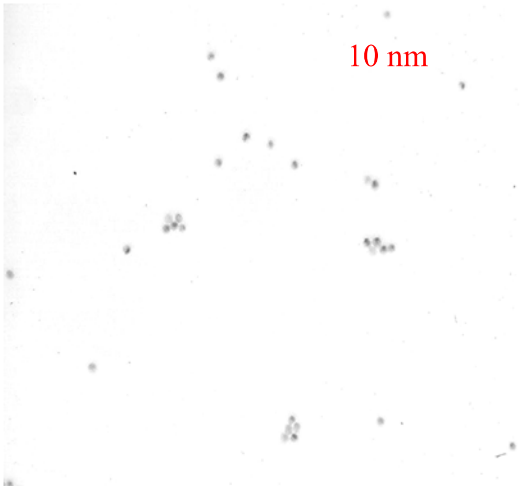


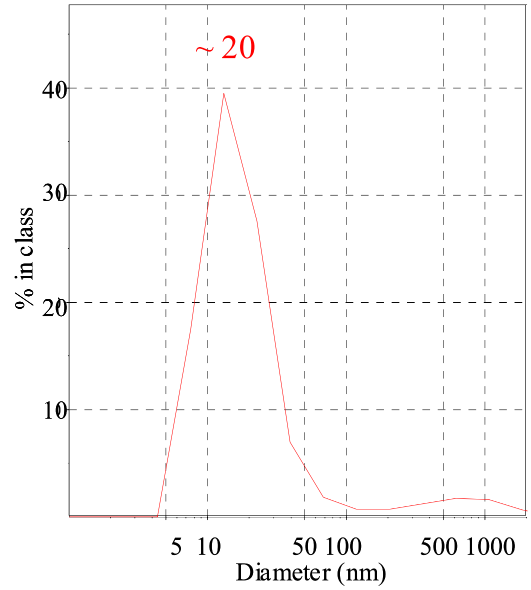


**Figure 7.9 A. 10 nm BSPP coated Au nanoparticles B. DLS of DNA-Au bioconjugate**

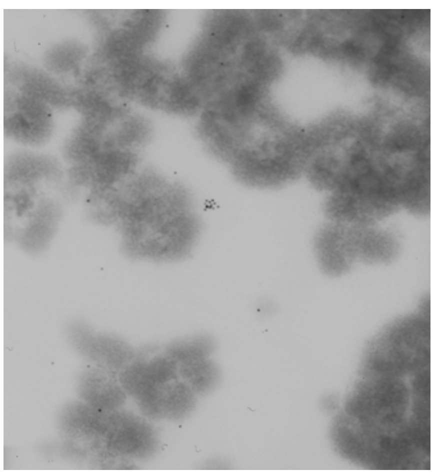

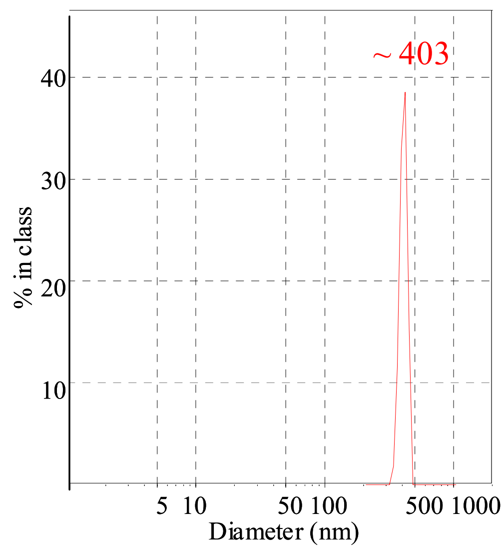


**Figure 7.10 . Plain Gag protein A. TEM** **B. DLS**

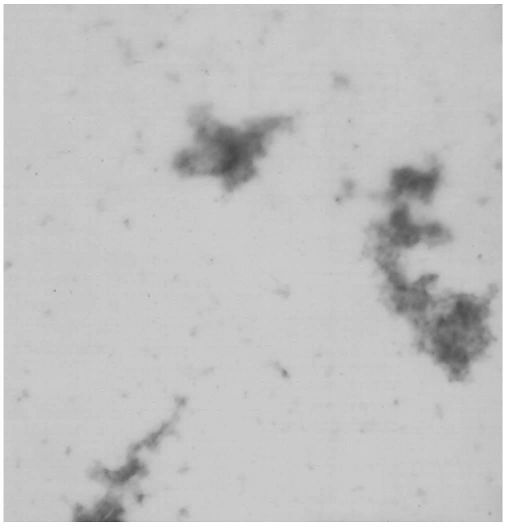

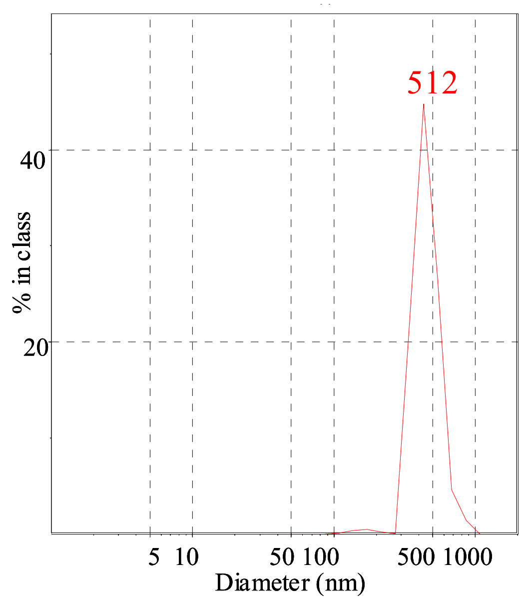


**Figure 7.11. Reassembled Gag protein A. TEM B. DLS**

## 7.3.3 Conclusions

Based on successful encapsulation of metallic nanoparticles by RCNMV, attempts to reassemble HIV virus particles from Gag protein was made. Rein etal have reported formation of spherical particles in vitro of dimension ~30 nm. The particles formed in vivo in infected cells are normally ~120 nm in diameter. These spherical virus particles were formed in the presence nucleic acid. The Gag protein under low ionic-strength form protein-sheets even with out nucleic acid - essentially it is very sticky under such conditions (~100 mM NaCl). Repeated attempts to assemble the particles failed as seen in the TEM images.

.

## *Acknowledgements*

We thank Dr. Steven A.Lommel and Dr. Richard H. Guenther, Department of Plant Pathology, NCSU for providing RCNMV. We also would like to acknowledge Dr. Alan Rein and Siddhartha A.K. Datta from NIC who gifted us with HIV Gag protein.

## *References*


(1) Lwoff, A., Tournier, P. *Ann. Rev. Microbiol.* **1966**, *20*, 46.

(2) Crick, F. H. C., Watson, J. D. *Nature* **1956**, *177*, 473.

(3) Caspar, D. L. D., Klug, A. *Cold Spring Harb. Symp. Quant. Biol.* **1962**, *27*, 1-24.

(4) Flenniken, M. L. L., L. O.; Crowley, B. E.; Willits, D. A.; Young, M. J.; Douglas T. *Chemical Communications* **2005**, 447-449.

(5) Mark Allen, D. W., ; Jesse Mosolf; Young, M. J.; Douglas, T. *Advanced Material* **2002**, *14*, 1562.